A Search for Evidence of New Particle Production in Semi-leptonic Top Quark Pair Events with at least one Photon and MET of pp Collisions at sqrt(s) of 13 TeV

Fan Xia

Charlottesville, VA

B.S., Lanzhou University, China 2012

A Dissertation presented to the Graduate Faculty of the University of Virginia

in Candidacy for the Degree of Doctor of Philosophy

Department of Physics

University of Virginia

May 2019

We approve the dissertation of Fan Xia.

Date of Signature

Bradley Cox

March 14, 2019

Supervisor: Dr. Bradley Cox

3/14/2019

Reviewer: Dr. Bob Hirosky

Reviewer: Dr. Hank Thacker

3/14/2019

Independent Reviewer: Dr. Craig Sarazin

Abstract

This dissertation presents a search for evidence of new particle production in semi-leptonic top quark pair events with exactly one lepton (electron or muon), at least one photon, and E_T^{miss} using proton-proton collisions at the center-of-mass energy $\sqrt{s} = 13$ TeV collected by the Compact Muon Solenoid (CMS) experiment at the Large Hadron Collider (LHC) in RunII 2016, corresponding to an integrated luminosity of 35.87 fb^{-1}.

This search is based on a scenario where the top squark is the lightest squark, the gravitino is the lightest supersymmetric particle and the bino-like neutralino is the next-to-lightest supersymmetric particle in Gauge Mediated Supersymmetry Breaking (GMSB) models. The strong production of top squark pairs yields events with top quark pairs and pairs of neutralinos where each neutralino decays to a photon and an undetected gravitino which leads to the significant missing transverse momentum. To minimize the QCD background, the semi-leptonic decay channel of the top pairs is required by selecting events with jets and either an electron or a muon. In addition, the presence of at least one energetic photon in the final state is required to improve signal significance. The missing transverse momenta of these events are compared to the expected spectrum of Standard Model processes to search for evidence of supersymmetry. The conclusion is that no evidence of new particles is found in this analysis. The result is interpreted to set an upper limit which excludes top squark masses up to 1000 GeV/c^2, exceeding previous results by 250 GeV/c^2.

Acknowledgements

The research presented in this dissertation is made possible by the dedicated contributions of the thousands of intelligent individuals at the Large Hadron Collider and the Compact Muon Solenoid. With decades profoundly efforts, the most powerful machine was launched to discover the mystery of physical world and surely will keep advancing human understanding. I am so proud and grateful to have been part of this great endeavor, and would like to acknowledge everyone who worked to make it happen.

I would like to express my immerse gratitude to my advisor Professor Brad Cox, who is also my deeply respected physicist. He brought me into the real experimental physics world, gave me the opportunity to explore the new physics at the world largest machine in history. I would like to thank him for his great physics insight that guides me through my research and all kinds of support he has provided me during my graduate study.

The high energy physics group at the University of Virginia has been the supportive home for me in the last six years. I want to thank Brian Francis, who gave me hands-on help of this analysis and always be patient to my questions as well after he graduated. I have to thank Evan Wolfe, Thomas Anderson, Yanchu Wang, Matt Joyce, Steve Boi for all the fun time and help I have received, not only in inspiring academical discussions but also in daily life, like saving me from my stuck car. Thanks go to Professors Chris Neu and Bob Hirosky, who, as well as being excellent physicists, I have learnt a lot and got great advice from them. I thank other members of my thesis committee, Professor Craig Sarazin and Professor Hank Thacker for their comments and advices.

During my two years stay at CERN, I have been involved in working on the detector. I would like to thank Sasha Ledovskoy for his guidance on EB noise simulation and advice for my analysis. My thanks as well go to Ecal Trigger team. The time I had spent at P5 and 24/7 on-call shifts are memorable experience. I would like to thank Tutanon Sinthuprasith, who had led the team efficiently, and was always warm-hearted to my request for favor. I would like to thank Alex Zabi, he is so knowledgeable of the detector, and always being kind and patient to our students. I have to thank the CMS SUSY group for their guidance through my analysis.

Finally, I would like to thank my parents, their love and encouragement keep me moving forward and make me here today!

Contents

List of Figures

List of Tables

Chapter 1

Introduction

The success of the Large Hadron Collider (LHC) in producing of the world highest energy proton-proton collisions has created very exciting and promising expectations in the particle physics. During the RunI period (2009-2013), the last element of the Standard Model (SM), the "Higgs boson" was discovered, marking the confirmation of the fundamental theory for the electroweak's sector of particle physics. However, we should not be blind about the shortcomings of the Standard Model. The Standard Model cannot explain the existence of dark matter which is considered to be the main component of mass in our universe. It also suffers from the "hierarchy problem" since the mass of Higgs boson should be much heavier due to the radiative corrections it receives in the SM framework. Furthermore, the theories of three fundamental interactions described by the SM are expected to unify at a large energy scale in a grand unification theory (GUT), where there is no distinction between interactions. Chapter 2 gives an overview of the SM and discusses the motivation for new physics.

To address these problems of the SM and expectations for new physics, many theories beyond Standard Model (BSM) physics are proposed to extend the SM with high energy phenomena while keeping consistency with our lower-energy observations. Supersymmetry is one of the most promising theories among them since it successfully remedies the deficiencies of SM. Chapter 3 introduces the SUSY theory and the specific model used in this analysis.

To penetrate into the micro world, the large hadron collider accelerates protons close to light speed, enabling high energy collisions to produce fundamental particles. To observe these produced particles, the Compact Muon Solenoid (CMS) detector tracks their interactions with the CMS detector elements. Chapter 4 covers the design of LHC and CMS, and reveals how the detector elements work in observing the particle world. Chapter 5 explains how the fundamental particles are reconstructed from the raw data that are collected and recorded in experiments.

During the RunII period (2015-2018) of the LHC, the center of mass energy of the proton-proton collisions was upgraded to 13 TeV in an attempt to produce a breakthrough discovery. This dissertation presents a search for a SUSY particle, the top squark, which is the supersymmetric partner of the top quark. This analysis uses the 2016 full datasets collected by the CMS detector, corresponding to an integrated luminosity of 35.87 fb^{-1}. Chapters 6 and 7 describe this analysis and the interpretation of results. Chapter 8 presents the conclusions of this search. The results of this research show no evidence for the existence of the top squark. A shape analysis based on observed data distributions is performed and an exclusion limit is calculated on the top squark mass up to 1000 GeV/c^2.

Chapter 2

The Standard Model of Particle Physics

The Standard Model is built on quantum field theory, describing the fundamental particles and their interactions. Theoretical development since the mid 20^{th} century together with the increased energy of accelerators and improved measurement capabilities of modern particle detectors, have verified the tremendous success of the Standard Model in predicting and explaining the experiments results.

This chapter presents a discussion of the Standard Model and shows some of its successful predictions in experiments. Although it is believed to be a self-consistent theory, the Standard Model has unexplained areas and inconsistencies. The new physics is motivated by needs to broaden and improve the Standard Model, and is discussed in next chapter.

2.1 The Standard Model

The Standard Model was inspired from many great concepts developed around middle of the 20th century, the first step was attributed to Sheldon Glashow [16] for combining the electromagnetic and weak interactions in 1961. In 1967, Steven Weinberg [17] and Abdus Salam [18] demonstrated the Higgs mechanism could trigger the electroweak symmetry breaking which gives rise the masses of all elementary particles. The Higgs mechanism was incorporated into Glashow's electroweak theory, forming the modern shape of the Standard Model.

The Standard Model is based on a quantum field theory that incorporates the elementary particles and their interactions through quantum fields. There are two types of elementary particles in the Standard Model, fermions with 1/2 spin, and bosons with integer spin. The gauge bosons in the Standard Model are the force carriers that mediate these three kinds of interactions in the Standard Model. Table 2.2 lists the bosons and their features in the Standard Model. Fermions are separated into three generations, sharing the same quantum numbers but different masses and lifetimes. Fermions can also be classified into either lepton or quark according to the type of interactions in which they participate. Table 2.1 lists the fermions of the Standard Model.

	Leptons		Quarks	
1st generation	e	ν_e	u	d
2nd generation	μ	ν_μ	c	s
3rd generation	τ	ν_τ	t	b
charge	-1	0	2/3	-1/3

Table 2.1: Elementary fermions in the Standard Model

	Charge	Spin	Interactions participate
gluon	0	1	Strong
$W^{\pm}$	$\pm$ 1	1	Electroweak
Z	0	1	
γ	0	1	
H	0	0	

Table 2.2: Elementary bosons and their properties in the Standard Model

The dynamics of the Strong and the Electroweak interactions are described by the gauge groups where exchanges of the gauge bosons mediate the forces between the particles.

$$SU(3)_C \otimes SU(2)_L \otimes U(1)_Y \tag{2.1}$$

The Strong interaction or the Quantum Chromodynamics theory (QCD) in field theory is described by the $SU(3)$ gauge symmetry. There are 8 massless gauge bosons called gluons carrying a color charge performing as the strong force carriers. Gluons can interact with other gluons and quarks which also carry the color charges.

QCD is a short distance interaction, and has two main features, color confinement and asymptotic freedom.

The color confinement includes the property that no color charge can be observed directly. All particles carrying colors are confined and formed in colorless states. Hadrons are the most common colorless states, categorized into two types: baryons made up of three quarks and mesons made up of one quark and its anti-quark. The second feature asymptotically freedom [19] [20] is the property that the interaction between quarks becomes stronger as the interaction distance increases within the interaction range, leading to the confinement of quarks and gluons within hadrons.

The electromagnetic and weak interactions are unified as $SU(2)_L \otimes U(1)_Y$. The $U(1)$ gauges field boson is B, and the $SU(2)$ has three component bosons, W^1, W^2, W^3. These gauge bosons mix and generate the observable particles: $W^{\pm}$, Z^0 and γ,

$$\begin{pmatrix} \gamma \\ Z^0 \end{pmatrix} = \begin{pmatrix} \cos\theta_W & \sin\theta_W \\ -\sin\theta_W & \cos\theta_W \end{pmatrix} \begin{pmatrix} B \\ W^3 \end{pmatrix}, \tag{2.2}$$

where θ_W is the Weinberg angle or weak mixing angle, it also gives the mass relation between Z and W bosons.

$$m_Z = \frac{m_W}{\cos\theta_W} \tag{2.3}$$

To maintain local gauge invariance, gauge fields are required to be massless, like photons in the electromagnetic interaction and gluons in the strong interaction. But in weak interactions, the W and Z are not massless and do not preserve local gauge invariance. To incorporate these physical features, a complex scalar field with non-zero vacuum expectation value was introduced, leading to the spontaneously broken symmetry of $SU(2)_L \otimes U(1)_Y$, and generating the masses of the gauge bosons. An additional scalar boson is also introduced to the SM, the Higgs boson. This mechanism is known as the Higgs mechanism [21], and the elementary fermions also gain masses by coupling to the Higgs field.

The Standard Model of particle physics successfully describes three of the four fundamental interactions. Through half a century's experiments, many particles and their properties predicted by the Standard Model have been observed and confirmed, including W and Z bosons by the CERN SPS in 1983, bottom and top quarks at Fermilab in 1977 and 1995, etc. Most recently, a new particle was discovered 2.1 and confirmed to be the Higgs boson in 2012 by the ATLAS [2] and CMS [1] experiments at LHC, completing the last aspect of the Standard Model.

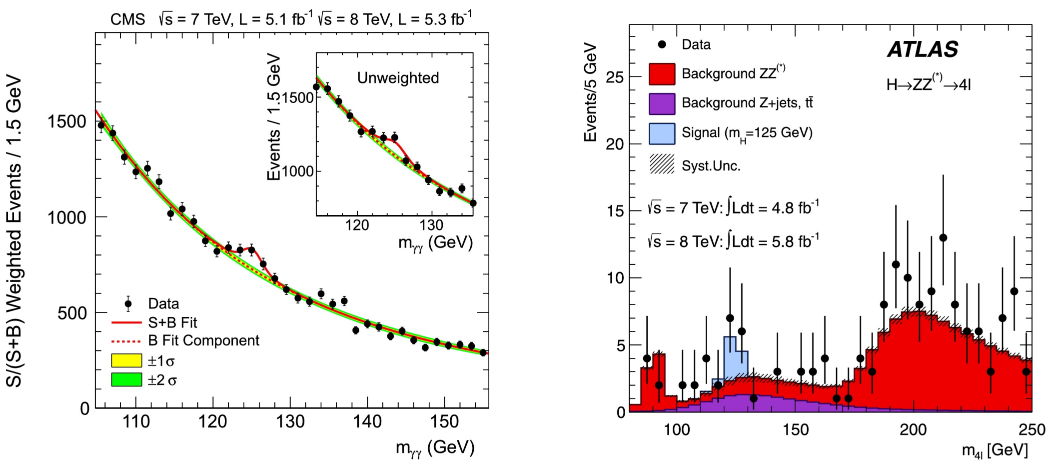

Figure 2.1: The diphoton invariant mass distribution in H→ $\gamma\gamma$ channel (left), reprinted from reference [1], The distribution of the four-lepton invariant mass in H→ 4 *lepton* channel (right), reprinted from reference [2].

2.2 Motivations for New Physics

Although the Standard Model has incorporated and explained many of the elements of particle physics in its half-century development, its shortcomings cannot be neglected, and new physics beyond Standard Model are inevitably motivated by the imperfection of the SM.

The mass of the Higgs boson was not predicted in the Standard Model. It was discovered to be 125GeV [2] [1] by the CMS and ATLAS experiments. However, the mass of the Higgs boson, as a scalar field, receives corrections from radiative coupling to the fermions. The first-loop order correction can be written as,

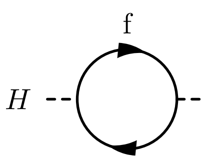

$$\Delta m_H^2 = -\frac{|\lambda_f|^2}{8\pi^2}\Lambda_{UV}^2 + o(\ln \Lambda_{UV}) \tag{2.4}$$

Λ_{UV} is the ultraviolet cutoff energy up to where the Standard Model should be valid. Λ_{UV} is presumed to be M_{plank} of order 10^{19} GeV. The first-loop order correction, proportional to Λ_{UV}^2, is quadratically divergent. Without introducing new physics, to maintain $m_{Higgs} \sim 125$ GeV, a precise "fine-tune" of physics constants is required to cancel these correction terms. This is considered to be an "unnatural" physics condition.

The hierarchy problem, in general, is the question of the large discrepancy in strength between the weak force and gravity. Here the Standard Model offers no indication of the mechanism leading to the enormous differences in scale.

Another mystery in astrophysics and cosmology is the evidence of the presence of dark matter [22] [23] in the observable Universe which cannot be explained in the SM. One compelling observation is the discrepancy between the expected and observed galaxy rotation curves. The curve of the orbital speeds of visible matter versus their radial distances from a galaxy's center can deviate from expectations. An example is shown in Figure 2.2. The invisible matter makes non-negligible contribution. In a standard cosmology model, the dark matter is estimated to constitute 85% of the total matter.

Furthermore, the SM builds on the $SU(3)_C \otimes SU(2)_L \otimes U(1)_Y$ gauge theory and there are three gauge couplings playing vital roles in the theory. The simple and elegance of physics leads to that belief that the SM is imbedded in a grand unification theory (GUT). Given these couplings "run" (change magnitude with the energy of the interaction), it has been a long hope that these couplings unify at a certain very high energy scales to achieve a Grand Unification and even further the Theory of Everything (TOE) including the Gravity and the SM interactions. This dream cannot be realized in current Standard Model framework.

All these problems in the Standard Model require the existence of physics beyond SM. In next chapter, Supersymmetry, one very promising theory among all these new physics models comes to rescue. It solves the hierarchy problem, offers candidates for dark matter, and produces unification of the gauge couplings. The supersymmetric extension of the Standard Model paints a more complete picture of fundamental particle physics.

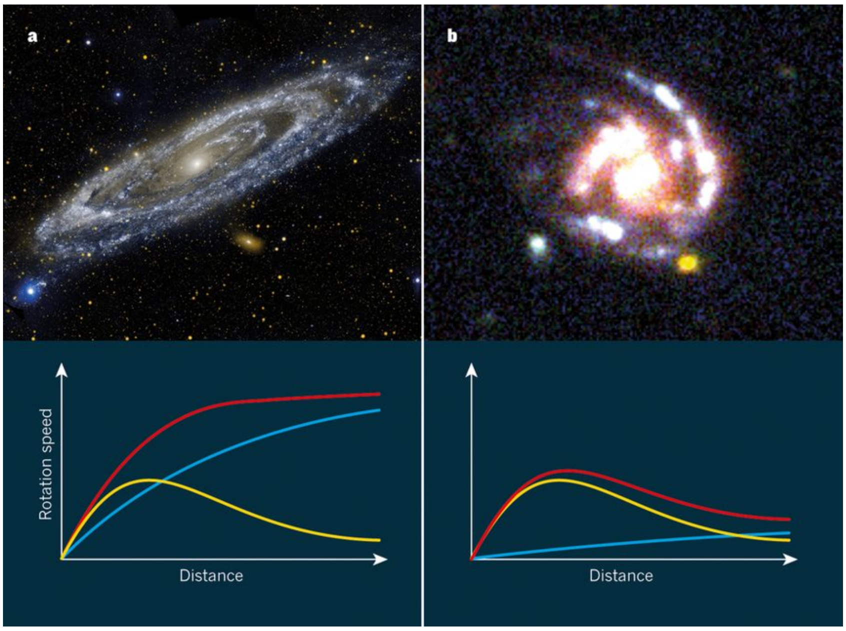

Figure 2.2: Galaxy rotation curves of two galaxies from different classes, a) nearby spiral galaxy, b) Six massive star-forming galaxy in the distant Universe. The rotation speeds are observed to be red curves, in contrast to the expected yellow curves derived from the visible matter. Astronomers proposed the additional mass of the galaxies contribution by invisible "dark matter" in blue curves. Reprinted from reference [3].

Chapter 3

The Supersymmetric Extension to the Standard Model

3.1 Supersymmetry

The primary motivation of Supersymmetry [4] [24] is to connect fermions and bosons in a symmetric theory. The SUSY generator $\hat{Q}$ is introduced. It transforms a fermion to a boson and transforms a boson to a fermion. As a consequence, for each particle in the Standard Model, there is a supersymmetric partner with spin that differs by 1/2, while all other quantum numbers are the same. For instance, the color charge and the electric charge are not changed for the supersymmetric partner.

$$\hat{Q}|Boson\rangle = |Fermion\rangle, \qquad \hat{Q}|Fermion\rangle = |Boson\rangle \tag{3.1}$$

With this fundamental principle in the Supersymmetry theory, the hierarchy problem in the Standard Model is naturally solved without requiring precise fine-tuning. The Higgs mass correction would add the bosonic supersymmetric partners for the SM fermions.

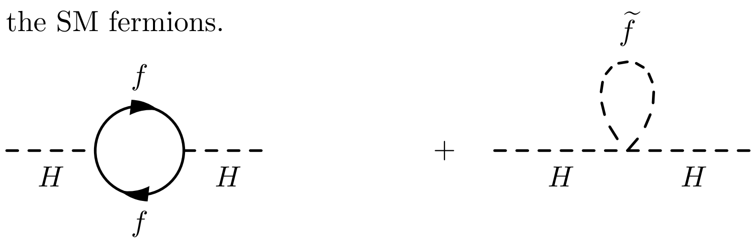

Thus, the correction can be written as,

$$\Delta m_H = \frac{-|\lambda_f|^2}{8\pi^2}\Lambda_{UV}^2 + 2 * \frac{+\lambda_S}{16\pi^2}\Lambda_{UV}^2 + \ldots \tag{3.2}$$

where the couplings to the Higgs are exactly the same $|\lambda_f|^2 = \lambda_S$. The divergent correction from SM fermions cancels as the bosonic supersymmetric partner would act as an opposite mass contribution.

Another advantage of supersymmetry for physics beyond SM is a possible explanation of dark matter. In many Supersymmetry models, there are stable and weak interacting particles (such as gravitino in general gauge mediated supersymmetry (GGM)) that can be dark matter candidates.

Finally, the ultimate goal of theoretical physics is to achieve a grand unification theory, in which the gauge couplings can be unified. In Standard Model, the renormalization group running of gauge couplings cannot make them meet together at a common energy scale, while in the supersymmetry theory, the couplings can be unified at 10^{16} GeV scale.

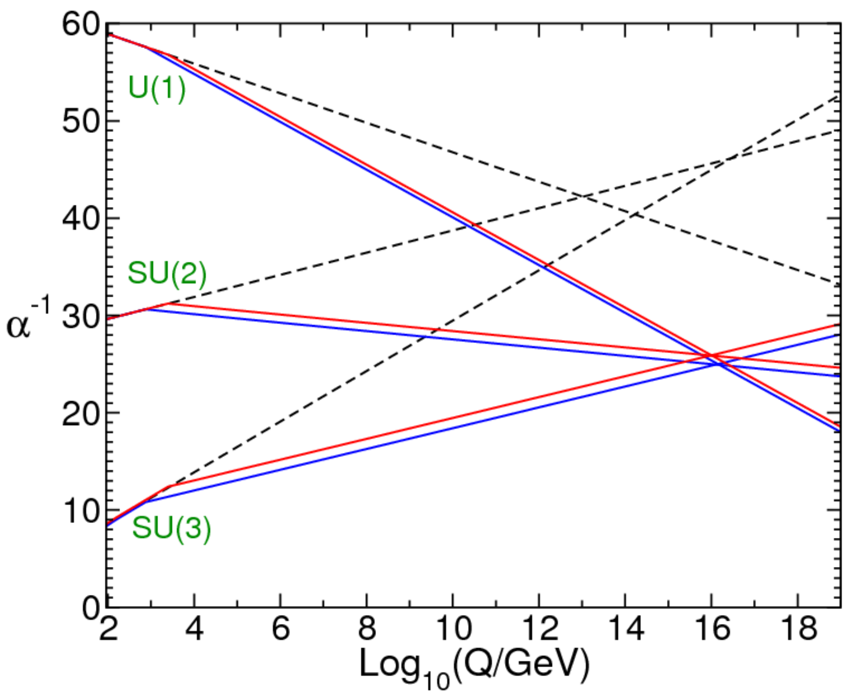

Figure 3.1: Two-loop renormalization group evolution of the gauge couplings. The dashed lines represent the running in the SM, the read and blue solid lines represent the running range with the choice of free parameters in SUSY models. Reprinted from reference [4].

3.2 The Minimal Supersymmetric Standard Model

The minimal supersymmetric Standard Model (MSSM) is the minimal extension to the SM that can realize supersymmetry by requiring minimum number of new particles. Each SM particle has a supersymmetric partner as listed in Table 3.1. It is convention to prefix an "S" to represent the SUSY partner of SM fermions, append a "ino" suffix to SUSY partner of SM bosons, and add a "$\sim$" above the SM particle symbol to represent the SUSY particle. For instance, "Stop" ($\tilde{t}$) is top (t) quark's superpartner, "gluino" ($\tilde{g}$) is gluon's (g) superpartner.

SM particles		Spin	MSSM particles		spin
Quark	q	1/2	Squark	$\tilde{q}$	0
Lepton	l	1/2	Slepton	$\tilde{l}$	0
Gluon	g	1	Gluino	$\tilde{g}$	1/2
B Boson	B	1	Bino	$\tilde{B}$	1/2
W Boson	$W^{\pm}, W^0$	1	Wino	$\tilde{W}^{\pm}, \tilde{W}^0$	1/2
Higgs Boson	H	0	Higgsino	$\tilde{H}$	1/2
R-parity		+1	R-parity		-1

Table 3.1: Standard Model particles and their superpartners in MSSM

MSSM introduces a new quantum number, R-parity, it is defined as:

$$P_R = (-1)^{3\cdot(B-L)+2s} \tag{3.3}$$

where B is baryon number, L is lepton number and s is spin. R-parity is +1 for the Standard Model particles and -1 for their superpartners in MSSM. MSSM is invariant under R-parity. In the collider experiments, the initial state of R-parity is +1, so the SUSY particles must be produced in even numbers, typically production of SUSY particle-antiparticle pairs. Also, the lightest supersymmetric particle (LSP) is completely stable with -1 R-parity, thus it can be a dark matter candidate.

If the perfect symmetry exists, the SUSY particles that have the same masses as the SM particles should have been discovered a long time ago, which is not the case obviously. Therefore, SUSY must be extended with a broken sector. To maintain the "natural" solution to the SM hierarchy problem, only "soft" breaking terms are allowed in MSSM. It is assumed that the SUSY breaking occurs in a "hidden sector" that has no direct couplings to the "visible sector" of the MSSM, the two sectors share interactions via "messengers" that can mediate the breaking to the MSSM. Several SUSY breaking models depending on the interaction type are intensively studied. In this dissertation, we focus on the general-gauge-mediated (GGM) supersymmetry breaking models.

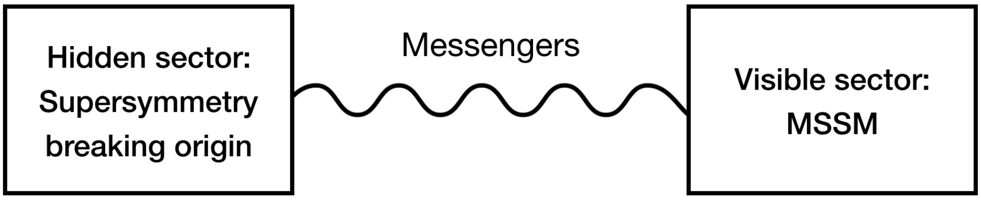

Figure 3.2: The presumed schematic for messengers mediating supersymmetry breaking from the hidden sector to the visible sector.

3.3 Gauge Mediated Supersymmetry Breaking

In this analysis, we are interested in the general gauge mediated supersymmetry breaking (GMSB) scenario [25] [26]. As the name suggested, GMSB uses the SM gauge interactions to communicate the hidden breaking sector with the visible GGM sector. In LHC, with proton-proton collisions, the strong productions are dominant process. The stop squark is assumed to be the lightest squark. Stop pairs decaying leads to the top quark pairs and the next-to-the-lightest supersymmetric particles (NLSPs), where a NLSP decaying to a gravitino ($\tilde{G}$) as a stable LSP.

This analysis concerns the neutralino NLSP cases, specifically the bino-like NLSP. The gauge and mass eigenstates are related as in Table 3.2. In GMSB, the neutralino ($\tilde{\chi}_1^0$) is very bino-like ($\tilde{B}^0$) , its decay branching ratio is dominated by $\gamma + \tilde{G}$, as plotted in Figure 3.3 by using the following formula [27]:

$$\Gamma(\tilde{\chi}_1^0 \to \tilde{G} + \gamma) = \frac{c_W^2}{c_W^2 + s_W^2(1 - \frac{m_Z^2}{m_{\tilde{\chi}_1^0}^2})^4} \tag{3.4}$$

$$\Gamma(\tilde{\chi}_1^0 \to \tilde{G} + Z) = \frac{s_W^2(1 - \frac{m_Z^2}{m_{\tilde{\chi}_1^0}^2})^4}{c_W^2 + s_W^2(1 - \frac{m_Z^2}{m_{\tilde{\chi}_1^0}^2})^4} \tag{3.5}$$

	Gauge Eigenstates	Mass Eigenstates
Neutralinos	$\tilde{B}^0, \tilde{W}^0, \tilde{H}_u^0, \tilde{H}_d^0$	$\tilde{\chi}_1^0, \tilde{\chi}_2^0, \tilde{\chi}_3^0, \tilde{\chi}_4^0$
Charginos	$\tilde{W}^\pm, \tilde{H}_u^+, \tilde{H}_d^-$	$\tilde{\chi}_1^\pm, \tilde{\chi}_2^\pm$

Table 3.2: Gauge and mass eigenstates representations of Neutralinos and Charginos

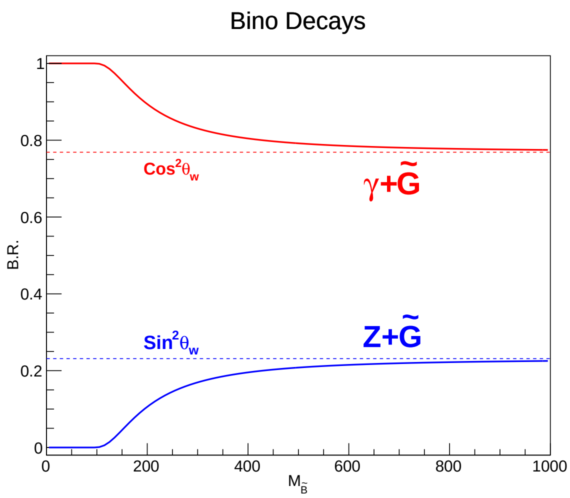

Figure 3.3: Bino decay branching ratios in GGM

The phenomenology of interest to this dissertation of GMSB with R-parity conservation can be summarized as the following features:

- Strong productions of proton-proton collisions lead to stop squark pairs.
- Stop squark decay to top quark and bino-like NLSP.
- Top quark pairs decay semi-leptonically, requiring one of the top quarks decays leptonically by decaying to exact one electron or muon.
- Bino-like NLSPs decay to γ and gravitino ($\tilde{G}$) dominantly.
- Gravitinos leave detector undetected, result as imbalance of energy in events.

These motivate the interest topology as shown in Figure 3.4. It is searched and presented in this dissertation.

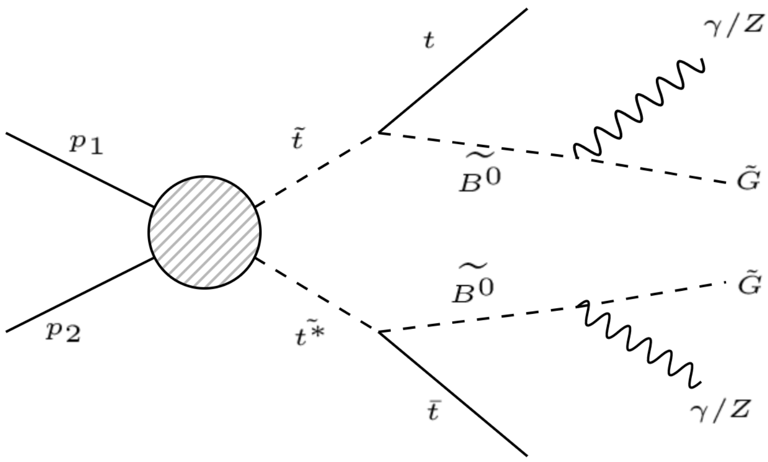

Figure 3.4: Stop pairs production decaying to bino-like neutralinos, leading to the $t\bar{t} + \gamma(Z)\gamma(Z) + E_T^{miss}$ final states in GMSB model.

3.4 Simplified Supersymmetry Model Spectra

To make all the analyses results less model dependent and easily to be compared between each other, the SUSY analysis group has recommended to interpret all results in the simplified supersymmetry model spectra (SMS) [28] [29]. The SMS illustrates the simplest particle spectra, only depends on the particle masses, cross sections and relative branching ratios. The same SMS model can be interpreted by different SUSY models which have the same topologies. Therefore, various analysis can present the limit constraints simultaneously and seek combination further.

Analysis result presented in this dissertation also considers the two compatible SMS topologies T6ttZG and T6ttHG, where the stop pair production yields top quark pair and two NLSPs, each NLSP then decays to 50%γ/50%Z + LSP in T6ttZG and 50%γ/50%Higgs + LSP in T6ttHG as illustrated in Figure 3.5.

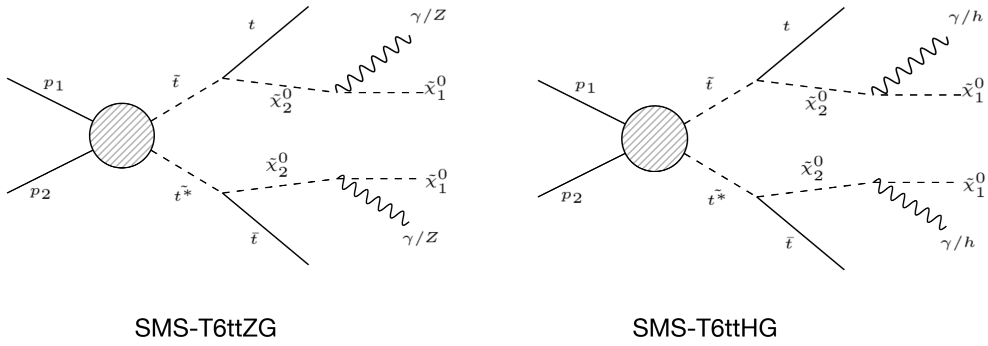

Figure 3.5: Stop pairs production leading to the $t\bar{t} + \gamma(Z,h)\gamma(Z,h) + E_T^{miss}$ final states in SMS models.

3.5 Experimental Status of SUSY on LHC

With the successful commissioning of LHC and data collected during RUNI & RUNII periods, the CMS and ATLAS experiments have analyzed and presented the most updated results for SUSY search. Figure 3.6 shows the summary limits set by CMS [5] and Figure 3.7 shows the limits set by ALTAS [30].

Considering the direct top squark pair productions, the results of these searches interpreted by SMS models on CMS are shown in Figures 3.8. It needs to be clear that these results do not preclude the search presented in this dissertation, as the bino-like NLSP has very different final states and the semi-leptonic channel of top pair has suppressed the SM backgrounds significantly.

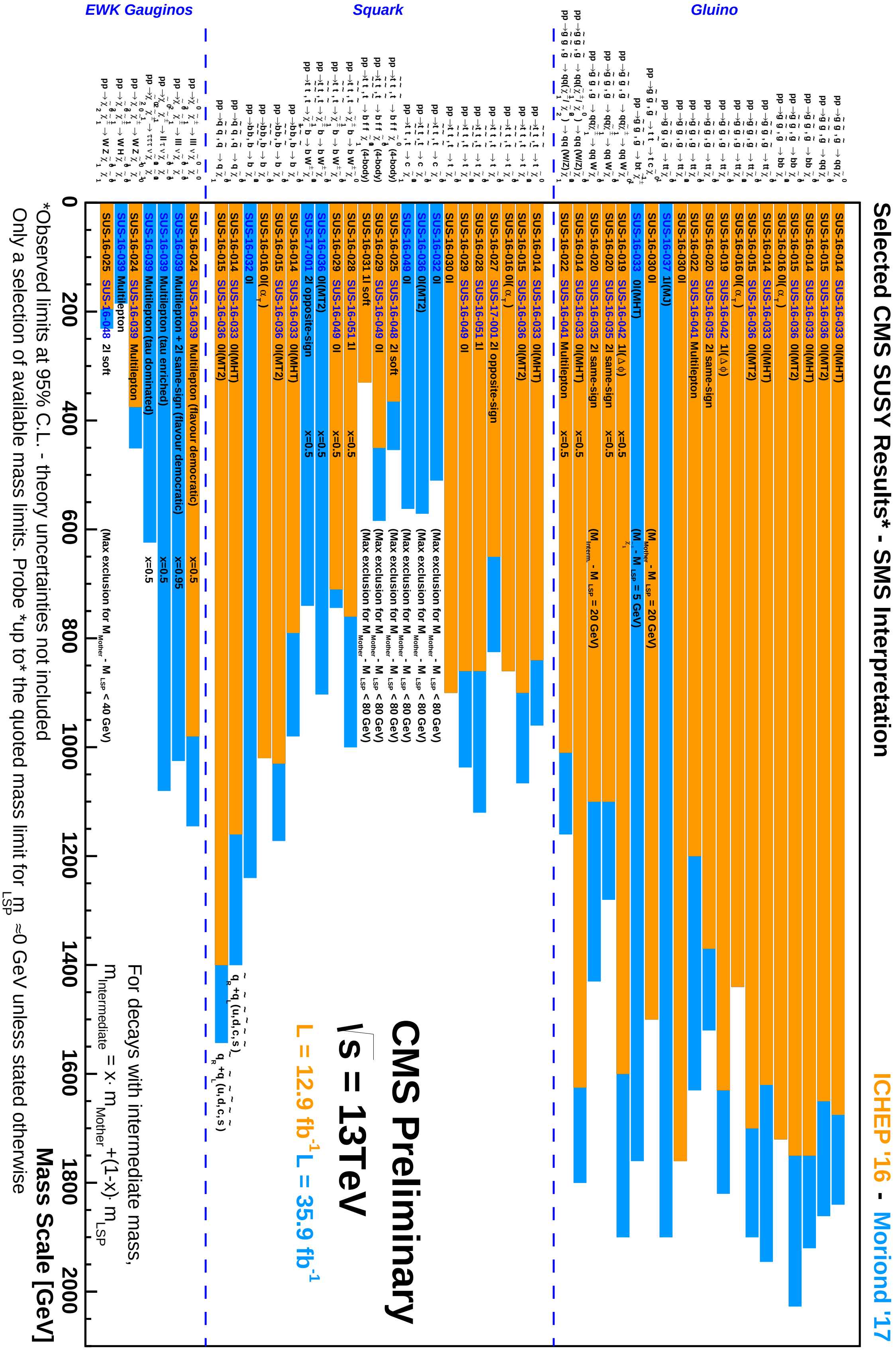

Figure 3.6: Summary of mass limits of CMS SUSY searches.

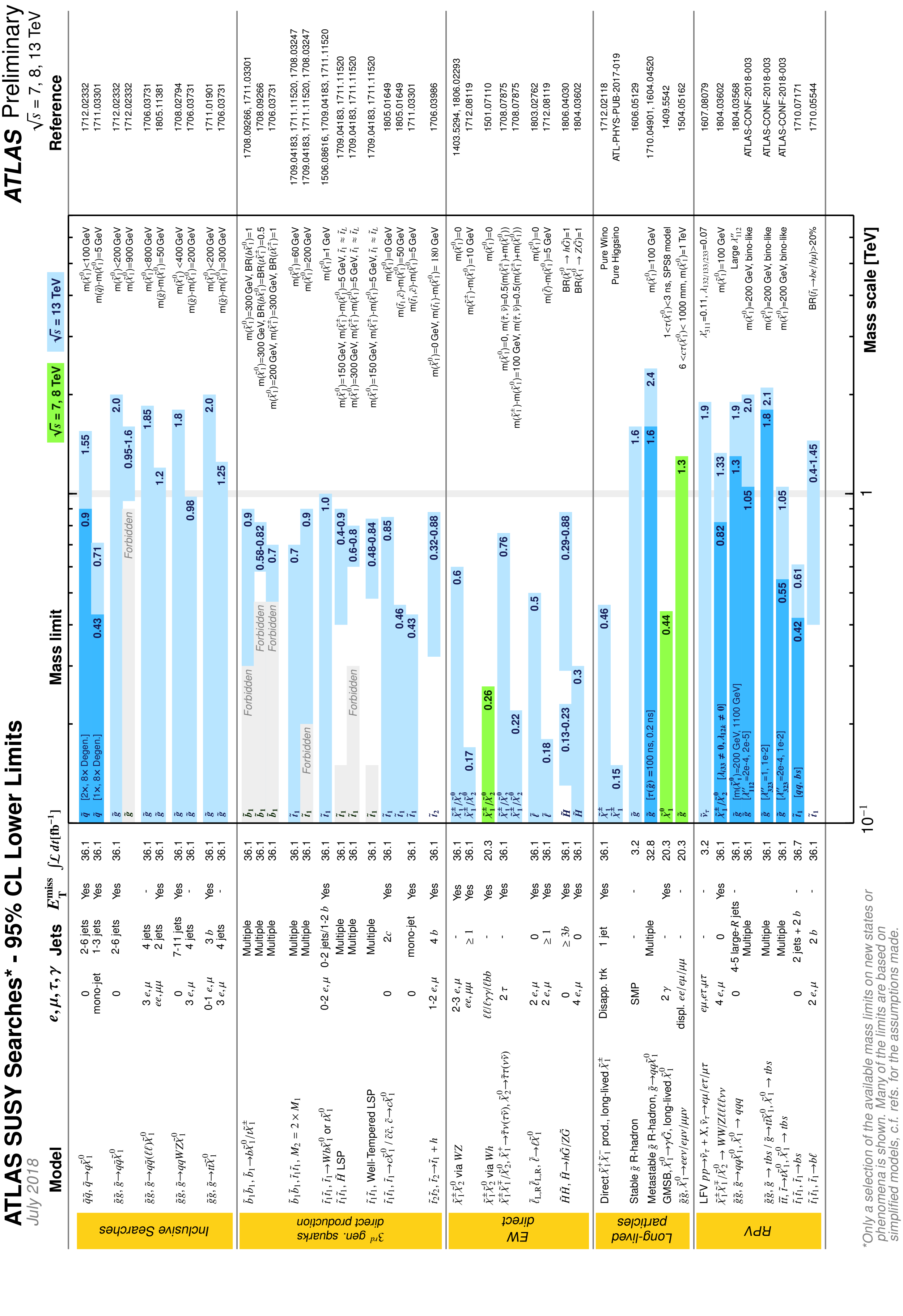

Figure 3.7: Summary of mass limits of ATLAS SUSY searches.

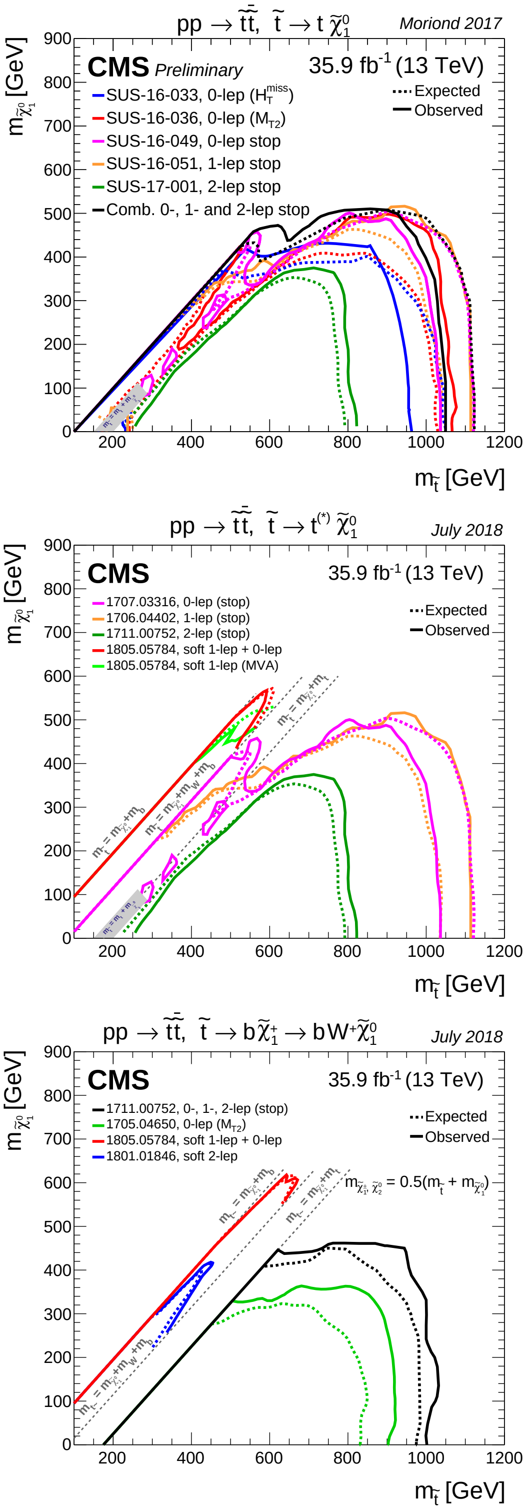

Figure 3.8: The exclusion limits of top squark searches on CMS for simplified model of top squark pair production with squark decays to a on- or off-shell top quark and the LSP, leading to final states with two bottom quarks, two W bosons, and two LSPs (top); with top squark decays via on- or off-shell top quarks and W bosons (middle); with top squark decays via an intermediate chargino ($\tilde{\chi}_1^{\pm}$) or neutralino ($\tilde{\chi}_2^0$) (bottom). Reprinted from reference [5].

Chapter 4

The Compact Muon Solenoid Detector at the Large Hadron Collider

4.1 The LHC

The Large Hadron Collider (LHC) is currently the largest and most powerful proton-proton collider in the world. It is located at the border of France and Switzerland. The LHC has a circumference of 27 kilometers ring tunnel and resides around 50 to 175 meters underground, reusing the tunnel of the LEP e^+e^- collider which was closed in 2000 to make room for LHC. Seven experiments of the LHC analyze data produced by collisions in this accelerator. Four detectors, ATLAS, ALICE, CMS, LHCb, are sited in the huge caverns in the tunnel ring as shown in Figure 4.1. ATLAS and CMS are the two largest and general-purpose experiments.

The principle goal of the LHC is providing high luminosity collisions of proton-proton beams. Luminosity (L) measures the number of collisions produced by the collider in units of $cm^{-2}s^{-1}$. The function used to calculate the collider luminosity can be written as:

$$L_{instant} = \frac{N_1 N_2 f N_b}{4\pi\sigma_x\sigma_y} \cdot W \cdot e^{\frac{B^2}{A}} \cdot S \tag{4.1}$$

where the last three terms are correction factors. S accounts for the beam crossing angle, W corrects the presence of beam offsets and $e^{\frac{B^2}{A}}$ is required when we have a

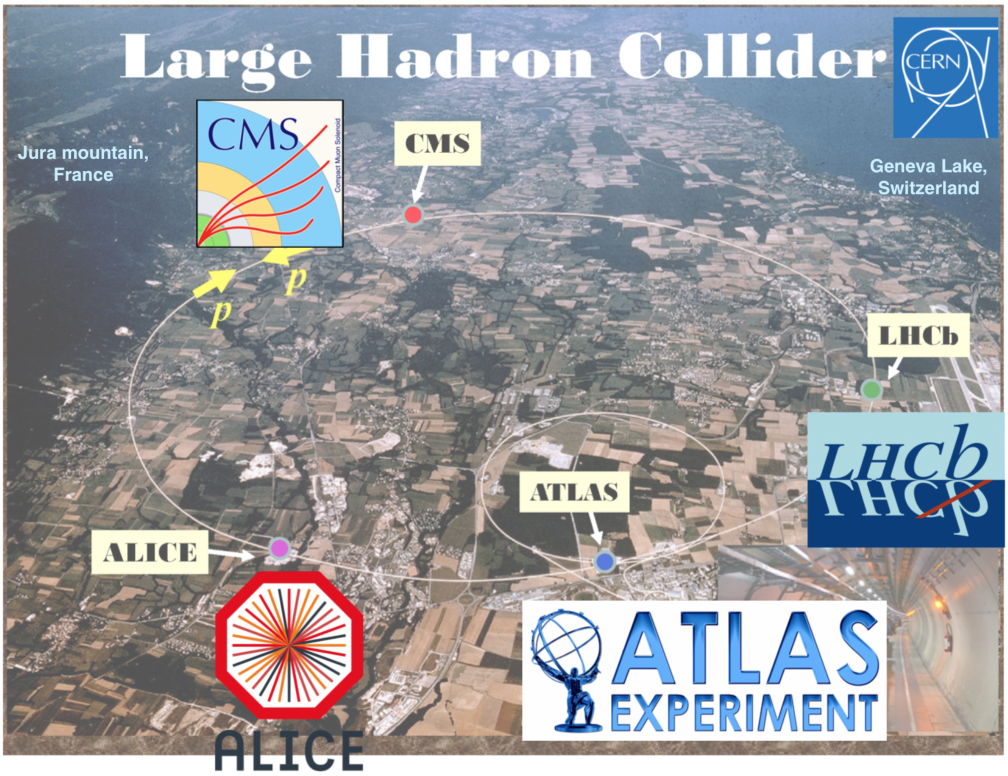

Figure 4.1: The view of LHC ring with the positions of four main experiments and the landmarks of Jura Mountain, France, Lake Geneva, Switzerland marked.

non-zero crossing angle and beam offsets simultaneously. N_1, N_2 are the number of protons/bunch for beam-1 and beam-2, f is the beam revolution frequency, N_b is number of bunches/beam, σ_x, σ_y are the transverse beam sizes.

With the above function, we calculate the instant luminosity. By integrating the instant luminosity over the time, we define the integrated luminosity,

$$L_{integrated} = \int L(t)dt \tag{4.2}$$

which is related to the number of events of physical process P by the following equation,

$$L_{integrated} \cdot \sigma_P = N_{events} \tag{4.3}$$

The integrated luminosity has the unit of cm^{-2}, which can also be expressed in $barns$ ($1b = 10^{-28}m^2$). Figure 4.2 shows the integrated luminosities delivered by LHC through 2018.

The above mathematics is mostly adapted from reference [31], please refer to it for the detailed explanation and calculation of luminosity.

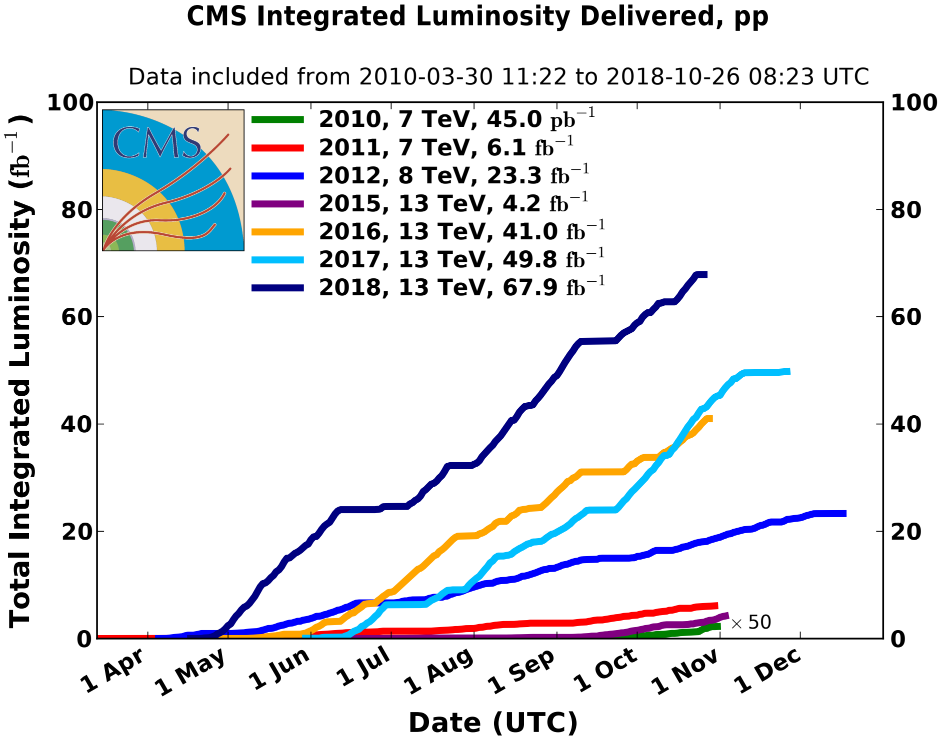

Figure 4.2: The integrated luminosities of pp collision each year delivered by LHC and recorded by CMS. Go to reference [6] for more plots.

Starting from ionized hydrogen gas, protons travel a long way to reach 7 TeV in energy before they collide. The injection complex is shown in Figure 4.3.

The components of accelerator can be simplified into three parts: magnets, to control transverse beam dynamics; radiofrequency cavities, to control longitudinal beam dynamics, giving energy pulses to the proton beams; beam control and monitoring systems. 1232 magnetic dipoles along the beam path control the protons' trajectories. They are composed of superconducting Niobium-Titanium coils cooled below 1.9K and provide a magnetic field up to 8.33 T. The magnetic multipoles are also used for fine control and focusing of the beam. The LHC receives proton bunches injected by the SPS accelerator with energy of 450 GeV and subsequently accelerates the beam to 3.5 - 7 TeV by using 400 MHz superconducting radio-frequency cavities.

The LHC produced its first proton beam in September 2008. The operation of the collider for physics was delayed to later 2009 due to a magnet quenching accident. On March 30th, 2010 two proton beams collided at a center-of-mass

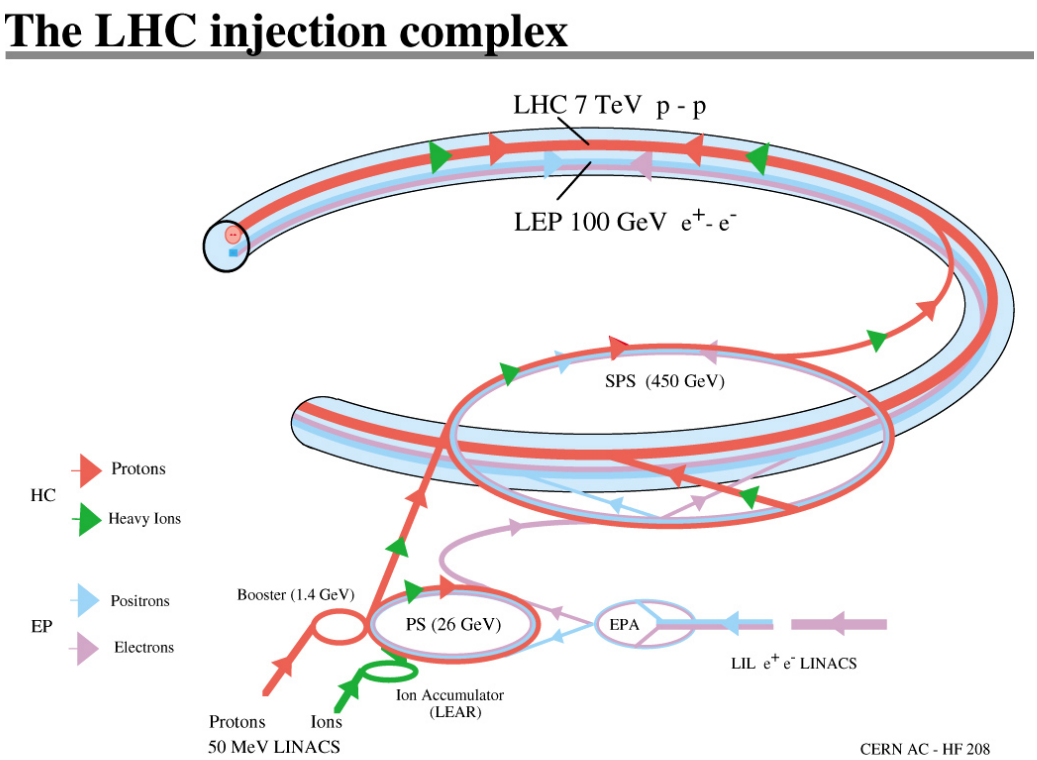

Figure 4.3: The LHC injection complex. Reprinted from reference [7].

energy of 7 TeV, launching the research journey of LHC. During the RunI period from 2009 to 2013, the LHC ran at 7 TeV and 8 TeV. On July 4th, 2012 the Higgs boson discovery was announced.

After two years' maintenance and upgrading work, the LHC was restarted in 2015 starting RunII. On May 20th, 2015 the collider energy was raised to an unprecedented 13 TeV. The peak instantaneous stable luminosity reached $10^{34} cm^{-2} s^{-1}$ in 2016. The total integrated luminosity is about 40 fb^{-1} for 2016, and 50 fb^{-1} for 2017, producing a tremendous amount of data for physics analysis. RunII was completed at the end of 2018. RunIII will begin in 2021, then the high luminosity upgrade of LHC (HL-LHC) is scheduled afterward.

For more about LHC, please refer to its official site: `https://www.lhc-closer.es/taking_a_closer_look_at_lhc/1.lhc`.

4.2 The CMS Detector

The Compact Muon Solenoid (CMS) detector [32] is a general-purpose experiment operating at the LHC. It is sited at the Point 5, close to the French village Cessy, and was assembled above ground and then lowered into the cavern about 100m underground. As the perspective view of the detector shown in Figure 4.4, the detector has $\sim$ 30m overall length and is 15m in diameter. The total weight is about 14000 tons. The layers of its subdetectors cover the complete solid angle around the collision point to measure the particles produced from the collisions. The term "Compact" describes the design to include both the tracker and calorimeters within the solenoid which provides a powerful magnetic field of 3.8 T.

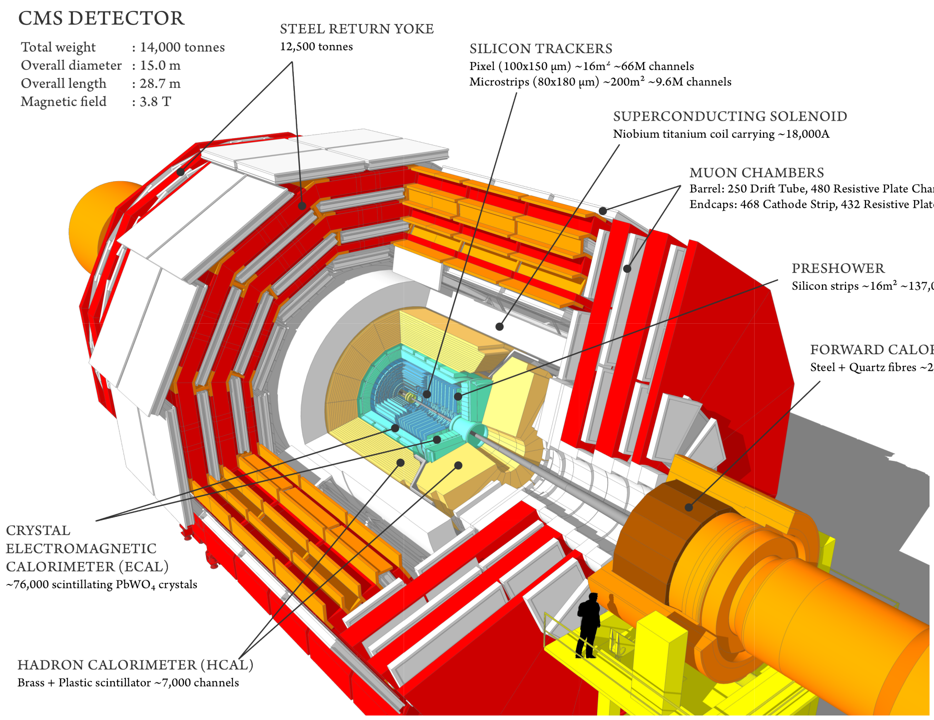

Figure 4.4: The perspective view of the CMS detector. Reprinted from reference [8].

The main components of CMS are the inner tracker system, the electromagnetic calorimeter (ECAL), the hadron calorimeter (HCAL), the superconducting magnet and the muon system. From the center collision point, the first layer is the silicon tracker detector consisting of the innermost pixel to outer microstrip layers, the second layer is the lead tungstate crystal ECAL, and the third layer is the scintillator HCAL. These three layers are designed to be compact and fit inside the cylindrical superconducting solenoid with 12.5 m length and 6 m of internal radius. The powerful magnetic field bends the tracks of charged particles, allowing a measurement of their momenta using the curvature. The outermost muon system consists of three different chambers: drift tubes (DTs), resistive plate capacitors (RPCs) and cathode strip chambers (CSCs). The iron return yokes of the superconducting solenoid are interleaved within these muon stations. The following sections in this chapter will describe all the individual sub-detectors.

All the subdetectors of CMS work together to provide measurements with high resolution of energy, momentum and position, as well as to identify electrons, muons, photons and hadrons. Undetectable particles such as neutrinos can be inferred through the momentum imbalance of the visible particles.

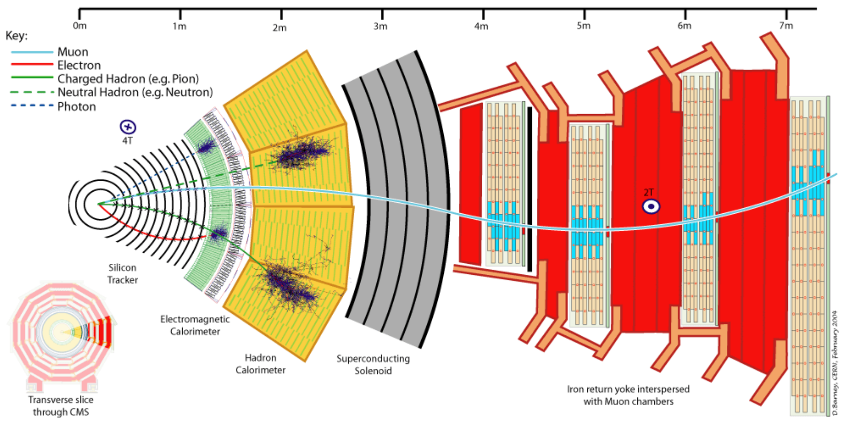

Figure 4.5: The transverse slice of CMS and the examples of ways different particle types are detector by the CMS detector.

CMS uses the nominal interaction point as the origin of the coordinate system. The x axis points horizontally toward the center of the LHC ring, the y axis points vertically upward to the ground surface, and the direction of the z axis is determined along the beam path by the right-hand rule. In cylindrical polar coordinates, the polar angle θ is measured from the positive z axis and the azimuthal angle ϕ is measured from the positive x axis in the x-y plane. The pseudorapidity is defined as $\eta = -\text{In}[tan(\theta/2)]$. The angular separation of particles is defined by the cone radius ΔR, calculated using $\Delta R = \sqrt{(\Delta\phi)^2 + (\Delta\eta)^2}$. Transverse energy E_T, transverse momentum p_T and the imbalance of transverse momentum P_T^{miss} are measured in the x-y plane.

There are over 4000 scientists and students from around 200 institutes and universities of more than 40 countries working on CMS as a collaboration.

4.2.1 Inner Tracker System

The tracker system [33] [34] measures the tracks of charged particles. As the inner most layer is closest to the beam pipe, both high granularity and high resistance to radiation damage are required. It needs to be lightweight to minimize disturbance to the particles while maintains the ability to measure positions accurately and promptly. The final design of the tracker is fully silicon-based to meet all these criteria.

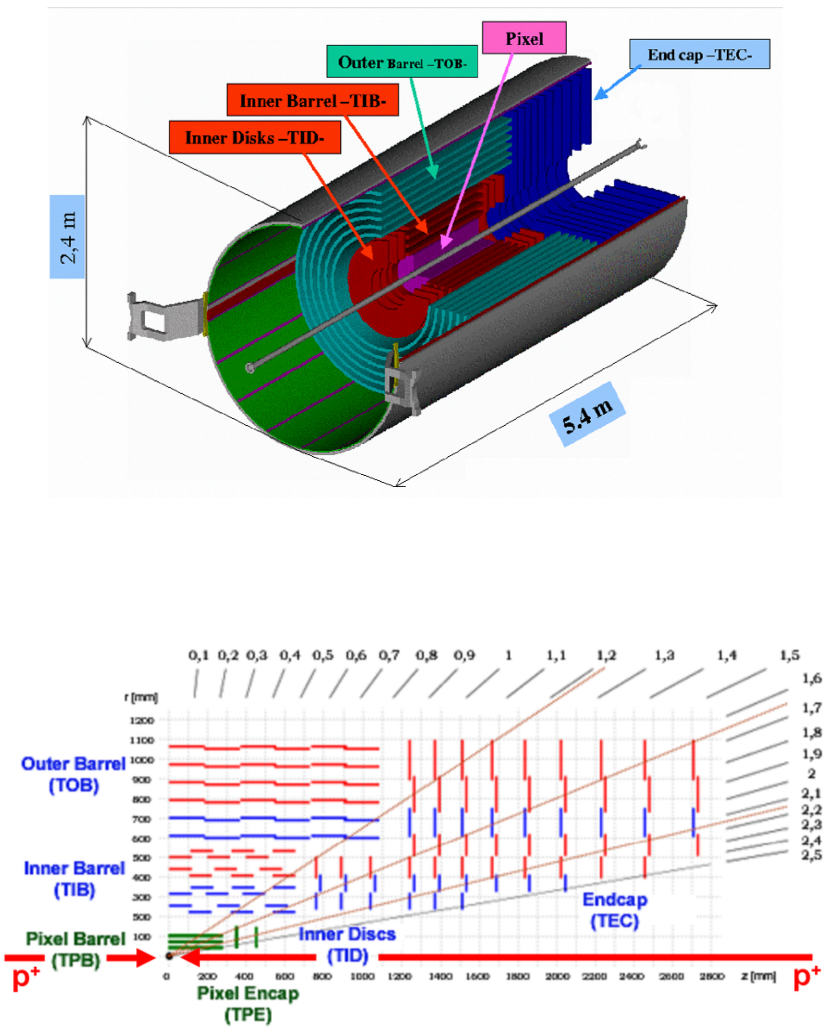

Figure 4.6: The CMS tracker layout in a 3-D view (top), and a 2-D view (side) in the R-z plane. Reprinted from Figure 2 in reference [9].

The tracker system consists of the silicon pixel detector and the silicon strip detector with independent cooling, powering and read-out schemes, covering a pseudorapidity range of $|\eta| < 2.5$. As illustrated in Figure 4.6, the pixel detector, with a surface area of 1.1 m^2, is made of three layers Pixel Barrel (TPB) and two layers Pixel Endcap (TPE) on each side of the barrel. The strip detector, covering about 200 m^2 area, is composed of the Tracker Inner Barrel (TIB), and the Tracker Outer Barrel (TOB), whereas the endcap disks are made of the Tracker inner Disks (TID) and the Tracker End Caps (TEC), total 10 layers in the barrel region and 12 disks in the endcap region.

Within the 3.8 T magnetic field generated by the solenoid, the tracks of charged particles are bent and their curvatures are measured by connecting the hit points on the silicon layers. For 2011 pileup conditions [35], the average track-reconstruction efficiency for promptly-produced charged particles with transverse momenta of $P_T > 0.9$ GeV is 94% for pseudorapidities $|\eta| < 0.9$ and 85% for $0.9 < |\eta| < 2.5$. The tracker system also provides the vertex reconstruction. The position resolution of reconstructed primary vertices is 10-12 microns in each direction of the 3D dimensions.

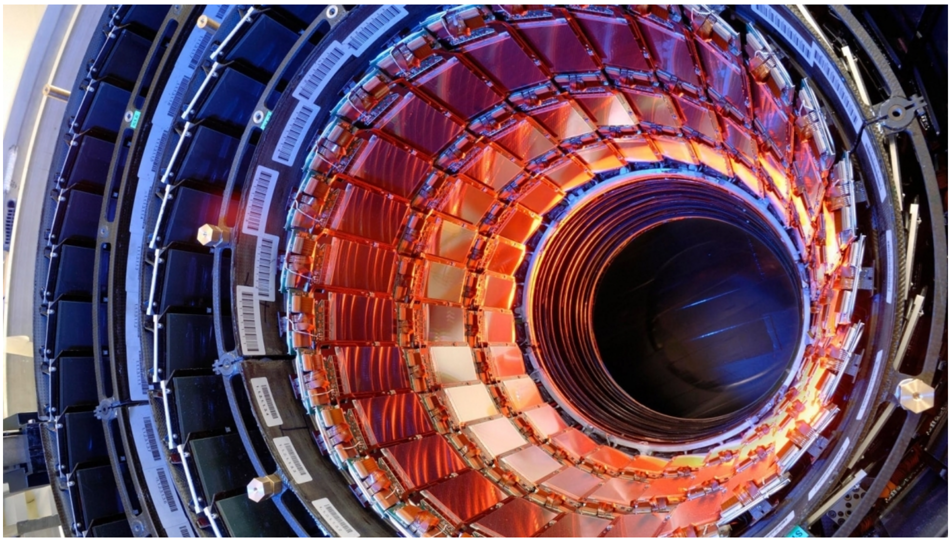

Figure 4.7: The silicon strip detectors in the barrel module of CMS Tracker.

4.2.2 Electromagnetic Calorimeter

The Electromagnetic Calorimeter (ECAL) [36] [37] provides the high-precision measurement of energy and position of electrons/positrons and photons, which are critical to this analysis and to Higgs analysis especially for the $H \rightarrow \gamma\gamma$ channel. The ECAL is a single-layer crystal calorimeter as shown in Figures 4.8 and 4.9.

It consists of a barrel (EB) and two endcaps (EEs). There is a preshower detector (ES) standing in front of each EE. The barrel covers the pseudorapidity range $|\eta| < 1.479$. It is made of 61200 crystals grouped as 36 supermodules. Each crystal is $2.2 \times 2.2 \times 23\,cm^3$. The Endcaps covering the range $1.479 < |\eta| < 3.0$, are built as 4 Dees (2 per EE) that made of total 14648 crystals, each is $3 \times 3 \times 23\,cm^3$. All crystals are kept within 0.1 °C of their optimum temperature to ensure stable and equal response.

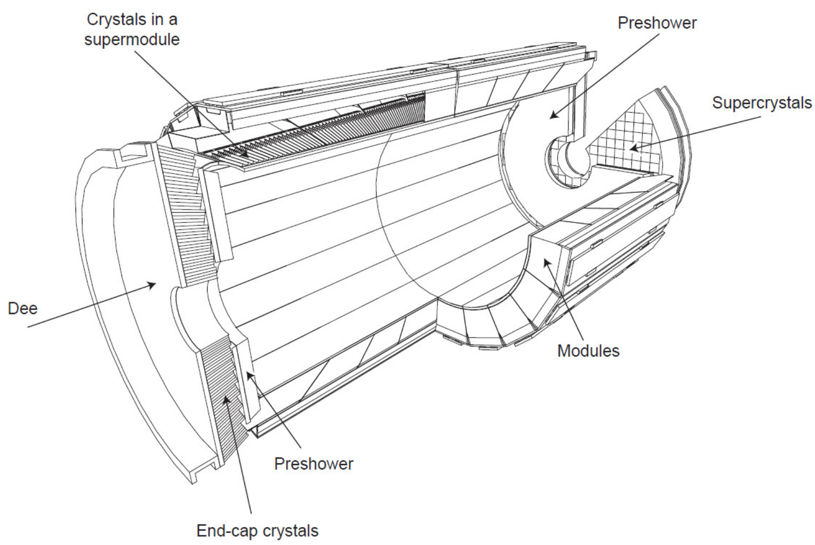

Figure 4.8: Layout of the ECAL.

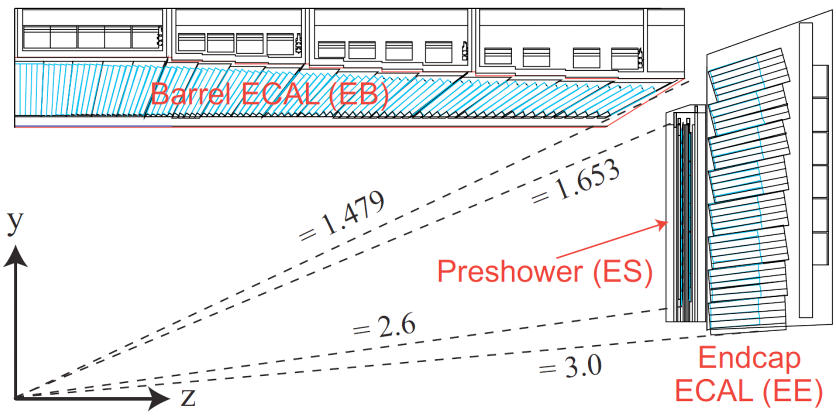

Figure 4.9: The geometric view of one quarter of CMS ECAL.

The highly performant ECAL requires quick response, fine granularity while working in high radiation and magnetic field. Also, it needs to be compact to fit inside the solenoid. Considering all these aspects, Lead tungstate ($PbWO_4$) crystal was chosen. $PbWO_4$ is a transparent, high density material ($8.3g/cm^3$) with a short radiation length ($X_0 = 0.89cm$). About 80% of its scintillation light is emitted within 25 ns, which corresponds to the designed bunch-crossing time. The amount of light generated in a crystal is proportional to the energy that is deposited. The scintillation light is collected by photon detectors with internal amplification. At the rear of each crystal, there is a pair of silicon avalanche photondiodes (APD) in the EB or a single vacuum phototriode (VPT) in the EE as shown in Figure 4.10 to measure the scintillation light. The amplified electronic signal is then recorded by the data acquisition system. By analyzing the data collected from the test beam, radioactive source and cosmic-ray, the ECAL crystal-to-crystal energy response is calibrated. Due to radiation effects, the crystal transparency varies with exposure to the integrated interactions and must be monitored by the laser system and the parameters are corrected when changes are observed. In RunII, the ECAL laser corrections are typically performed once to twice a week.

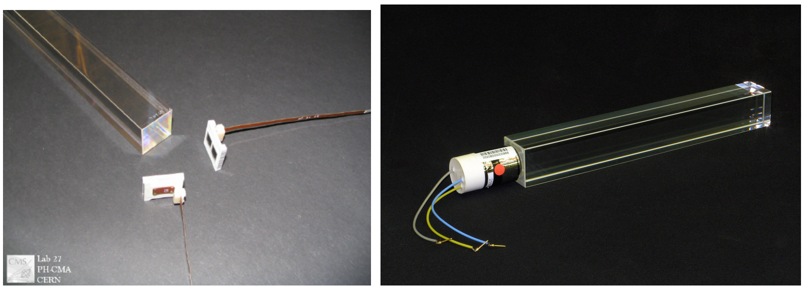

Figure 4.10: EB crystal and APD (left), EE crystal with attached VPT (right).

The preshower detector located in front of each endcap, covers the $1.653 < |\eta| < 2.6$. It consists of lead absorbers and silicon detector layers to provide a better angular resolution to distinguish between single high-energy photons and closely separated pairs of low-energy photons from neutral pion decay.

4.2.3 Hadronic Calorimeter

The Hadronic Calorimeter (HCAL) measures the energies and positions of charged and neutral hadrons, it also provides an indirect measurement of non-interacting and uncharged particles such as neutrino by calculating the imbalance of conservative parameters. The HCAL [38] must be both hermetic and compact to fit within the CMS solenoid. It should have reasonable energy resolution with depth segmentation to form a sampling calorimeter. The HCAL is built in barrel (HB), barrel outer (HO), endcap (HE) and forward (HF) sections. There are 36 HB wedges. The HO stands outside the coil to cover energy leaks outside HB undetected. Two HFs sit at each end of CMS. One quadrant of HCAL and the corresponding pseudorapidity of each section are illustrated in Figure 4.11.

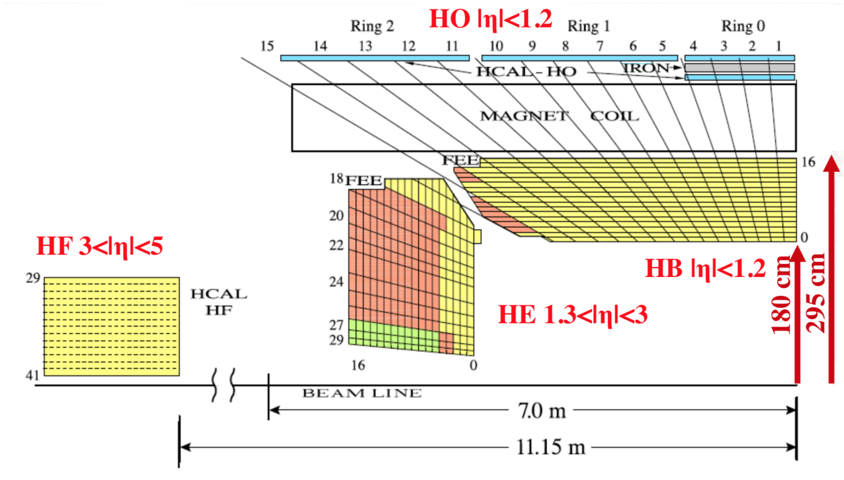

Figure 4.11: The layout of a quadrant of HCAL in longitudinal view.

The sampling calorimeter is made of alternating layers of brass absorber plates and plastic scintillator megatiles as illustrated in Figure 4.12. The incident hadron generates hadronic showers in the absorber, then charged particles in the shower produce scintillation light in the plastic scintillator. The scintillation light is collected by the wavelength-shifting fibre (WLS) and transported to hybrid photodiodes (HPD).

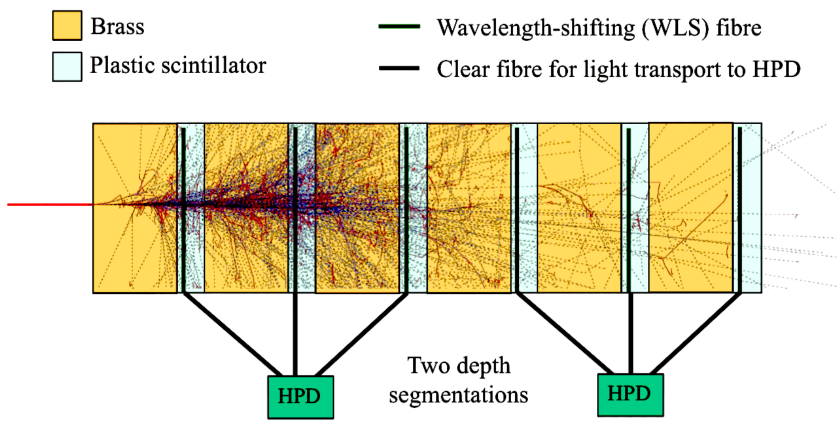

Figure 4.12: The schematic of sampling calorimeter with two-depth segmentations, reprinted from reference [10].

The two HFs stand at both end of CMS covering the high pseudorapidity range $3 < |\eta| < 5$ to measure the particles traveling near the beam line. It is made of steel absorber with Cerenkov-producing quartz fibers and is more radiation resistant than the other parts of HCAL. The CMS online luminosity measurement relies on the forward hadronic calorimeter (HF) "HF lumi".

4.2.4 Muon System

The muon system [39] is the outermost subdetector of CMS. As the name "CMS" suggests, detecting muons is one of the most important goals. Muon can penetrate through the inside subdetectors with minimal interaction. They are measured by fitting the curved path to its hit points through multiple layers of muon stations and combining these with Tracker measurements. The muon system consists of three components, drift tubes (DT) in the barrel section, cathode strip chambers (CSC) in the endcap section, and resistive plate chambers (RPC), as shown in Figure 4.13. These chambers are interleaved with the iron return yoke plates and the muon system are immersed in a magnetic field of ~ 2 T.

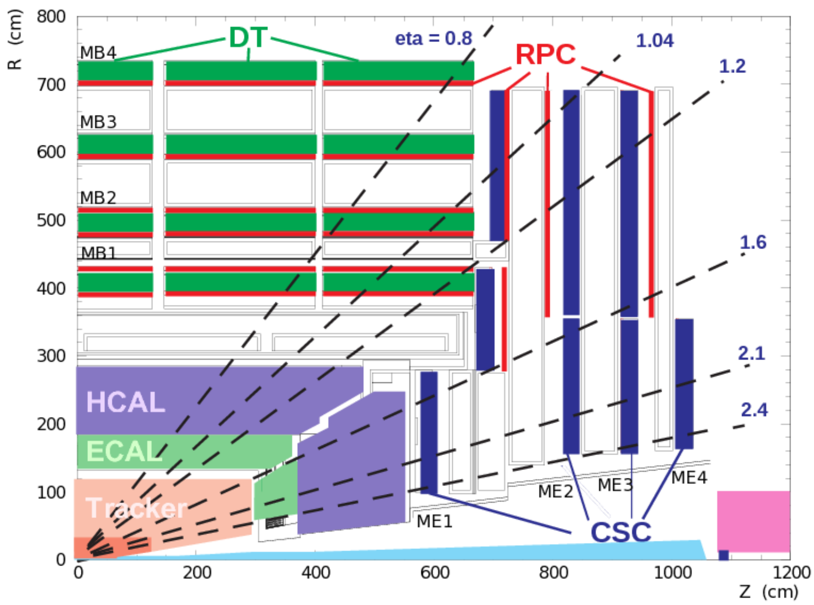

Figure 4.13: The quadrant view of the muon detector in CMS. Reprinted from reference [11].

The drift tube system measures muon positions in the barrel area, covering the range of $|\eta| < 1.2$. When a muon passes through a DT, it knocks electrons off the atoms of the gas, then those electrons drift to the positively-charged wire and are converted to the two coordinates of the muon's position.

The cathode strip chambers are installed in the endcap disks due to the high particle incident rates and uneven magnetic field. The CSC is made of arrays of positively-charged wires perpendicular to negatively-charged copper strips within a gas environment. The passing muon ionizes the gas atoms and its position is measured by the strips and wires. The closely arranged wires and strips and six layers of each CSC module provide precise position and timing information to accurately identify muons and match their tracks in the Tracker.

The resistive plate chambers are gaseous parallel-plate detectors made of high resistivity plastic material as shown in Figure 4.14. The muons pass through the gas chamber will result into an avalanche of electrons and further picked by the external detecting strips. The very quick response is then used by the online trigger system to make prompt decisions about whether saving the data or not.

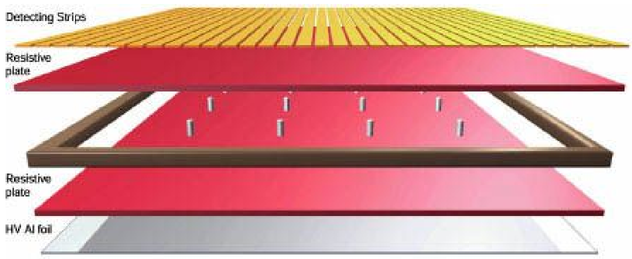

Figure 4.14: The schematic view of RPC layers.

4.2.5 Trigger and Data Acquisition

When operating at the nominal luminosity of $10^{34} cm^{-2} s^{-1}$ with 25 ns bunch-crossing separation, there is an average of 20 interactions/crossing which equivalent to nearly 1 billion events/second. Due to the huge data volume and high delivery speed, it is beyond the capability to store all the collisions for analysis. Therefore, the two level trigger system [40] consisting the Level-1 (L1) trigger and the high level trigger (HLT) are designed to pick only potentially interesting events. The L1 trigger system does a quick scan and reduces the output event rate to 100 KHz from the 40 MHz bunch-crossing rate. Its decision based on the muon trigger and calorimeter triggers by quickly finding objects like jets, electrons to reject events in

3.2 μs. L1 trigger works on custom hardware and firmware. Exceeding the limit rates can result in deadtime. Figure 4.15 shows the architecture of the L1 trigger system.

In the second step, the high level trigger reconstructs the events fed into by L1 trigger, using full detector information by applying the customized CMS analysis software reconstruction algorithms. As the consequence, only about 100 Hz events are stored for further study. HLT system is performed on the CPU farm which builds on thousands standard computers. The HLT menu is written and adjusted according to the running status. Finally, only one in 10^7 events produced in CMS is recorded and all the other rejected events are discarded forever. There are dedicated monitoring system to keep watching on the online trigger rates in case of high rates which might result in Data Acquisition (DAQ) suspension and data losing reluctantly.

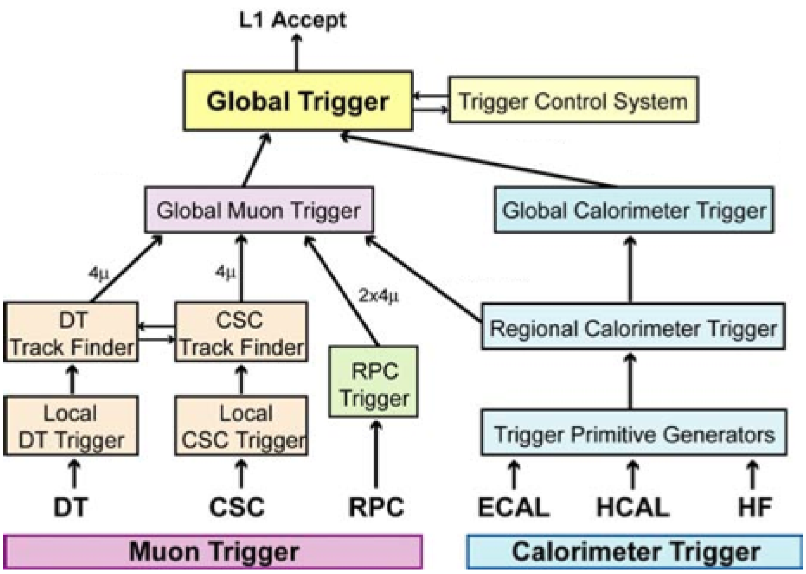

Figure 4.15: CMS L1 trigger decision flow chart.

Chapter 5

Event Reconstruction

5.1 Particle-Flow Event Reconstruction

All the raw data collected by the CMS detector needs to be reconstructed to physical quantities and physical objects before it can be used for further analyses. The Particle-Flow (PF) algorithm [41] [42] is one of the event reconstruction schemes that deployed in CMS. This section is summarized from reference [41]. The PF reconstruction combines the information from all sub-detectors to give an optimal reconstruction and identification of all stable particles in events, including muons, electrons, photons, charged hadrons and neutral hadrons.

The fundamental elements for PF algorithm are charged-particle tracks, calorimeter clusters and muon tracks. The charged-particle tracks provide the precise momentum measurements and direction measurements by requiring the high tracking efficiency and low fake rate. An iterative-tracking strategy is applied. The tracks are firstly seeded and reconstructed with very tight cuts. The next step removes hits assigned to the tracks reconstructed in the previous step. The iteration proceeds by loosing the seeding cut while removing prior assigned hits. Starting at very tight seeding criteria and removing assigned hits for future iterations keep the low fake rate. The progressively loosing criteria increase the eventual tracking efficiency.

The calorimeter clustering algorithm is designed to measure stable neutral particles' energy and direction such as photons and neutral hadrons; distinguish neutral particles from charged hadrons' energy depositions; reconstruct and identify electron with associated Bremsstrahlung photons; and help measure the energy of charged hadrons for which are not accurately determined by the track algorithm [41]. The clustering algorithm proceeds in three steps. The local calorimeter cells with the maximum energy above a given threshold are identified as "cluster seeds", then the "topological clusters" are grown from these seeds by aggregating adjacent cells with a minimum energy threshold requirement. The "topological clusters" provide seeds to the "particle-flow clusters".

Finally, single particles are reconstructed by linking the PF elements avoiding double counting. The tracks and clusters are linked if a track's extrapolation falls into a calorimeter cluster boundary. The two calorimeter clusters are linked when the cluster of more granular calorimeter is within the cluster envelope of less granular calorimeter. For instance, an ECAL cluster is linked to an HCAL cluster when the ECAL cluster is within the envelope of that HCAL cluster since ECAL has more granular and accurate measurement than HCAL. A charged-particle track and a muon track are linked when they return the smallest χ^2 within a certain threshold by global fit, and a global muon is reconstructed accordingly. The reconstructions of different particle types are described in the following sections.

5.2 Muon Reconstruction

Muons are first particles reconstructed among all types of particles. By linking the charged-particle tracks in the Tracker system and the tracks in the muon system, the "global muon" is identified. If the momentum of a global muon is consistent with the momentum measured from the Tracker system within 3σ, it is further identified as a "Particle-Flow muon", and its track are removed from PF candidates for use in the subsequent reconstruction.

5.3 Electron Reconstruction

Electrons are reconstructed and identified after muons. Electrons leave tracks in the Tracker system and deposit energies in ECAL. Due to the Bremsstrahlung in the Tracker layers, electrons tend to lose energy before arriving the calorimeter, and have short tracks. Electron tracks are refitted with the Gaussian-Sum Filter (GSF) [43] algorithm to build the trajectories all the way to ECAL. The linked tracks and ECAL clusters including the clusters from Bremsstrahlung photons are labeled as “Particle-Flow Electron” and are removed from further reconstruction processes.

5.4 Photon Reconstruction

Photons are primarily reconstructed from the ECAL clusters that are not matched to any tracks. The crystals with the energies deposited above a threshold are clustered according to the size and shape expected for a photon, and give rise to the “Particle-Flow photon”.

5.5 Jet Reconstruction

Jets are the products of the quarks or gluons, and are detected as the collimated spray of hadrons and hadron decay products. All particles reconstructed with the particle-flow algorithm without being identified in previous particle types, are clustered into “Particle-Flow jets” by associating the elements in a spray. Anti-kt algorithm (AK) algorithm [44] is the CMS default set and used in this analysis. This algorithm iteratively finds each pair of two particles in a event which is closest in the distance d_{ij} weighted by their momenta, and combines them into one object. This process is repeated until $d_{ij} > min(\frac{1}{p_{Ti}^2}, \frac{1}{p_{Tj}^2})$ for each jet pair. This algorithm tends to have high P_T particles clustered first.

$$d_{ij} = min(\frac{1}{p_{Ti}^2}, \frac{1}{p_{Tj}^2})\frac{\Delta_{ij}^2}{R^2} \tag{5.1}$$

where $\Delta_{ij}^2 = (y_i - y_j)^2 + (\phi_i - \phi_j)^2$ is the distance in the $y - \phi$ plane, R is the distance parameter, measured as the cone radius $\sqrt{\Delta\eta^2 + \Delta\phi^2}$.

This analysis selects jet objects reconstructed to “AK4PFJet” within the cone size of radius $R = 0.4$.

5.5.1 b Tagging

B tagging is a reconstruction technique based on the tracks, secondary vertex, soft lepton information and their combination, that distinguishes jets originated from b-quarks. Comparing to the jets due to hadronization of light quarks and gluon, the b jet tends to have long lifetime, large mass, high track multiplicity, large semileptonic decay ratio. Combined Secondary Vertex (CSV) algorithm involves the use of secondary vertices with other lifetime information to provide the discrimination. Each jet is calculated a “likelihood” value and a specific cut is used to select btagged jet. Thus, the possible maximum b-tagging efficiency is not limited to the reconstruction efficiency of the secondary vertex. The version 2 of CSV algorithm (CSVv2) is used in this analysis.

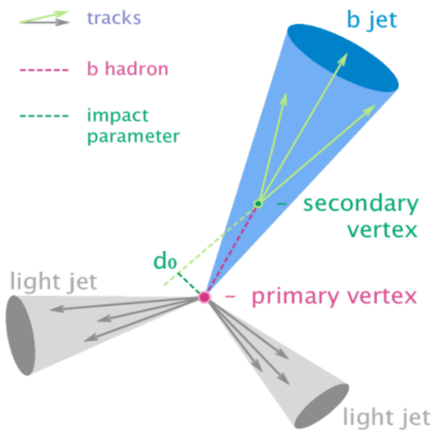

Figure 5.1: Illustration of b jet structure. Reprinted from reference [12].

5.6 Missing Transverse Momentum Reconstruction

The particles such as the Standard Model neutrinos that do not interact with the detector materials will leave no trace that can be detected directly. In addition, some potential BSM particles may also not interact. The existence of such invisible particles will produce an imbalance of the total transverse reconstructed momentum. The momentum imbalance is the missing transverse momentum P_T^{miss} and its magnitude is the missing transverse energy E_T^{miss}. After all PF candidates are reconstructed and identified, the particle-flow P_T^{miss} is defined as the negative vector sum of all reconstructed particle-flow particles’ transverse momenta.

$$P_T^{miss} = -\sum_i \overrightarrow{P_{Ti}} \tag{5.2}$$

$$E_T^{miss} = |-\sum_i \overrightarrow{P_{Ti}}| \tag{5.3}$$

Chapter 6

Data Analysis

6.1 Analysis Overview

As discussed in Section 3.3, we are motived by the GMSB scenario in which the strong production of top squark pairs yields events with top quark pairs and pairs of neutralinos where each neutralino decays to a photon and an undetected gravitino which leads to the significant missing transverse momentum. To eliminate the backgrounds from the SM QCD processes, we require the semi-leptonic decay of the top pairs by selecting events with jets and either an electron or a muon. In addition, we require the presence of at least one energetic photon in the final state. The example topology of an event with two photons and MET in the final states while the top pair decays semi-leptonically is illustrated in Figure 6.1.

Several SM processes can produce or mimic the interesting final state. For instance, the electron and jet can be mis-identified as photon. We use the simulated events to evaluate the SM backgrounds. The $t\bar{t}\gamma(\gamma)$ and $t\bar{t}jets$ productions are considered as the dominant backgrounds; $W\gamma$, $Z\gamma$, Zjets are considered as the sub-dominant backgrounds; and $t\bar{t}+W/Z$, Wjets, Di-boson, single top are included as the other minor backgrounds. Figure 6.2 shows example background processes.

This analysis is performed in two channels, electron channel and muon channel. The single lepton High-level triggers (HLT) have been used to collect data. Two signal regions are further defined by having exact one or ≥ 2 selected photons.

The electron channel has more contribution from the $Z \rightarrow ee$ process where the electron is misidentified as a photon than the muon channel. No such background is

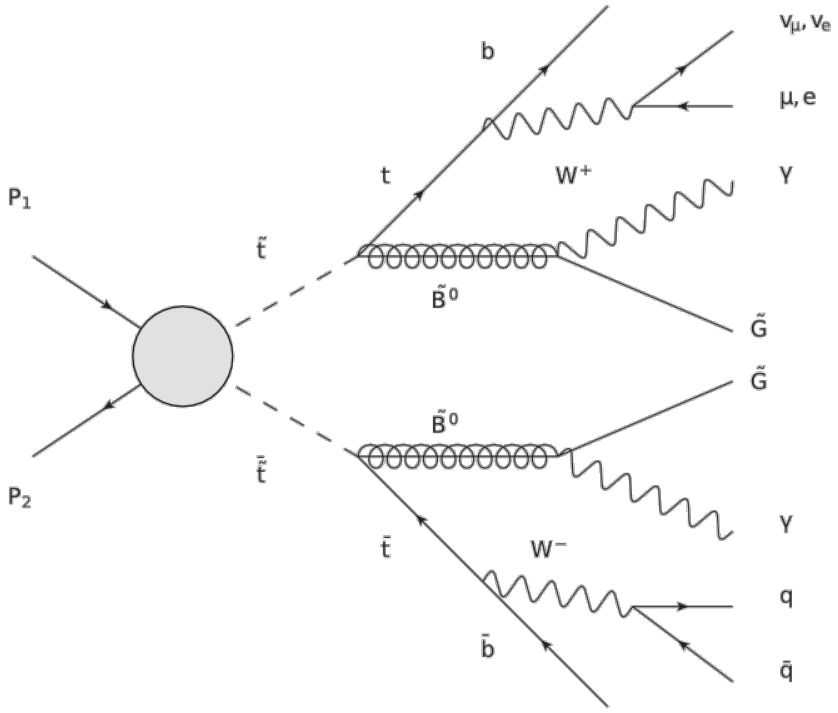

Figure 6.1: An example Feynman diagram for the GGM SUSY pair-production of stop squarks and subsequent decay of the sparticles and top quarks.

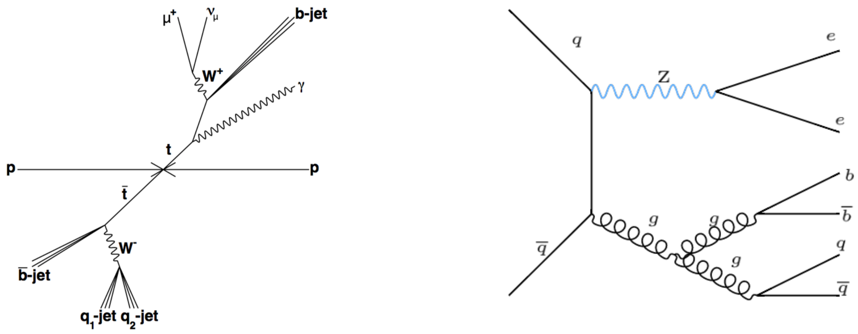

Figure 6.2: Examples of backgrounds: $t\bar{t}jets$ (left) and Zjets (right).

present in the muon channel. In addition, a jet can be misinterpreted as a photon. Since this misidentification happens in both data and simulation, the difference of the misidentification rates need to be adjusted. This difference is studied with $t\bar{t}jets$ and $t\bar{t}\gamma$ samples, and simulated events are normalized accordingly.

Finally, we compare the missing transverse momenta of these events against the expected spectrum of Standard Model processes to search for evidence of supersymmetry, and the results are interpreted as upper limits at the 95% confidence level for the top squark and bino-like NLSP mass-plane.

6.2 Data and Simulation

6.2.1 Data Samples

The datasets used in this analysis correspond to the full 2016 dataset of 35.87 fb^{-1} at $\sqrt{s}$ = 13 TeV. The data were centrally reprocessed with `CMSSW_8_0_X` [45] and analyzed with ROOT [46] trees generated in `CMSSW_8_0_26_patch1`. ROOT is a data analysis framework in high energy physics, CMSSW is the collection of data processing software designed for CMS experiment. Table 6.1 lists in detail each dataset based on the triggers used to collect the events. And the luminosities are calculated for the 2016 data taking period which have a 2.5% uncertainty. To make sure every sub-detector is performing well when taking data, and to certify the events quality for data analysis, the ID numbers of certified events are stored in a JSON format file. The integrated luminosity of 35.87 fb^{-1} of this analysis includes only good quality data that has been certified in the JSON file while masking out poor quality events.

Dataset	Run Range	Integrated Luminosity (fb^{-1})
/SingleMuon/Run2016B-03Feb2017_ver2-v2/MINIAOD	273150–275376	5.78
/SingleMuon/Run2016C-03Feb2017-v1/MINIAOD	275657–276283	2.57
/SingleMuon/Run2016D-03Feb2017-v1/MINIAOD	276315–276811	4.25
/SingleMuon/Run2016E-03Feb2017-v1/MINIAOD	276831–277420	4.01
/SingleMuon/Run2016F-03Feb2017-v1/MINIAOD	277772–278808	3.10
/SingleMuon/Run2016G-03Feb2017-v1/MINIAOD	278820–280385	7.54
/SingleMuon/Run2016H-03Feb2017_ver2-v1/MINIAOD	281613–284035	8.39
/SingleMuon/Run2016H-03Feb2017_ver3-v1/MINIAOD	284036–284044	0.22
Total SingleMu	273150–284044	35.87
/SingleElectron/Run2016B-03Feb2017_ver2-v2/MINIAOD	273150–275376	5.79
/SingleElectron/Run2016C-03Feb2017-v1/MINIAOD	275657–276283	2.57
/SingleElectron/Run2016D-03Feb2017-v1/MINIAOD	276315–276811	4.25
/SingleElectron/Run2016E-03Feb2017-v1/MINIAOD	276831–277420	4.01
/SingleElectron/Run2016F-03Feb2017-v1/MINIAOD	277772–278808	3.10
/SingleElectron/Run2016G-03Feb2017-v1/MINIAOD	278820–280385	7.53
/SingleElectron/Run2016H-03Feb2017_ver2-v1/MINIAOD	281613–284035	8.39
/SingleElectron/Run2016H-03Feb2017_ver3-v1/MINIAOD	284036–284044	0.22
Total SingleElectron	273150–284044	35.87
JSON		Integrated Luminosity (fb^{-1})
Cert_271036-284044_13TeV_23Sep2016ReReco_Collisions16_JSON.txt		35.87

Table 6.1: List of datasets and JSON files used in this analysis.

6.2.2 Signal Samples

To study the expected SUSY signal distribution, a two dimensional Monte Carlo signal scan was produced centrally using the simplified model framework T6ttZG as described in section 3.4. T6ttZG model assumes squark pair production. It produces events in bins of top squark mass and neutralino (NLSP) mass as shown in Figure 6.3. In T6ttZG signal samples, the NLSP is forced to decay to the LSP with a $\gamma(50\%)/Z(50\%)$ ratio, so a branching ratio reweighting is required to make the NLSP bino-like in GMSB model where the bino decay branching ratio is calculated according to the bino mass as described in section 3.3.

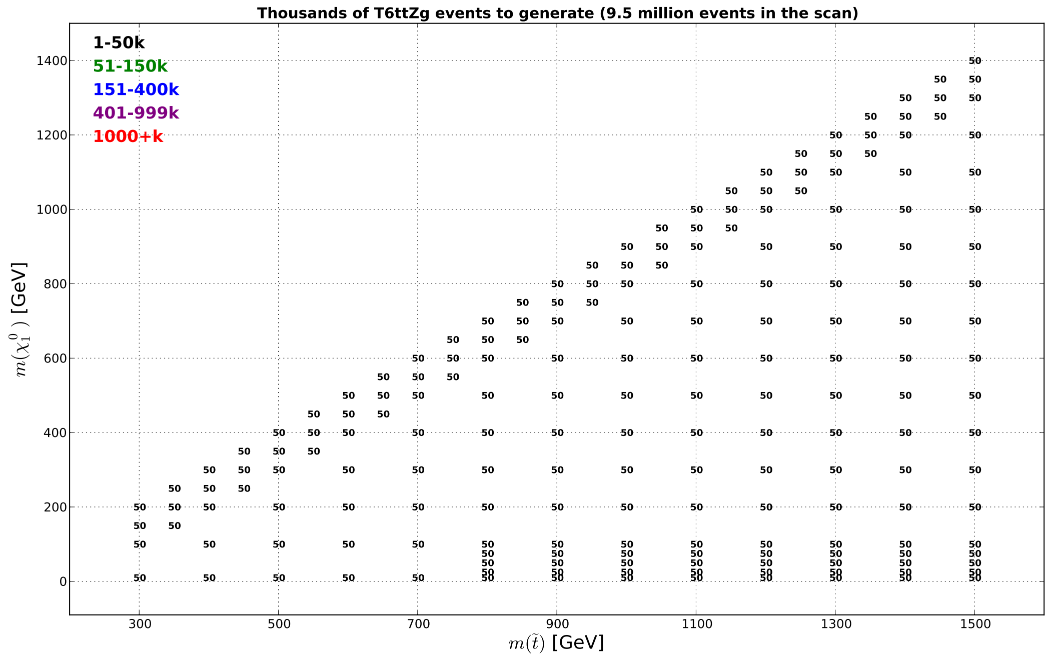

Figure 6.3: SUSY signal: T6ttZG scanned masspoints.

6.2.3 Background Samples

To estimate the expected E_T^{miss} from Standard Model backgrounds, this analysis uses Monte Carlo (MC) simulated samples produced in the “Summer16” MC campaign and reprocessed in `CMSSW_8_0_X`. Table 6.2 lists the datasets. Their cross sections are taken from the Twiki page [47]. Twiki is the wiki and web application platform for team collaboration at CERN.

Sample	Dataset	σ (pb)
$t\bar{t}$+ jets	/TT_TuneCUETP8M2T4_13TeV-powheg-pythia8/*	831.76
$t\bar{t}+W$	/TTWJetsToLNu_TuneCUETP8M1_13TeV-amcatnloFXFX-madspin-pythia8/*	0.2043
	/TTWJetsToQQ_TuneCUETP8M1_13TeV-amcatnloFXFX-madspin-pythia8/*	0.4062
$t\bar{t}+Z$	/TTZToLLNuNu_M-10_TuneCUETP8M1_13TeV-amcatnlo-pythia8/*	0.2529
	/TTZToQQ_TuneCUETP8M1_13TeV-amcatnlo-pythia8/*	0.5297
W+ jets	/W3JetsToLNu_TuneCUETP8M1_13TeV-madgraphMLM-pythia8/*	1160
	/W4JetsToLNu_TuneCUETP8M1_13TeV-madgraphMLM-pythia8/*	600
$Drell-Yan$	/DYJetsToLL_M-50_TuneCUETP8M1_13TeV-amcatnloFXFX-pythia8/	6025.2
Single $t/\bar{t}$		
s-channel	/ST_s-channel_4f_leptonDecays_13TeV-amcatnlo-pythia8_TuneCUETP8M1/*	3.36
t-channel	/ST_t-channel_top_4f_inclusiveDecays_13TeV-powhegV2-madspin-pythia8_TuneCUETP8M1/*	136.02
	/ST_t-channel_antitop_4f_inclusiveDecays_13TeV-powhegV2-madspin-pythia8_TuneCUETP8M1/*	80.95
tW	/ST_tW_antitop_5f_inclusiveDecays_13TeV-powheg-pythia8_TuneCUETP8M2T4/*	35.85
	/ST_tW_top_5f_inclusiveDecays_13TeV-powheg-pythia8_TuneCUETP8M2T4/*	35.85
WW	/WW_TuneCUETP8M1_13TeV-pythia8/*	110.8
WZ	/WZ_TuneCUETP8M1_13TeV-pythia8/*	47.13
ZZ	/ZZ_TuneCUETP8M1_13TeV-pythia8/*	16.52
$Z\gamma$	/ZGTo2LG_TuneCUETP8M1_13TeV-amcatnloFXFX-pythia8/*	117.86
$W\gamma$	/WGToLNuG_TuneCUETP8M1_13TeV-madgraphMLM-pythia8/*	405.27
$t\bar{t}+\gamma$	/TTGJets_TuneCUETP8M1_13TeV-amcatnloFXFX-madspin-pythia8/*	3.697
* = RunIISummer16MiniAODv2-PUMoriond17_80X_mcRun2_asymptotic_2016_TrancheIV_v6*/MINIAODSIM		
$T6ttZg$	/SMS-T6ttZg_TuneCUETP8M1_13TeV-madgraphMLM-pythia8/RunIISpring16MiniAODv2-PUSpring16Fast_80X_mcRun2_asymptotic_2016_miniAODv2_v0-v1/MINIAODSIM	Various

Table 6.2: List of background & signal MC datasets and cross sections used for normalization.

6.2.4 MC Pileup Reweighting

Due to the high instantaneous luminosity of LHC and the dead-time of hardware on detector, a single bunch crossing could contain several separate events as well as debris from previous brunching crossings, resulting in "Pileup". Pileup downgrades the resolution and reconstruction quality of data analysis. When simulating the background events and signal events, it is necessary and important to reweight the events in simulation to match the observed pileup distribution in data.

This reweighting is calculated as the ratio of true data pileup profile and MC pileup profile as shown in Figure 6.4. The true data pileup profile is calculated based on the 2016 full dataset using the total inelastic cross-section of 69.2 mb $\pm$ 4.6%, and the measured instantaneous luminosity of each bunch crossing. To produce the MC samples, the pileup parameters which are estimated according to the true pileup of previous collected data are set in the configuration file for simulation. Thus, the distribution of MC pileup can be obtained directly from CMSSW. The reweighting procedure makes the true pileup distribution of MC samples identical to observed data. This improves the agreement between data and MC.

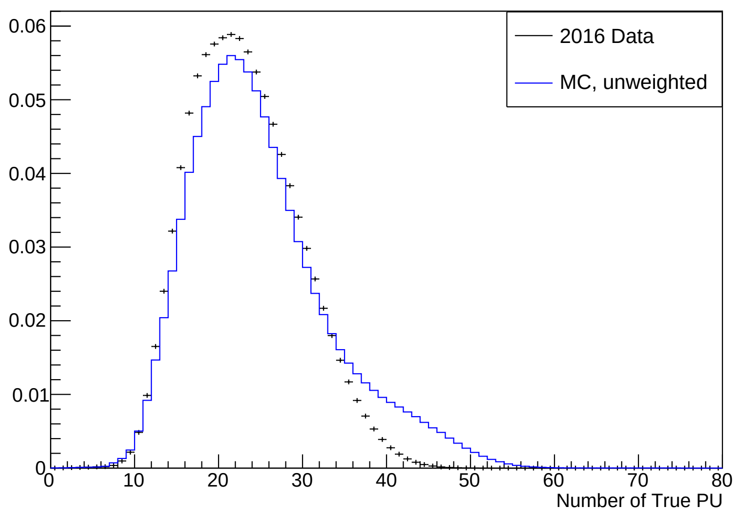

Figure 6.4: Comparison of the number of true pileup for data(black) and simulated background MC pieup before reweighting(blue).

6.2.5 Top P_T Reweighting

It has been generally observed that the leptons and jets produced by top quark decays exhibit a softer P_T spectrum than predicted by Monte Carlo simulations. Investigations by the CMS Top group found this was caused by a mis-modeling of the top quark P_T distribution. It was found that the differential cross-section for top quark pair production, as a function of top quark P_T , is softer than that of existing $t\bar{t}$ Monte Carlo samples.

Therefore, for simulated $t\bar{t}$ backgrounds, we need to apply a correction factor (SF) respect to P_T of generated top/antitop as recommended by the top group [48]. Event weight(w) is the square root of the production of SF_{top} and $SF_{anti-top}$:

$$SF(P_T) = e^{0.0615-0.0005\cdot P_T} \tag{6.1}$$

$$w = \sqrt{SF_{top} \cdot SF_{anti-top}} \tag{6.2}$$

A systematic uncertainty for this reweighting is determined by the difference between results obtained by reweighting $t\bar{t}$ samples twice (i.e. by the weights squared) and by no reweighting at all.

6.3 Objects Definition

In this section, we describe the selection of individual objects, namely muon, electron, photon and faked photon, jet and btagged jet. Leptons are defined in two categories, tight and loose.

6.3.1 Muon

Muons are selected in tight and loose categories based on the standard cut-based selection as described in Table 6.3.

The ID cuts for tight muon and loose muon includes all the specific cuts described in the Table 6.3. The definition of cut variables in the table are:

- P_T - the transverse momentum of the reconstructed muon.

Cuts	Tight μ	Loose μ
p_T	> 30 GeV/c	> 10 GeV/c
PFRelIso (0.4)	< 0.15	< 0.25
$\|\eta\|$	< 2.1	< 2.5
ID	POG Tight	POG Loose
	Global Muon	Global Muon or Tracker Muon
χ^2/NDOF of track fit	< 10	
$N_{hits}(muon\ chamber)$	> 0	
$N_{hits}(pixel)$	> 0	
$N_{layers}(tracker)$	> 5	
$N_{matched}(muonstation)$	> 1	
$\|d_{xy}(PV)\|$	$< 2mm$	
$\|d_z(PV)\|$	$< 5mm$	

Table 6.3: Tight and loose muon definitions.

- PFRelIso (0.4) - ParticleFlow-based combined relative isolation. It is the algorithm of isolation calculated within the cone of radius $\Delta R = 0.4$. It defines the ratio of the noise energy deposits to the candidate muon energy.

- $|\eta|$ - the absolute value of the pseudorapidity of the reconstructed muon.

- Global Muon - the muons reconstructed by the Particle Flow algorithm, with a χ^2 fit to tracks from both the tracker and muon chambers.

- Tracker Muon - the muons reconstructed by the Particle Flow algorithm, with a χ^2 fit to tracks from the tracker only.

- χ^2/NDOF - the reduced chi-squared of the global muon track fit.

- $N_{hits}(muon\ chamber)$ - the number of hits in the muon chambers used in the muon track fit.

- $N_{hits}(pixel)$ - the number of pixel layers in the inner pixel detector with hits used in the muon track reconstruction.

- $N_{layers}(tracker)$ - the number of tracker layers with hits used in the muon reconstruction.

- $N_{matched}(muon\ station)$ - the number of reconstructed muon segments of the muon chambers.

- $|d_{xy}(PV)|$ - the transverse distance of the muon track with respect to the primary vertex.

- $|d_z(PV)|$ - the longitudinal distance of the muon track with respect to the primary vertex.

6.3.2 Electron

Electrons are separated into cut-based tight and loose categories as defined in Table 6.4. Some cuts are specified according to whether the object been reconstructed in the electromagnetic calorimeter barrel (EB) or endcap (EE).

Cuts	Tight e	Loose e
p_T	> 35 GeV/c	> 10 GeV/c
$\|\eta\|$	< 2.1	< 2.5
	$!(1.4442 < \|\eta\| < 1.566)$	$!(1.4442 < \|\eta\| < 1.566)$
ID	POG Cut-based Tight	POG Cut-based Loose
PFRelIso(0.3)	< 0.0588(EB), < 0.0571(EE)	< 0.0994(EB), < 0.107(EE)
full5x5_sigmaIetaIeta	< 0.00998(EB), < 0.0292(EE)	< 0.011(EB), < 0.0314(EE)
abs(dEtaInSeed)	< 0.00308(EB), < 0.00605(EE)	< 0.00477(EB), < 0.00868(EE)
abs(dPhiIn)	< 0.0816(EB), < 0.0394(EE)	< 0.222(EB), < 0.213(EE)
H/E	< 0.0414(EB), < 0.0641(EE)	< 0.298(EB), < 0.101(EE)
abs(1/E-1/p)	< 0.0129(EB), < 0.0129(EE)	< 0.241(EB), < 0.14(EE)
expected missing inner hits	$<= 1$	$<= 1$
pass conversion veto	yes	yes

Table 6.4: Tight and loose electron defintions.

The ID cuts for tight electron and loose electron includes the the specific cuts described in Table 6.4. The definition of cut variables are:

- full5x5_sigmaIetaIeta - the shower shape variable which is summed over the 5×5 crystal matrix centered on the seed crystal.
- abs(dEtaInSeed) - the difference in η between the supercluster and the matched track.
- abs(dPhiIn) - the difference in ϕ between the supercluster and the matched track.
- H/E - the ratio of the hadronic energy in a cone of radius 0.15 centered on the electrons position, over the electromagnetic energy of the electrons supercluster.
- abs(1/E-1/p)- the difference between the inverse electromagnetic energy and the inverse tracker momentum.

- expected missing inner hits - number of missing hits in the inner tracker in reconstructed track fit.

- pass conversion veto - the electron must not be reconstructed from a photon which converts to an electron-positron pair within the tracker.

6.3.3 Photon

Photons are selected by applying the loose cut-based approach with an efficiency of about 90%. Only barrel ($|\eta|$ <1.4442) photons with a minimum transverse momentum of 20 GeV are considered. The selection criteria are given in Table 6.5. Photons are also required to be distinct from other selected objects in the event to suppress final state radiation (FSR) photons radiating from high-P_T leptons or final state partons. This requirement is:

- $\Delta R(\gamma, e/\mu) > 0.3$

- $\Delta R(\gamma, \gamma_{other}) > 0.3$

Cuts	Loose γ
E_T	> 20 GeV
$\lvert\eta\rvert$	< 1.4442
ID	passPixelVeto
ID	POG cut-based Loose
H/E	0.0597
$\sigma_{i\eta i\eta}$	0.01031
PF Charged Hadron Isolation	1.295
PF Neutral Hadron Isolation	$10.910 + 0.0148\gamma_{P_T} + 0.000017\gamma_{P_T}^2$
PF Photon Isolation	$3.630 + 0.0047\gamma_{P_T}$

Table 6.5: Photon definition.

The cut-based ID for loose photon includes all the specific cuts listed following. The definition of each cut is:

- E_T - the transverse energy of the reconstructed photon.

- passPixelVeto - No pixel seed in the pixel tracker.

- $\sigma_{i\eta i\eta}$ - the shower shape variable which is summed over the 5×5 crystal matrix centered on the seed crystal.

- PF Charged Hadron Isolation - Particle Flow isolation within a cone size of radius 0.3 for charged hadrons associated to the primary vertex.

- PF Neutral Hadron Isolation - Particle Flow isolation within a cone size of radius 0.3 for neutral hadrons associated to the primary vertex.

- PF Photon Isolation - Particle Flow isolation within a cone size of radius 0.3 for photons associated to the primary vertex.

In addition to the candidate photon definition, "fake" photons are defined to provide control regions in which to compare the performance of the E_T^{miss} shape in MC to data. Fakes are defined similarly to candidate photons, but are required to fail either the $\sigma_{i\eta i\eta}$ or the charged hadron isolation (chHadIso) requirements. An upper limit of 20 GeV is placed on the charged hadron isolation sum to ensure that poorly isolated QCD multi-jet events with very dissimilar E_T^{miss} resolution are not included in any fake comparison. The fake photon definition is summarized in Table 6.6.

	γ	*fake*
Requirement	$\sigma_{i\eta i\eta} < 0.01031$ and chHadIso < 1.295	chHadIso < 20 and ($\sigma_{i\eta i\eta} \geq 0.01031$ or chHadIso ≥ 1.295)

Table 6.6: Fake photons are defined as failing either the $\sigma_{i\eta i\eta}$ or charge hadron isolation requirement of the candidate photon selection. An upper window of 20 GeV is required for the isolation to retain similarity between the two objects.

6.3.4 Jet

Jets are reconstructed within a cone size of 0.4. All jet candidates need to pass the following clean criteria to select isolated jets without overlapping with other objects:

- $\Delta R(jet, e/\mu/\gamma) > 0.4$

The loose working point Jet-Id selection is chosen. A selected jet is considered b-tagged if the algorithm discriminator variable is greater than 0.8484, which is the medium working point (CSVv2M) as described in section 5.5.1.

The cut-based ID for loose jet includes all the specific cuts listed following. The definition for each cut is:

Cuts	Jet
p_T	> 30 GeV/c
$\|\eta\|$	< 2.4
ID	Jet PFLooseID
CEF/NHF/NEF	< 0.99
CHF/NCH	> 0
$N_{constituents}$	> 1

Table 6.7: Jet definition.

- CEF/NHF/NEF/CHF - the charged electromagnetic, neutral hadronic, neutral electro-magnetic, and charged hadronic energy fractions to the total energy of the jet candidate.

- NCH - the multiplicity of charged hadrons of the jet candidate.

- $N_{constituents}$ - the number of all Particle Flow particles in the jet candidate.

6.3.5 Efficiency, Scale Factor and Weight

To select the physics objects we are interested in, some carefully studied cuts are applied and efficiencies are introduced into this procedure, including reconstruction efficiency, identification efficiency, isolation efficiency, etc.

In a sample A with total number of N_A events, after requiring certain cut criteria S, the number of N_S events are selected, the efficiency ϵ is the probability that one event in the sample passes the selection.

$$\epsilon_S(A; x) = P(S|A; x) \tag{6.3}$$

where x is the optional reference quantity. In a large enough sample, efficiency can be simply measured as $\epsilon_S = N_S/N_A$.

The difference between the efficiency of a selection requirement in data and MC is commonly observed. To correct this difference, the scale factor is applied to the simulated events,

$$SF = \frac{\epsilon_{data}}{\epsilon_{MC}} \tag{6.4}$$

For the objects/events with multiple selection requirements, the total scale factor is the production of each scale factor and written as,

$$SF = \prod_i SF_i \tag{6.5}$$

The errors of these scale factors are uncorrelated, the total relative error can be calculated as,

$$\frac{\sigma_{SF}}{SF} = \sqrt{\sum_i (\frac{\sigma_{SF_i}}{SF_i})^2} \tag{6.6}$$

The object selections in this analysis use the recommended criteria from the CMS analysis and object groups, the efficiencies are well-measured and can be applied in analysis without re-measuring.

Electron

Electron scale factor combines the reconstruction scale factor and identification scale factor. Figure 6.5 shows this combined electron scale factor by using the result from EGM POG [49].

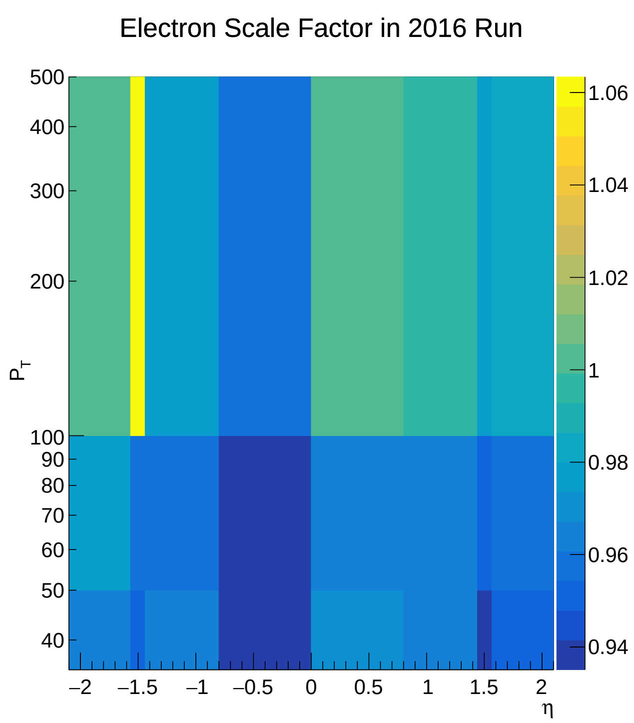

Figure 6.5: Electron scale factor as a function of P_T and η.

Muon

Muon scale factor combines the tracking scale factor, identification scale factor and isolation scale factor. Figure 6.6 shows the combined muon scale factor by using the result from Muon POG [14].

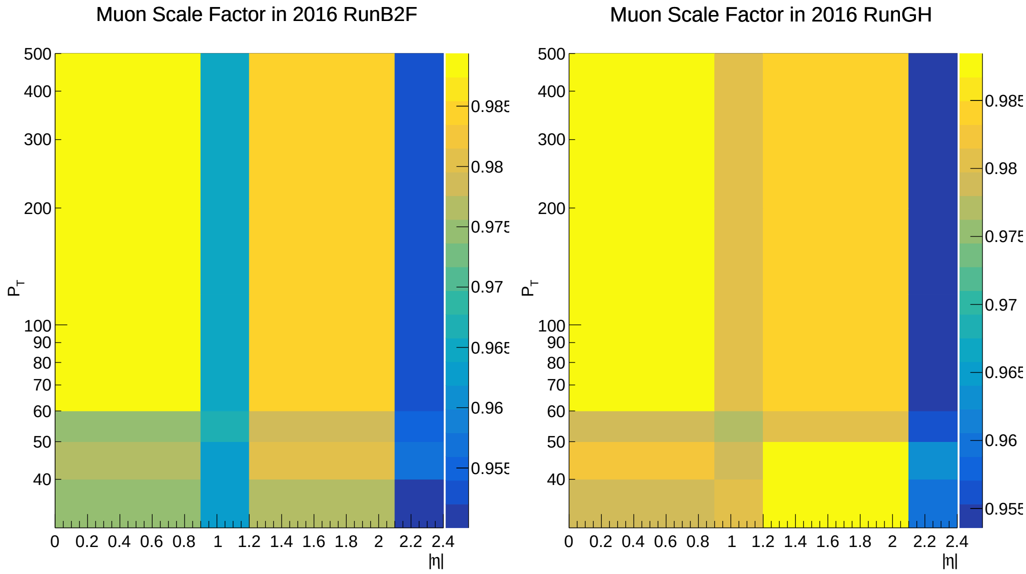

Figure 6.6: Muon scale factor as a function of P_T and $|\eta|$ for 2016 Run period B-F (left) and GH (right).

Photon

Photon scale factor combines the identification scale factor and pixel veto scale factor. Figure 6.7 shows the combined photon scale factor by using the result from EGM POG [50].

B-tagging Weight

B-tagging scale factors are measured on a jet-by-jet basis. In this analysis, we select multiple jets with at least one b-tagged jet. Rather than applying the object based scale factor, the b-tagging weight of the selected events due to the multiple btagging efficiencies and mis-tagging rate must be corrected. We use the method of reference [51] that only reweights the selected simulated events by scale factors and MC b-tagging efficiencies to predict the correct event yield in observed data. In this way, we avoid re-adding the un-selected events without b-tags and the migration of

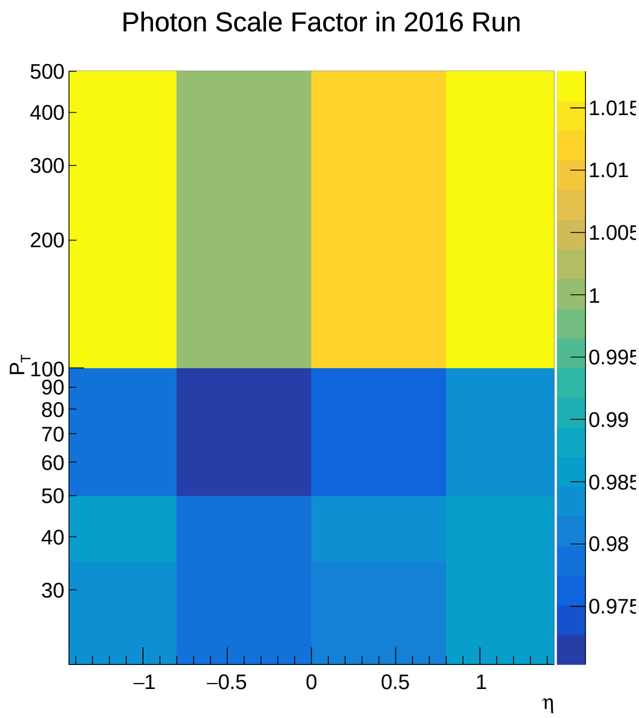

Figure 6.7: Photon scale factor as a function of P_T and η.

b-tag multiplicity of events.

For a given configuration of jets, the probabilities of simulated MC and data are defined as:

$$P(MC) = \prod_{i=tagged} \epsilon_i^{MC} \prod_{j=un-tagged} (1 - \epsilon_j^{MC}) \tag{6.7}$$

$$\tag{6.8}$$

$$P(Data) = \prod_{i=tagged} \epsilon_i^{Data} \prod_{j=un-tagged} (1 - \epsilon_j^{Data}) \tag{6.9}$$

$$= \prod_{i=tagged} SF_i \epsilon_i^{MC} \prod_{j=un-tagged} (1 - SF_j \epsilon_j^{MC}) \tag{6.10}$$

where the ϵ_i^{MC} is the b-tagging efficiency of MC and the SF_i is the b-tagging scale factor between Data and MC. The ϵ_i^{MC} and SF_i are functions of the jet flavor (b-bottom flavor, c-charm flavor, l-light flavor(u,d,s)), jet P_T and jet η.

The event weight is calculated as,

$$w = \frac{P(Data)}{P(MC)} \tag{6.11}$$

For each selected MC event, the btagging weight is calculated based on its jets configuration and applied. This reweighting process corrects the difference between data and MC due to the b-tagging selection.

6.4 Event Selection

6.4.1 Event Cleaning

We require each event to pass selections designed to remove non-physical and non-collision events such as instrumental noise and beam backgrounds.

Events are required to have at least one good primary vertex (PV) that passes the following requirements:

- There are at least 5 degrees of freedom in the vertex fitting procedure when fit the vertex from tracks with beam constraint
- $|z|$, the deviation along the beamline from the nominal center of the detector is less than 24 cm
- $|\rho|$, the transverse deviation in x-y plan from the beamline is less than 2 cm

Events are also required passing the following recommended E_T^{miss} filters [52]:

- Flag_HBHENoiseFilter
- Flag_HBHENoiseIsoFilter
- Flag_EcalDeadCellTriggerPrimitiveFilter
- Flag_goodVertices
- Flag_eeBadScFilter
- Flag_globalTightHalo2016Filter
- Flag_BadPFMuonFilter
- Flag_BadChargedCandidateFilter
- Flag_noBadMuons (reMiniAOD data samples, corresponds to not Flag_badMuons&Flag_duplicateMuons)

6.4.2 Trigger

Candidate events must pass the corresponding High-Level triggers (HLT) listed in Table 6.8. Electron+jets events must pass the SingleEle trigger, and muon+jets events must pass the SingleMu trigger. To estimate the QCD background, we select anti-isolated muon events using the HLTs as listed in Table 6.9. No HLT requirement for anti-isolated (particle candidates that fail the isolation requirement in reconstruction) electron events since tight isolation cuts are implemented in HLT, that conflicts with the QCD anti-isolation cut.

Dataset	Trigger name
SingleEle	HLT_Ele32_eta2p1_WPTight_Gsf
SingleMu	HLT_IsoMu24_v* || HLT_IsoTkMu24_v*

Table 6.8: List of triggers used to collect signal candidates.

Dataset	Trigger name
SingleMu(QCD)	HLT_IsoMu24_v* || HLT_IsoTkMu24_v*

Table 6.9: List of triggers used to collect QCD candidates in muon+jet data.

Tag-and-Probe Method for Trigger Efficiency

The efficiencies of the triggers must be corrected for Monte Carlo events by applying a scale factor $SF = \epsilon_{data}/\epsilon_{MC}$ to match the efficiencies in observed data. Since this analysis uses the recommendations from the POGs, most efficiencies are available from the POGs. No Single Electron HLT efficiency is provided by EGM POG officially, so these efficiencies are measured by using the Tag-and-Probe package [13] recommended by EGamma POG, the example plots showing Tag-and-Probe fitting quality in Figure 6.8.

The Tag-and-Probe method is based on the $Z \to ee$ process. The procedure can be summarized as follows:

- Select all ee events with a electron pass the Tag requirement.
- In all tagged events, testing the other electron whether it passes or fails the Probe requirement, here the probe criteria is the HLT filters.

- The passing probe and failing probe pairs are fitted on invariant-mass spectra by a Crystal Ball function with the backgrounds subtracted. The $N_{passing}$ is the number of events passing probe after fitting, $N_{failing}$ is the number of events failing probe after fitting.

- The ratio between the $N_{passing}$ and $N_{passing}+N_{failing}$ is taken as the efficiency of this probe.

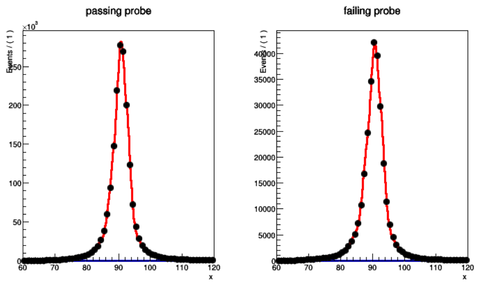

(a) data: bin $\eta(0, 0.8)P_T(35, 50)$

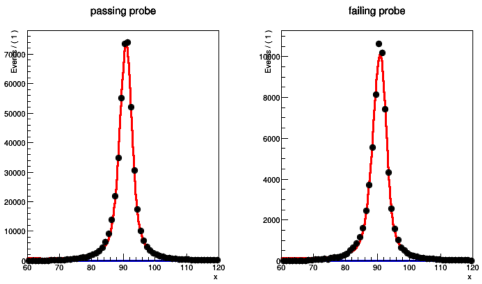

(b) mc: bin $\eta(0, 0.8)P_T(35, 50)$

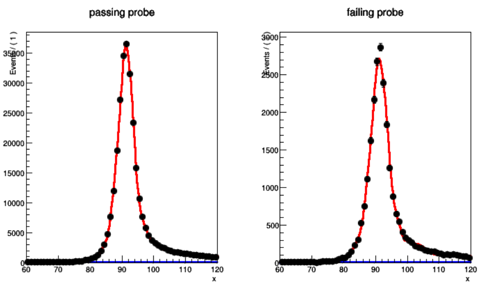

(c) data: bin $\eta(-1.44, -0.8)P_T(50, 100)$

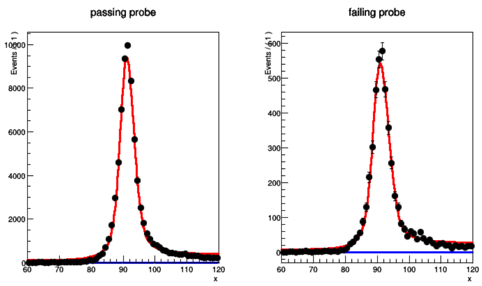

(d) mc: bin $\eta(-1.44, -0.8)P_T(50, 100)$

Figure 6.8: Example plots in tag and probe fitting process for measuring Single Electron HLT efficiencies. X axis represents the invariant mass of two selected electrons. For detailed procedures, refer to reference [13].

Figure 6.9 shows the electron trigger efficiency and scale factor, Figure 6.10 shows the muon trigger efficiencies and scale factors.

6.4.3 Preselection

This preselection requires that each event:

- Passes event cleaning and trigger requirements

- Has exactly one tight, isolated lepton (e, μ)

- Has no additional loose leptons

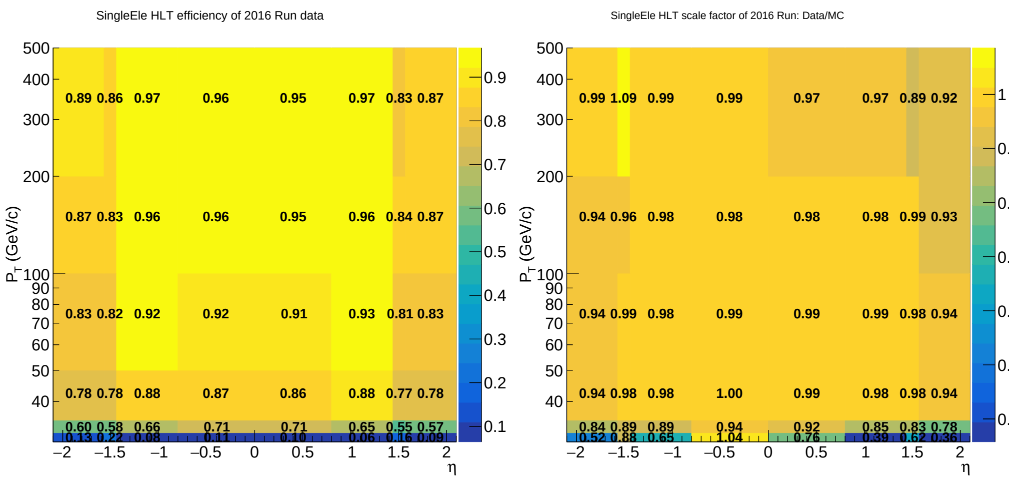

Figure 6.9: Single Electron HLT(`HLT_Ele32_eta2p1_WPTight_Gsf`) efficiency of 2016 data(left) and the corresponding scale factor(right) binned in η and P_T. The efficiency value of each bin is marked.

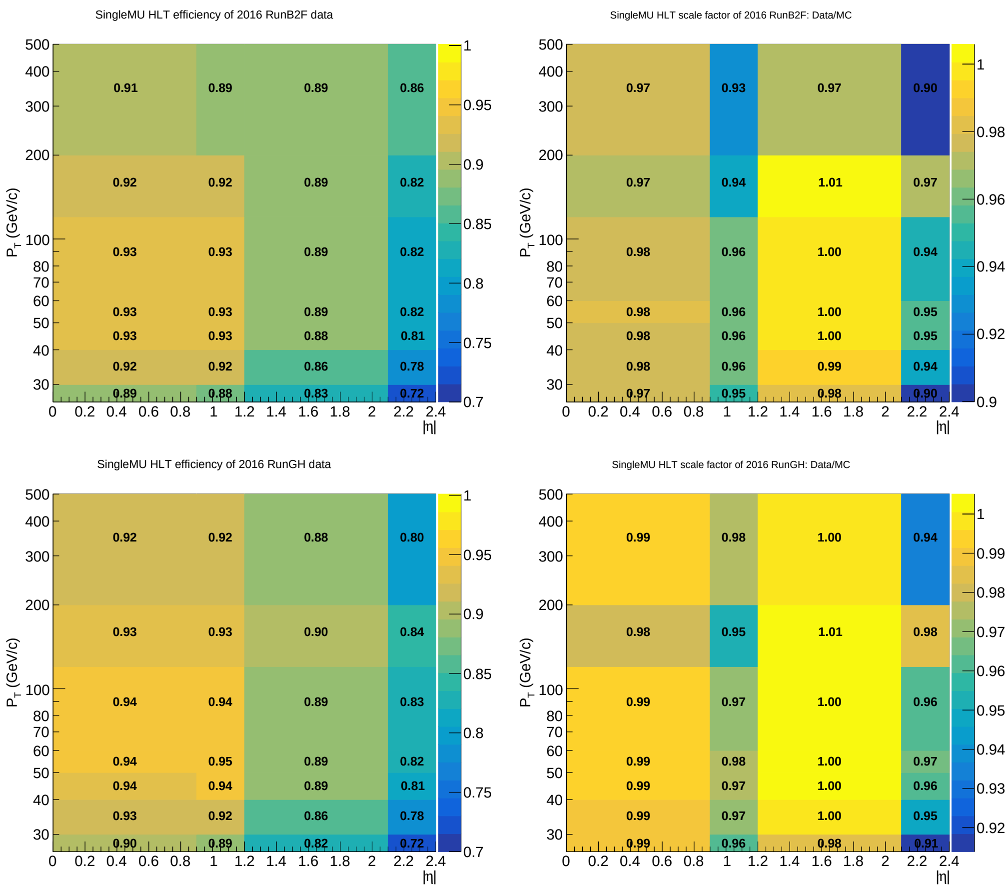

Figure 6.10: Single Muon HLT(`HLT_IsoMu24_v*` || `HLT_IsoTkMu24_v*`) efficiencies of 2016 data(left) and the corresponding scale factors(right) binned in $|\eta|$ and P_T and split into two ranges: RunBCDEF(top) and RunGH(bottom), corresponding to the periods with different trigger configurations. These results are obtained from MuonPOG [14]. The efficiency value of each bin is marked.

- Has at least 3 jets
- At least one selected jet is b-tagged by CSVv2M.

6.4.4 Signal Region and Control Region Selection

For the events that past the preselection, distinct signal and control regions are defined based on the number of selected photons and fake photons in addition to the above criteria. These are defined as:

Signal Region 1 (SR1): $N_\gamma = 1$.

Signal Region 2 (SR2): $N_\gamma \geq 2$.

Control Region 1 (CR1): $N_\gamma = 0$, $N_f = 1$.

Control Region 2 (CR2): $N_\gamma = 0$, $N_f \geq 2$.

Figure 6.11 shows the sketch of the control and signal regions. The control regions veto the presence of selected photons to avoid overlap with signal regions.

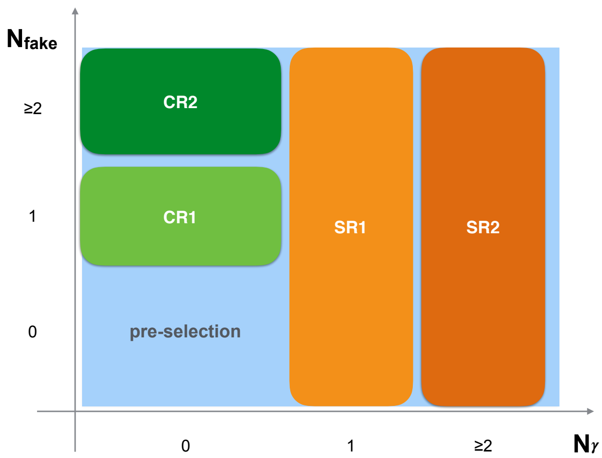

Figure 6.11: Sketch of the signal and control region definitions

6.4.5 Data-driven QCD Event Selection

QCD multi-jet and γ+jet backgrounds are negligibly small in the signal regions, but not in the control regions and the preselected regions. To collect a sample of events from data with which to describe the E_T^{miss} distribution of QCD background, we employ "QCD" lepton definitions that are orthogonal to the signal lepton definitions where the isolation requirement of QCD lepton is inverted with respect to the signal lepton's loose definition. QCD lepton is actually lepton-like jet.

These definitions of tight QCD lepton are listed in Tables 6.10 and 6.11. Similar to the requirement of exactly one tight lepton in the signal preselection, we require exactly one QCD lepton and zero additional loose leptons to select QCD events from the data.

Cuts	eQCD
p_T	> 30 GeV/c
$\|\eta\|$	< 2.1 $!(1.4442 < \|\eta\| < 1.566)$
ID	POG Cut-based Tight(no iso)
PFIso	0.0994<relIso<1.(EB) 0.107<relIso<1.(EE)

Table 6.10: QCD electron (eQCD) definition.

Cuts	μQCD
p_T	> 30 GeV/c
PFRelIso (0.4)	> 0.25
$\|\eta\|$	< 2.1
ID	POG Tight

Table 6.11: QCD muon (μQCD) definition.

6.5 Estimation of MET Background

All backgrounds are taken from their simulations of MC samples, except for the small data-driven QCD contribution to CR1. After applying the event selection to each MC sample, they are normalized to the total integrated luminosity of data using the cross sections listed in table 6.2. The MC samples have been reweighted with scale factors to correct for differences between MC and data in pileup, b-tagging efficiencies, lepton efficiencies, and photon efficiencies.

Several background scale factors are derived to correct for some mis-modelings. Section 6.5.3 addresses the W+jets and $t\bar{t}$ normalizations, Section 6.5.4 addresses the misidentification rate of electrons as photons, and Section 6.5.5 addresses the effect of simulated photon purity on the E_T^{miss} distribution shape. The Template Fit method, which is applied to derive these scale factors, is introduced in Section 6.5.1.

6.5.1 Template Fit Procedure

To estimate the composition of an observed data sample from the sources of various MC simulated backgrounds, the template fit procedure [53] is widely used in this analysis. The fit is performed using a binned maximum likelihood fit while taking into account the statistics. For the spectrum of a variable, the distribution of expected data d_{data}, is to fit as the sum of each normalized MC source d^i_{MC}, written as,

$$d_{data} = \sum_i f_i \cdot d^i_{MC} \tag{6.12}$$

where f_i is the scale factor for MC source i. The fit is optimized by maximizing the binned likelihood:

$$Log\,\mathcal{L} = \sum_{j\in bins} d^j_{data} \cdot (Log \sum_{i\in MCs} f_i \cdot d^{ij}_{MC}),\ \ 0 < f_i < 1 \tag{6.13}$$

where d^{ij}_{MC} is the number of MC events from source i in bin j, d^j_{data} is the number of data in bin j.

To account for the statistical fluctuations, we use the D^{ij}_{MC} as the expected number of events from MC source i in bin j,

$$d^{j}_{data} = \sum_{i} f_i \cdot D^{ij}_{MC} \tag{6.14}$$

Thus, the d^{ij}_{MC} is the corresponding generated distribution of D^{ij}_{MC}, and the fit is optimized by maximizing the combined binned likelihood which is written as,

$$Log\,\mathcal{L} = \sum_{j\in bins} d^{j}_{data} \cdot (Log \sum_{i\in MCs} f_i \cdot d^{ij}_{MC}) + \sum_{j\in bins}\sum_{i\in MCs} d^{ij}_{MC} \cdot Log D^{ij}_{MC}, \quad 0 < f_i < 1 \tag{6.15}$$

This fitting procedure is realized by deploying the TFractionFitter class [54] in ROOT. The systematic uncertainties of scale factors derived from template fit are calculated by fluctuating the templates for each systematic uncertainty and performing the fitting procedure to get the corresponding scale factors, and adding the fluctuations in quadrature.

6.5.2 QCD Background

While negligible in all signal regions, QCD multi-jet and γ+jet events still are a small contribution to CR1.

The E_T^{miss} distribution of the QCD background is taken from data using the QCD selection outlined in Section 6.4.5 and separated into the categories of photon and fake multiplicity listed in Section 6.4.3. No kinematic reweighting is applied to the shape due to the lack of QCD contribution in the signal region. The expected E_T^{miss} distribution shapes for QCD background in pre-selected regions are shown in Figure 6.12.

To constrain the overall rate and lepton fake rate for QCD events surviving our selection, an overall normalization is performed to the QCD background. In the region of $E_T^{miss} \leq 20$ GeV the QCD background event number is scaled to make up the difference between the observed data and the total MC simulated backgrounds. This normalization scale factor is 0.39 ± 0.01 (stat.) for the electron channel and 0.37 ± 0.01 (stat.) for the muon channel. The scale factors will be applied to the expected QCD shapes in Figure 6.12 and contribute to the total background.

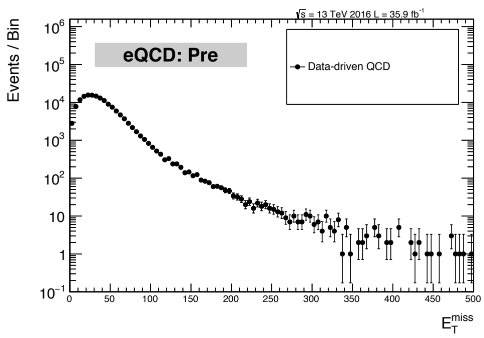

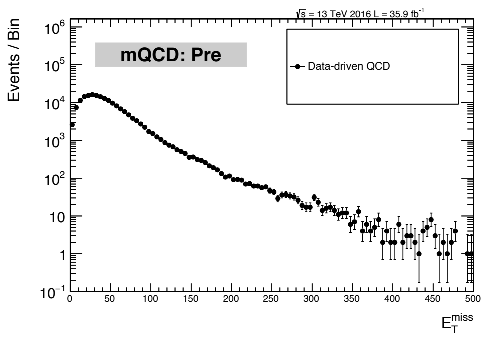

Figure 6.12: The expected E_T^{miss} distribution shapes of QCD background in electron (left) and muon (right) channels before normalization.

6.5.3 W+jets and $t\bar{t}$ Cross Section

The cross section for $W+$ jets production is observed to be poorly simulated when requiring b-tagged jets, as well as from the usage of only $W + 3$ jets and $W + 4$ jets samples. Besides, $t\bar{t}$ productions can be over-estimated since it overlaps with $t\bar{t}\gamma$ and ttV productions. Since we do not do a full kinematic reconstruction of the top quarks in $t\bar{t}$ events, we use the "M3" variable to discriminate $W+$ jets from the dominant $t\bar{t}$ background. The M3 variable is defined as the invariant mass of the three-jet system in each event having the highest transverse momentum of all three-jet combinations. Hadronic decays of boosted top quarks will produce a three-jet system with large P_T and having a mass near the top quark mass, $\sim 175\ GeV/c^2$; other processes without a heavy decay to three jets show a much smoother invariant mass distribution. By using a template fit for M3, the scale factors for both $W+$ jets and $t\bar{t}$ are derived and applied to the signal regions.

The template fit is performed in the M3 variable in the pre-selection for all events regardless of photon multiplicity. The signal template is taken from $t\bar{t}jets$ MC, and the background template is taken from $W+$ jets MC. All other backgrounds are subtracted from the data as shown in Figure 6.13 before the fitting procedure, the adjusted data for fitting is around 85% of the original total observed event number. The results of the fit are shown in Table 6.12 and Figure 6.14.

Channel	SF_W	$SF_{t\bar{t}}$
e	1.72 $\pm$ 0.03 (fit+stat.) $\pm$ 0.29 (syst.)	0.818 $\pm$ 0.003 (fit+stat.) $\pm$ 0.071 (syst.)
μ	1.60 $\pm$ 0.02 (fit+stat.) $\pm$ 0.29 (syst.)	0.854 $\pm$ 0.003 (fit+stat.) $\pm$ 0.067 (syst.)

Table 6.12: Scale factors (k-factors) for the normalization of $W+$ jets and $t\bar{t}$.

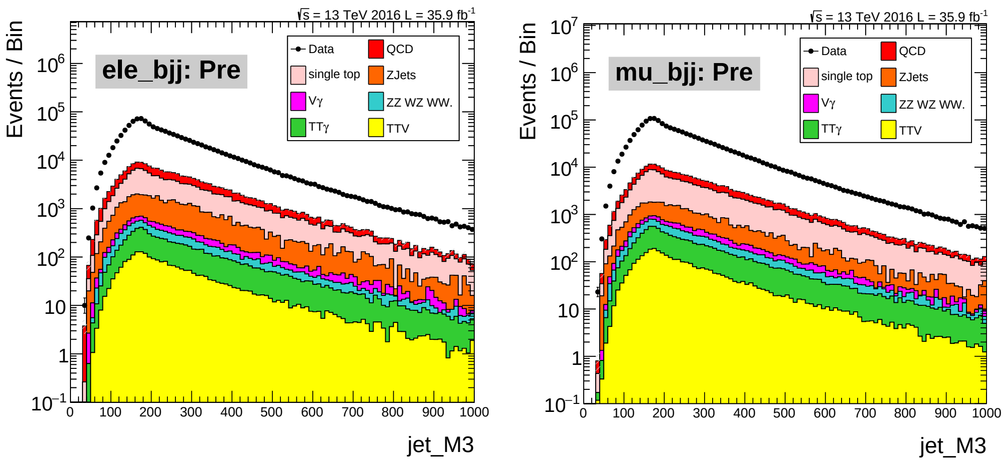

Figure 6.13: Subtraction of all the other backgrounds listed in the legend for electron(left) and muon(right) channels, the difference between the observed data (back dots) and the stacked histogram of all the other backgrounds except $t\bar{t}$ and $W+$ jets is taken as the adjusted data for the template fit.

6.5.4 Electron Misidentification Rate

The electron channel has a significant difference from the muon channel due to the non-negligible rate of electrons misidentified as photons. $Z \rightarrow ee$ events with an electron misidentified as a photon can be observed as a peak in the invariant mass of reconstructed $e\gamma$ pairs in SR1 near 90 GeV/c^2. Other backgrounds in SR1 do not exhibit a peak in this distribution. The misidentification of electrons as photons is most visible in the peak near 90 GeV/c^2in the invariant mass of $e\gamma$ pairs in SR1 which requires one photon. The simulated sample of this rate is seen to be smaller than in data in Figure 6.15.

Considering all of this, a truth-matching procedure in simulated $Z+$ jets backgrounds is applied to find events with an electron misidentified as a photon. For all reconstructed photons, the generator-level truth is determined by finding the matching generator particle requiring:

- $\Delta R(\gamma_{reco},\ \gamma_{gen}) < 0.01$ in the case of matching to a photon, or
- $\Delta R(\gamma_{reco},\ e_{gen}) < 0.04$ in the case of matching to an electron
- $|\Delta\eta(\gamma_{reco},\ e(\gamma)_{gen})| < 0.005$
- $|\mathrm{P}_T{}^{reco} - \mathrm{P}_T{}^{gen}|\ /\ \mathrm{P}_T{}^{gen} < 0.1$

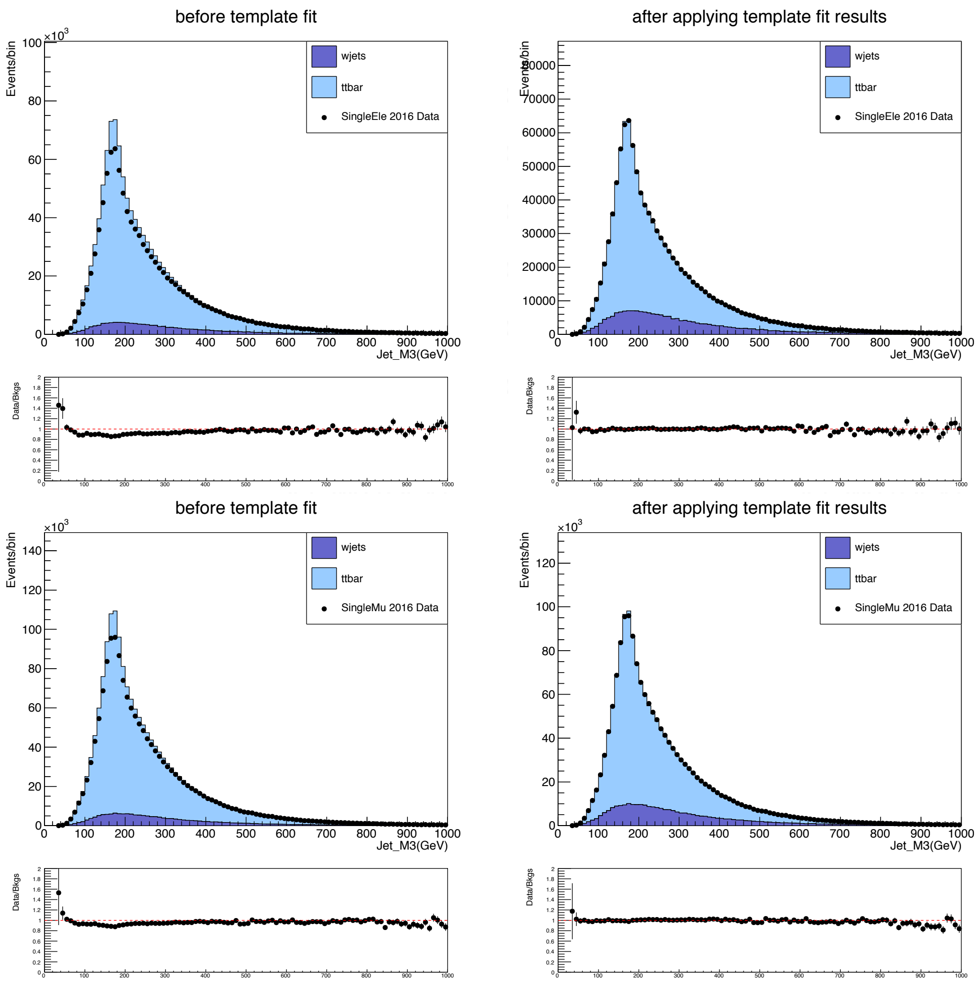

Figure 6.14: Before(left) and after(right) template fit results for the $W+$ jets and $t\bar{t}$ normalization in M3 for the electron channel(top) and muon channel(bottom). Here the black dots represent the distribution of adjusted data sample by subtracting all the other backgrounds.

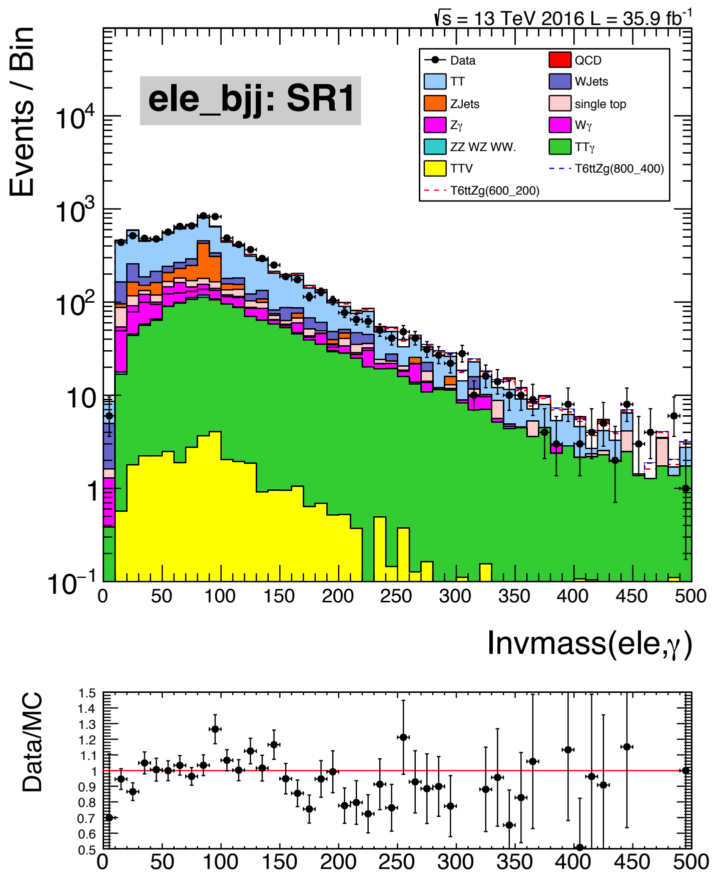

Figure 6.15: Comparison of the $m_{e\gamma}$ (left) in data and MC for the electron channel before correcting the electron fake photon rate. It is clear from the E_T^{miss} discrepancy that the simulation is deficient, and the $m_{e\gamma}$ discrepancy reveals this is caused by the $Z+$ jets background.

Reconstructed photons are categorized by whether they are matched to a generator-level photon or electron in this way, or if matched to neither one, the photon is considered as matched to a jet.

The electron misidentification rate scale factor is measured by a template fit of $m_{e\gamma}$ in SR1 while restrict the $m_{e\gamma}$ range in 70 - 120 GeV. The signal template is taken from $Z+$ jets sample where the photon is matched to a generated electron, and the background template is taken from $Z+$ jets sample where the photon is matched to a generated photon or jet. All the other backgrounds are subtracted from the observed data as shown in Figure 6.16 before the fitting procedure. The adjusted data is around 24% of the original total data number.

The results of this fit are shown in Figure 6.17 and give the scale factors of $Z+$ jets:

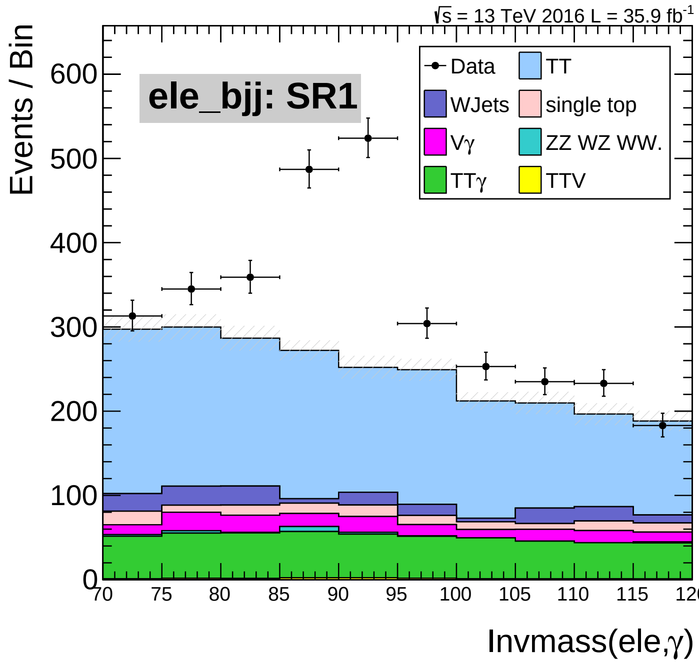

Figure 6.16: Subtraction of all the other backgrounds listed in the legend, the difference between the observed data and all the other backgrounds is taken as the adjusted data for the template fit.

$$SF_{real\gamma} = 1.09 \pm 0.02(\text{fit+stat.}) \pm 0.70(\text{syst.}) \tag{6.16}$$

$$SF_{efaked\gamma} = 1.90 \pm 0.01(\text{fit+stat.}) \pm 0.41(\text{syst.}) \tag{6.17}$$

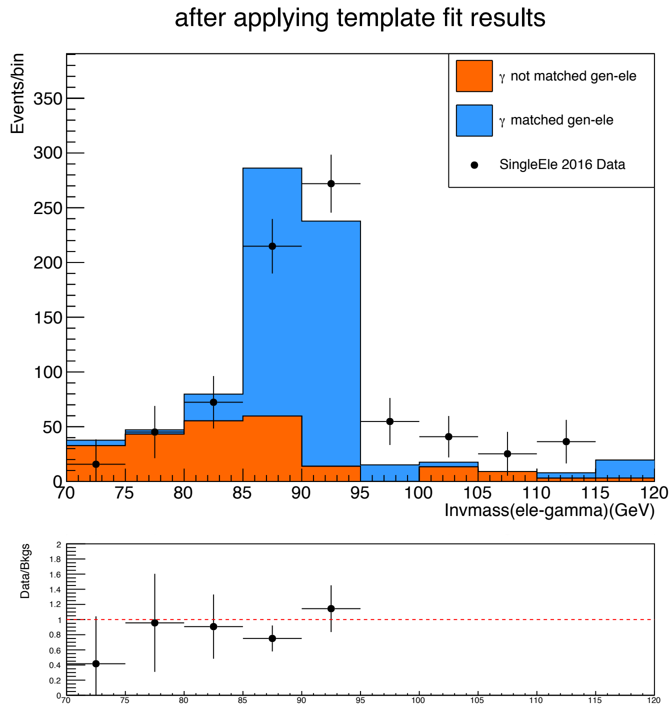

Figure 6.17: Template fit result for the electron to photon misidentification rate. Exactly one photon is required (SR1).

This scale factor pair should be applied to the $Z+$ jets sample in electron channel according to the matched generated particle of the selected photon. Considering E_T^{miss} is our search signature, we studied the effect on $Z+$ jets before and after applying the scale factors as shown in Figure 6.18. The further study indicates that in the uncertainty variation range, the scale factors don't change the E_T^{miss} shape, only change the normalization value. We then derive the unified scale factor for $Z+$ jets sample. To simplify the procedure, we apply this unified scale factors in our results.

The Z+jets scale factor in SR1 of electron channel is $SF_{Z+jets} = 1.4 \pm 0.2(\text{fit+stat.}) \pm 0.6(\text{syst.})$.

6.5.5 Photon Purity Adjustment for $t\bar{t}jets$ and $t\bar{t}\gamma$

We select loose cut-based photon due to the high efficiency ($\sim 90\%$), despite its low overall purity of real, prompt photons. The high E_T^{miss} backgrounds in each of the

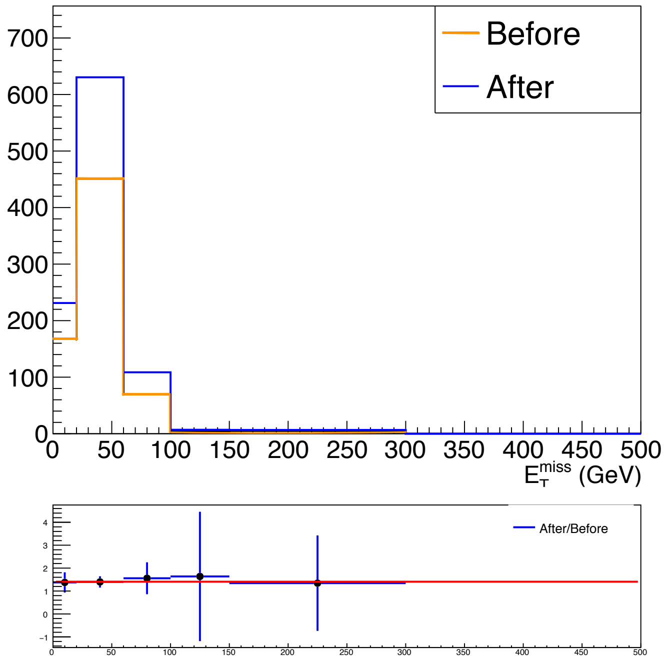

Figure 6.18: E_T^{miss} distributions of $Z+$ jets before and after applying the scale factors of electron faked photon template fit.

signal regions is then a rather impure mixture of $t\bar{t}\gamma$ and $t\bar{t}jets$ with many selected "photons" being misidentified jets. Furthermore, there is the lack of a dedicated $t\bar{t}\ \gamma\gamma$ sample of simulated events. As a search using the shape of E_T^{miss} distribution as the signature, the precise composition of the signal region samples is of no concern, only the accurate estimation of the E_T^{miss} distribution is necessary.

This section describes a measurement of the simulated photon purity and an adjustment to match the purity of the observed data. The effect of this purity adjustment on the E_T^{miss} distribution shape uses the strategy which is similar to that of the electron faked photon study 6.5.4.

The photon purity is measured by the template fit in variables that discriminate between prompt photons and jets. There are two discriminating variables, the charged hadron isolation (chHadIso) and $\sigma_{i\eta i\eta}$ of candidate photons.

The signal and background templates are formed for both chHadIso and $\sigma_{i\eta i\eta}$ in SR1 by removing the requirement on each variable and matching the reconstructed photon to its generator-level MC truth as outlined in Section 6.5.4. The signal template is taken from $t\bar{t}jets$ and $t\bar{t}\gamma$ MC where the photon is matched to either an electron or a photon, and the background template is taken from $t\bar{t}jets$ and $t\bar{t}\gamma$ where the photon is matched to a jet. All other backgrounds are subtracted from the observed data before fitting, the adjust data for fitting is around 70% of the original total data number. The results of each fit are shown in Figure 6.19, and listed in Tables 6.13.

Channel	γ Purity	
	prompt photon	non-prompt photon
e		
chHadIso	0.76 ± 0.10 (fit+stat.) ± 0.18 (syst.)	1.47 ± 0.21 (fit+stat.) ± 0.02 (syst.)
$\sigma_{i\eta i\eta}$	0.77 ± 0.05 (fit+stat.) ± 0.14 (syst.)	1.37 ± 0.06 (fit+stat.) ± 0.11 (syst.)
μ		
chHadIso	0.72 ± 0.08 (fit+stat.) ± 0.12 (syst.)	1.41 ± 0.16 (fit+stat.) ± 0.06 (syst.)
$\sigma_{i\eta i\eta}$	0.78 ± 0.04 (fit+stat.) ± 0.11 (syst.)	1.35 ± 0.04 (fit+stat.) ± 0.10 (syst.)

Table 6.13: Photon purity from simulation and fit to data. The template fit results of two photon variables chHadIso, $\sigma_{i\eta i\eta}$ agree. Also, the results in Electron channel agree with Muon channel, since the photon purity is independent of the type of selected lepton in events.

We use the similar strategy as the measurement for the Electron misidentification rate 6.5.4. We combine the scale factors of prompt photon and non-prompt

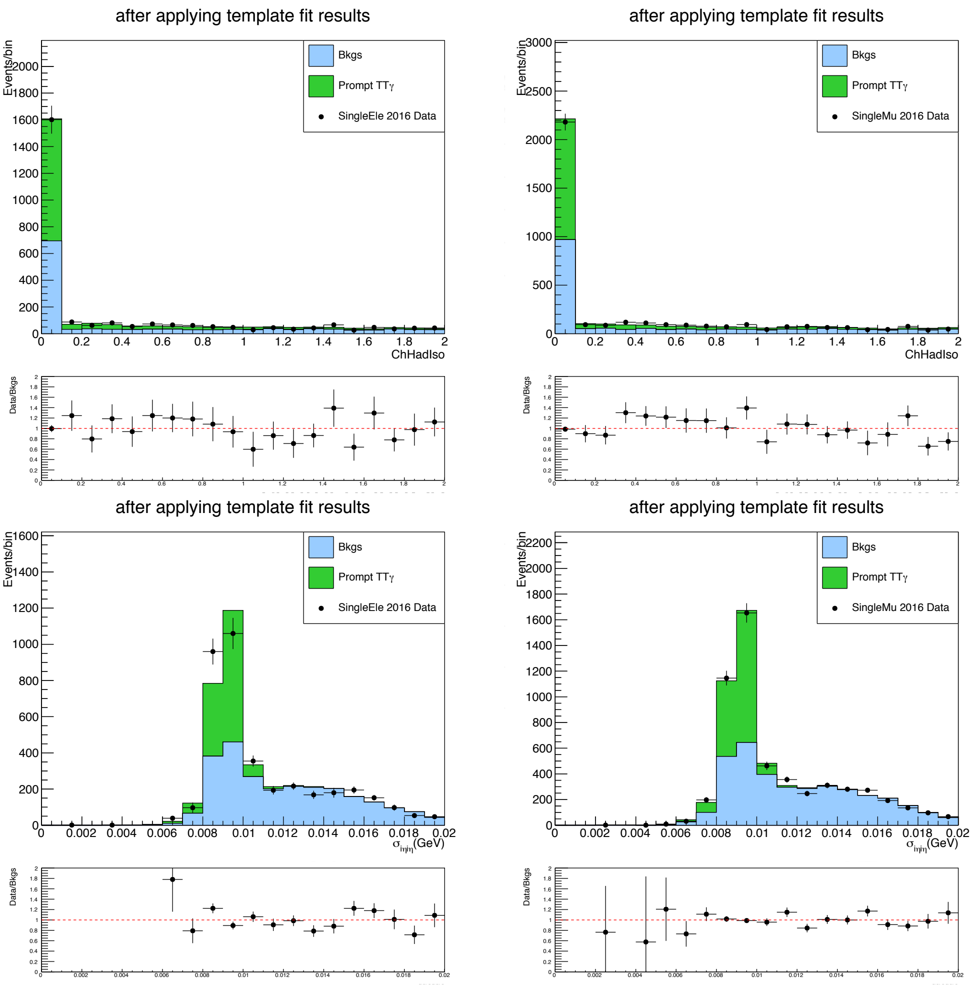

Figure 6.19: Template fit results for the electron (left) and muon (right) channels, in the photon variables charged hadron isolation (top) and $\sigma_{i\eta i\eta}$ (bottom).

photon to get a unified scale factors for $t\bar{t}jets$ and $t\bar{t}\gamma$ samples. Taking into account the uncertainties, scale factors derived from $\sigma_{i\eta i\eta}$ are used in unifying procedure. For instance, for $t\bar{t}jets$ sample, we apply the $\sigma_{i\eta i\eta}$ fitting scale factors in table 6.13 on E_T^{miss} according to the photon type in each event. We then plot the E_T^{miss} after photon purity reweighting and compare with the original E_T^{miss} to get the unified scale factor for $t\bar{t}jets$. In this way, we derive the unified scale factors for $t\bar{t}jets$ and $t\bar{t}\gamma$ samples as listed in Table 6.14. To prove the scale factors do not alter the E_T^{miss} shape, we compare the E_T^{miss} ($t\bar{t}jets$ $+t\bar{t}\gamma$) corrected by the unified scale factors of each sample with the E_T^{miss} corrected by the scale factors of each photon type. The variation of E_T^{miss} is extremely limited, and well covered by uncertainties. The conclusion is the united scale factors are sufficient to be used for photon purity correction. In SR2, the purity related to two selected photons, the template fit can not be well performed due to the limited event number. Thus, we apply an uncertainty derived from the scale factor to cover the photon purity adjustment, details are described in section 6.6.

Channel	γ Purity	
e		
SR1	0.99 ± 0.04 (fit+stat.) ± 0.13 (syst.)	0.81 ± 0.05 (fit+stat.) ± 0.14 (syst.)
μ		
SR1	1.00 ± 0.03 (fit+stat.) ± 0.10 (syst.)	0.82 ± 0.04 (fit+stat.) ± 0.11 (syst.)

Table 6.14: Unified photon purity scale factors for $t\bar{t}jets$ and $t\bar{t}\gamma$ samples

6.5.6 Control Region Comparison

The performance of the simulation in describing the E_T^{miss} distribution of background processes is investigated by comparing data to backgrounds in the control regions. The control regions are defined by selecting "fake" photons (described in Section 6.3.3) and classified into CR1 and CR2 by fake multiplicity in the same way as the signal regions (see Section 6.4.3). By selecting events failing the nominal isolation or $\sigma_{i\eta i\eta}$ requirements yet passing the other requirements for photons, the control regions maintain the electromagnetic energy scale and resolutions of the signal region photons while greatly enhanced the photon-like jets contribution to the poorly measured and simulated E_T^{miss} backgrounds. Furthermore, by only

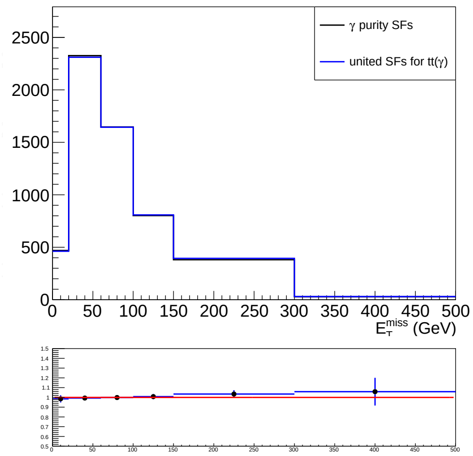

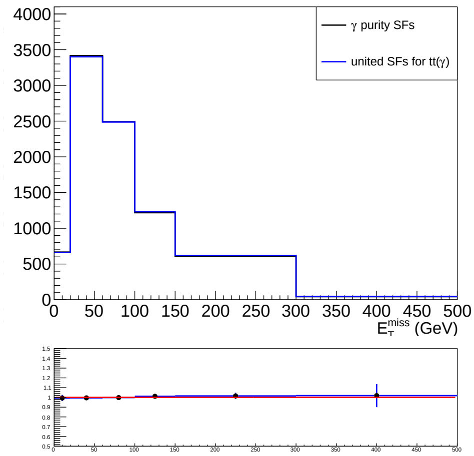

Figure 6.20: Comparison of the E_T^{miss} ($t\bar{t}jets$ $+t\bar{t}\gamma$) shape corrected by the unified scale factors (listed in Table 6.14) of each sample and corrected by the scale factors (listed in Table 6.13) of prompt photon and non-prompt photon. The electron (left) and muon (right) channels are shown both for SR1. The effect on the shape of the distribution is extremely small and well below statistical variations.

altering the photons in the control regions, the dominant effect on E_T^{miss} resolution by the $t\bar{t}$ system can be compared against the smaller effect of the photons.

The data and MC for the control regions are shown in Figure 6.21 with total event yields listed in Tables 6.15 and 6.16. The $t\bar{t}$ background contributes dominantly as the jet faked photon is selected for the control regions. The agreement is very good for one photon events in CR1 (within ∼5%). Considering the small sample size in CR2 and systematics, the overall ratios in CR2 are acceptable.

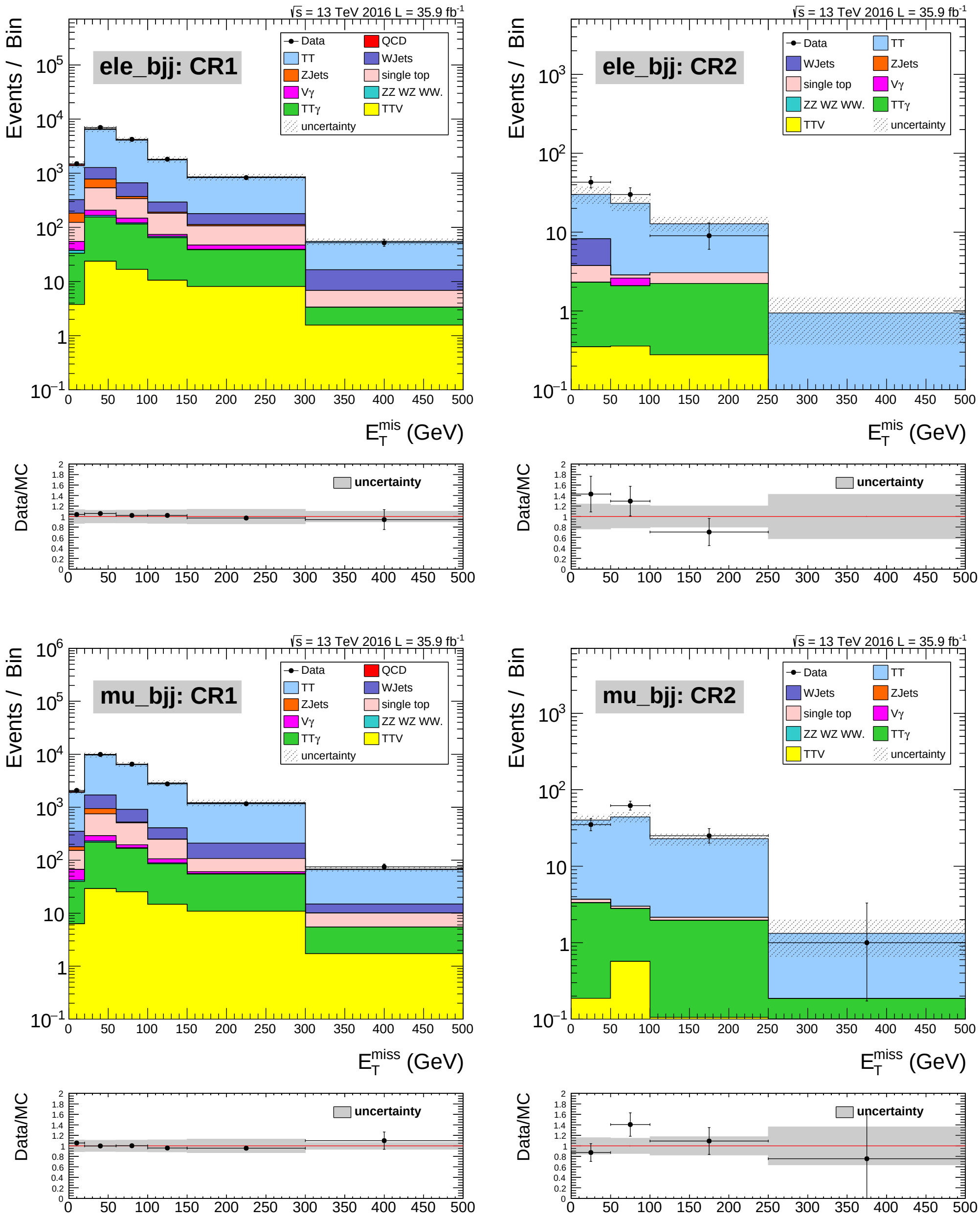

Figure 6.21: Comparison of data and MC in E_T^{miss} for the control regions. Electron (top) and muon (bottom) channels are shown for both CR1 (left) with one fake photon and CR2 (right) with two or more fake photons. The grey error bands in the ratio plots represent combined statistical and systematic uncertainties.

Channel	CR1	CR2
QCD	321.0 ± 11.2	–
$t\bar{t}$ + jets	$11800.3 \pm 64.8 \pm 1571.0$	$52.9 \pm 4.3 \pm 7.2$
W + jets	$1108.9 \pm 69.8 \pm 220.1$	$4.5 \pm 4.5 \pm 1.2$
Z + jets	$350.0 \pm 52.3 \pm 30.3$	–
Single t	$757.5 \pm 29.7 \pm 67.4$	$2.5 \pm 1.5 \pm 1.2$
Diboson	$25.9 \pm 3.9 \pm 2.5$	–
Vγ	$98.4 \pm 13.8 \pm 9.8$	$0.5 \pm 0.5 \pm 0.1$
$t\bar{t} + V$	$64.4 \pm 2.2 \pm 6.3$	$1.0 \pm 0.2 \pm 0.1$
$t\bar{t} + \gamma$	$345.6 \pm 7.2 \pm 33.8$	$5.6 \pm 0.9 \pm 0.5$
Total Background	$14872.7 \pm 114.4 \pm 1763.6$	$67.0 \pm 6.5 \pm 8.5$
Data	15405	82
Data/Bkgs	$1.03 \pm 0.01 \pm 0.12$	$1.22 \pm 0.15 \pm 0.17$

Table 6.15: Observed data and expected event yields and statistical uncertainties followed by systematic uncertainties in 35.87 fb^{-1} for the control regions in the electron channel.

Channel	CR1	CR2
QCD	568.3 ± 15.4	–
$t\bar{t}$ + jets	$18480.3 \pm 83.8 \pm 2124.0$	$100.6 \pm 6.2 \pm 12.3$
W + jets	$1579.2 \pm 80.7 \pm 323.1$	–
Z + jets	$239.3 \pm 44.5 \pm 21.6$	–
Single t	$1050.1 \pm 34.9 \pm 83.3$	$0.7 \pm 0.3 \pm 0.1$
Diboson	$24.2 \pm 3.9 \pm 2.4$	–
Vγ	$128.6 \pm 16.3 \pm 12.6$	–
$t\bar{t} + V$	$88.1 \pm 2.6 \pm 7.9$	$0.8 \pm 0.3 \pm 0.1$
$t\bar{t} + \gamma$	$483.3 \pm 8.6 \pm 45.4$	$7.4 \pm 1.1 \pm 0.7$
Total Background	$22575 \pm 132.4 \pm 2383.2$	$108.4 \pm 6.4 \pm 12.9$
Data	22514	123
Data/Bkgs	$1.00 \pm 0.01 \pm 0.11$	$1.13 \pm 0.11 \pm 0.15$

Table 6.16: Observed data and expected event yields and statistical uncertainties followed by systematic uncertainties in 35.87 fb^{-1} for the control regions in the muon channel.

6.6 Systematic Uncertainties

The systematic uncertainties are summarized in Table 6.17. For the MC simulated samples, the uncertainties of the lepton trigger and ID scale factors, photon ID scale factor, btagging scale factor and the luminosity are considered. For top pair productions, top pt reweighting uncertainty is included as described in 6.2.5. The systematics of user derived scale factors for JetM3 fit, electron faked photon and photon purity are considered. The uncertainty due to the limited sizes of generated samples varies for the different bins.

All systematic uncertainties are classified into two types: shape-based uncertainty and rate uncertainty. The shape-based uncertainty evaluates the Up($+1\sigma$)/ Down(-1σ) spectra which contribute to the limit calculation. Explicitly, for an event by event scale factor with uncertainty written as "$sf \pm 1\sigma_{sf}$", the spectrum of E_T^{miss} with "$sf + 1\sigma_{sf}$" applied event by event is taken as the "Up" shape of this uncertainty. Similarly, the spectrum with "$sf - 1\sigma_{sf}$" applied is taken as the "Down" shape. The rate uncertainty is applied to a dataset invariably and the corresponding spectrum varies by scaling only. Therefore, the rate uncertainty can be an input value to the limit calculation directly.

Luminosity: The recommended uncertainty on the total integrated luminosity is 2.5%. This affects all MC samples.

Pileup reweighting: The minimum bias cross-section used as input for the pileup reweighting procedure is varied by 4.6% as recommended.

Jet energy corrections: Jet energy scale and smearing are used in calculating the E_T^{miss} systematic. By shifting the uncertainty up and down, the E_T^{miss} spectra of signal region events are collected.

Lepton ID and trigger scale factors: The systematic uncertainty arising from lepton scale factors is evaluated by varying the scale factors up and down by their uncertainties. The uncertainties of ID, isolation and trigger are added in quadrature.

Photon ID scale factors: Photon scale factor and its corresponding uncertainty are prescribed by the EGamma POG [55]. The systematic uncertainty of the photon scale factors are evaluated by varying the scale factors up and down by their uncertainties.

Btagging reweighting: The reweighting for each event is calculated using scale factors [56] and MC b-tagging efficiencies as the method specified by the BTag SF [51]. The systematic uncertainty is evaluated by shifting the scale factors up and down.

Top quark P_T reweighting: The systematic uncertainty from the reweighting of top quark P_T in simulated top pair events is evaluated as follows: in the -1σ variation, no reweighting is applied at all, and in the $+1\sigma$ variation the reweighting is applied twice, i.e. the square of the weights is used.

User-derived scale factors: The user-derived scale factors include the scale factors for samples derived from JetM3 fit, photon purity adjustment and electron misidentification rate. The systematic uncertainties for these scale factors are re-measured with the fluctuations of all other systematic uncertainties and quadratic combined.

SR2 uncertainties derived from photon purity adjustment: The SR2 with two photons selected, the event number is very limited for the template fit, the square of the photon purity scale factors listed in Table 6.14 are used as an approximation, and the uncertainties are calculated accordingly. For instance, the photon purity scale factor for $t\bar{t}jets$ in electron channel SR1 is $0.99 \pm 14\%$ and square to $0.98 \pm 20\%$, instead of applying the square value to SR2 directly, we treat it as an uncertainty, whereas the $0.98 \pm 20\% = 0.78 \sim 1.18 = 1^{+18\%}_{-22\%}$, we take the maximum difference 22% as the uncertainty for this background without scaling it.

Fastsim MET uncertainty: The SUSY signal is Fastsim MC which requires special treatment due to the MET modeling. The MET uncertainty is evaluated by adding(Up)/subtracting(Down) the absolute difference between the spectra of genMET and pfMET.

MC statistics: Due to the limited statistics in the MC simulations, the uncertainty for each bin of E_T^{miss} is taken into account.

Source	Shape	Rate	Notes
Luminosity		2.5%	Signal and all backgrounds
Pileup		4.6%	”
Lepton ID/Trigger	✓		”
Photon ID	✓		”
JES	✓		”
b-tagging	✓		”
Top Quark P_T	✓		$t\bar{t}$+jets, $t\bar{t}+V$, $t\bar{t}\gamma$
Scale Factor of JetM3 fit($t\bar{t}$)		10 %	
Scale Factor of JetM3 fit($W + jets$)		18 %	
Scale Factor of photon purity fit($t\bar{t}$)		10 – 14 %	SR1 only
Scale Factor of photon purity fit($t\bar{t}\gamma$)		14 – 18 %	SR1 only
Scale Factor of electron fake photon fit($Zjets$)		45 %	Electron channel only
SR2 uncertainties derived from photon purity adjustment($t\bar{t}$)		14 – 22 %	SR2 only
SR2 uncertainties derived from photon purity adjustment($t\bar{t}\gamma$)		46 – 50 %	SR2 only
SUSY Signal Fastsim pfMET vs. genMET	✓		Signal only
SUSY Signal Cross Sections		10 – 30 %	Signal only

Table 6.17: Summary of systematic uncertainties. Each source is treated as a single, independent nuisance parameter in the upper limit calculation. Where range is given for the overall effect on rate, the range covers both the electron/muon channels and up/down fluctuations.

6.7 Results

In this section, we show the data compared with the expected standard backgrounds in pre-selected region, SR1 and SR2. While no photon is required in pre-selected region, one photon is required in SR1 and $\geq$2 photons in SR2. Only SR1 and SR2 are considered in shape comparisons for the limit calculation. The pre-selecting region serves as cross check.

Tables 6.18 and 6.19 show the total event yields for each channel in both SR1 and SR2 signal regions, and figures 6.22 - 6.27 show a number of kinematic and event-wide distributions in each channel. From the figures and tables, it can be observed that the SR1 is dominated by $t\bar{t}jets$ background with $t\bar{t}\gamma$ and $V + jets$ as the sub-dominant backgrounds. In the SR1 1-photon region, un-eliminated faked photon effects dominate, while in SR2 with $\geq$2 photons region, the faked photons effect are suppressed and $t\bar{t}jets$ and $t\bar{t}\gamma$ contribute equally.

While the total event yields do differ from the predicted backgrounds, the difference is well covered by the uncertainty. In the high E_T^{miss} region, the presence of signal should be sufficiently sensitive to the shape-based comparison. No clear discrepancy of shape is observable in all signal regions leading to the conclusion that we see no evidence of GMSB SUSY.

Channel	Pre-selection	SR1	SR2
QCD	59140 ± 152	–	–
$t\bar{t}$ + jets	844357 ± 548	4440 ± 39 ± 825	7.6 ± 1.5 ± 2.1
W + jets	202251 ± 938	645 ± 53 ± 129	–
Z + jets	47715 ± 754	1021 ± 102 ± 471	3.7 ± 3.5 ± 1.7
Single t	91906 ± 298	340 ± 19 ± 29	0.3 ± 0.1 ± 0.1
Diboson	3798 ± 49	30 ± 4 ± 3	–
Vγ	3680 ± 82	583 ± 35 ± 60	3.9 ± 2.1 ± 0.4
$t\bar{t} + V$	2450 ± 13	36.5 ± 1.4 ± 3.7	0.4 ± 0.1 ± 0.1
$t\bar{t} + \gamma$	5369 ± 30	1207 ± 12 ± 250	12.4 ± 1.4 ± 6.4
Total Background	1260665.7 ± 1367.8	8302 ± 128 ± 1193	28.2 ± 4.5 ± 7.4
T6ttZg(600_200)	269 ± 9	131 ± 6 ± 20	60 ± 4 ± 10
T6ttZg(800_400)	40 ± 1	19.7 ± 0.7 ± 3.3	7.5 ± 0.5 ± 1.4
Data	1253935	8618	35

Table 6.18: Observed data and expected event yields in 35.87 fb^{-1} for signal and backgrounds in the electron channel. The errors represented above are statistical followed by systematic for SR1 and SR2. Only statistical uncertainty is listed for pre-selected region.

Channel	Pre-selection	SR1	SR2
QCD	76319 ± 179	–	–
$t\bar{t}$ + jets	1333418 ± 717	6720 ± 50 ± 955	17.0 ± 2.5 ± 3.0
W + jets	282625 ± 1085	903 ± 61 ± 170	–
Z + jets	25893 ± 482	378 ± 55 ± 21	–
Single t	135055 ± 360	470 ± 22 ± 26	1.7 ± 1.6 ± 0.1
Diboson	5334 ± 58	28.3 ± 4.2 ± 1.6	–
Vγ	4477 ± 93	727 ± 39 ± 40	2.8 ± 1.3 ± 0.2
$t\bar{t} + V$	3513 ± 16	46.3 ± 1.7 ± 2.9	0.43 ± 0.14 ± 0.03
$t\bar{t} + \gamma$	7385 ± 33	1738 ± 15 ± 265	19.1 ± 1.6 ± 8.9
Total Background	1874021 ± 1449	11011 ± 107 ± 1114	41.0 ± 3.6 ± 9.6
T6ttZg(600_200)	333 ± 9	161 ± 7 ± 23	81 ± 5 ± 12
T6ttZg(800_400)	50 ± 1	20.8 ± 0.7 ± 3.2	10.0 ± 0.6 ± 1.6
Data	1853817	11478	43

Table 6.19: Observed data and expected event yields in 35.87 fb^{-1} for signal and backgrounds in the muon channel. The errors represented above are statistical followed by systematic for SR1 and SR2. Only statistical uncertainty is listed for pre-selected region.

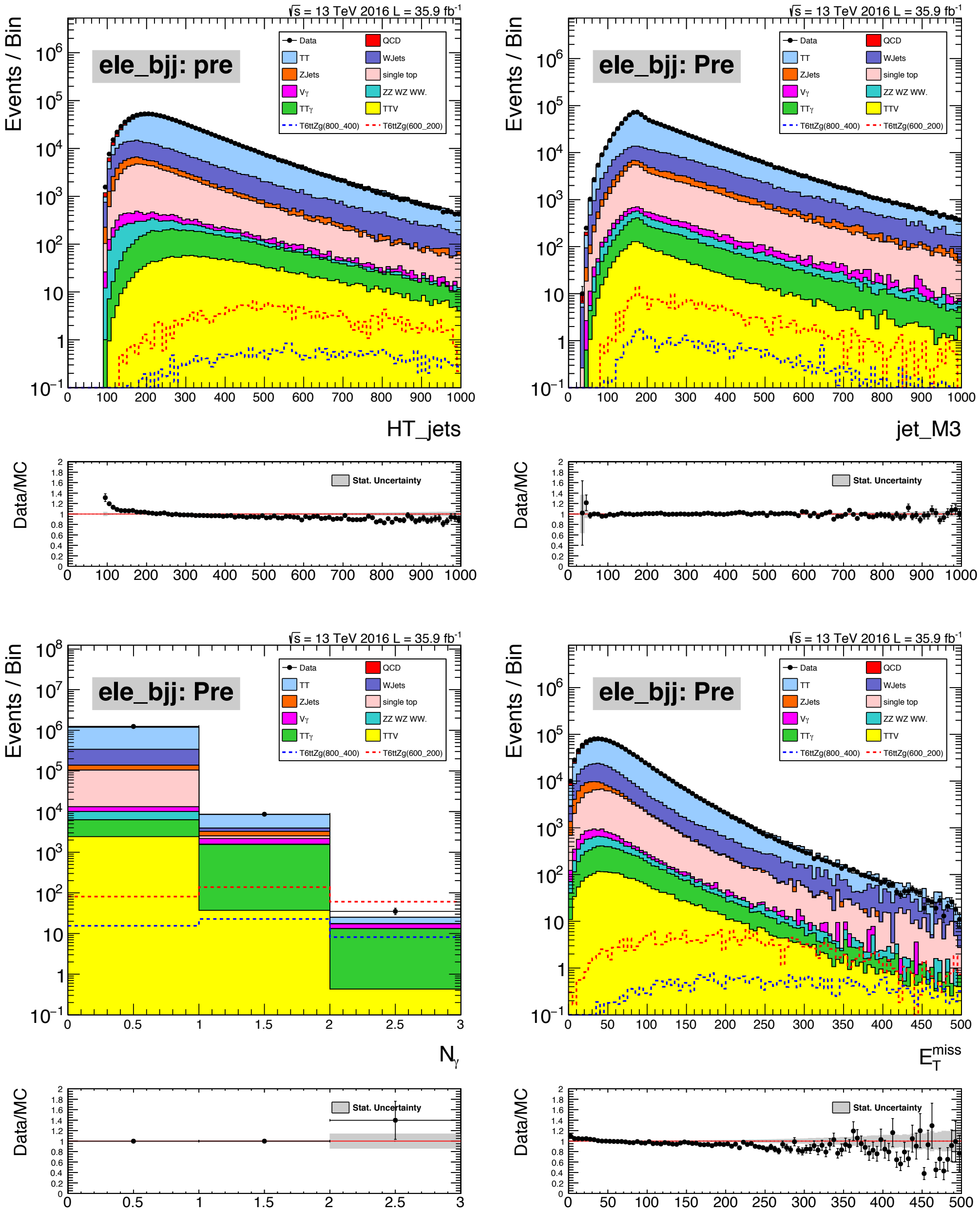

Figure 6.22: Comparison between data and MC in the electron pre-selection, the dark error bands in ratio plots represent statistical uncertainty only.

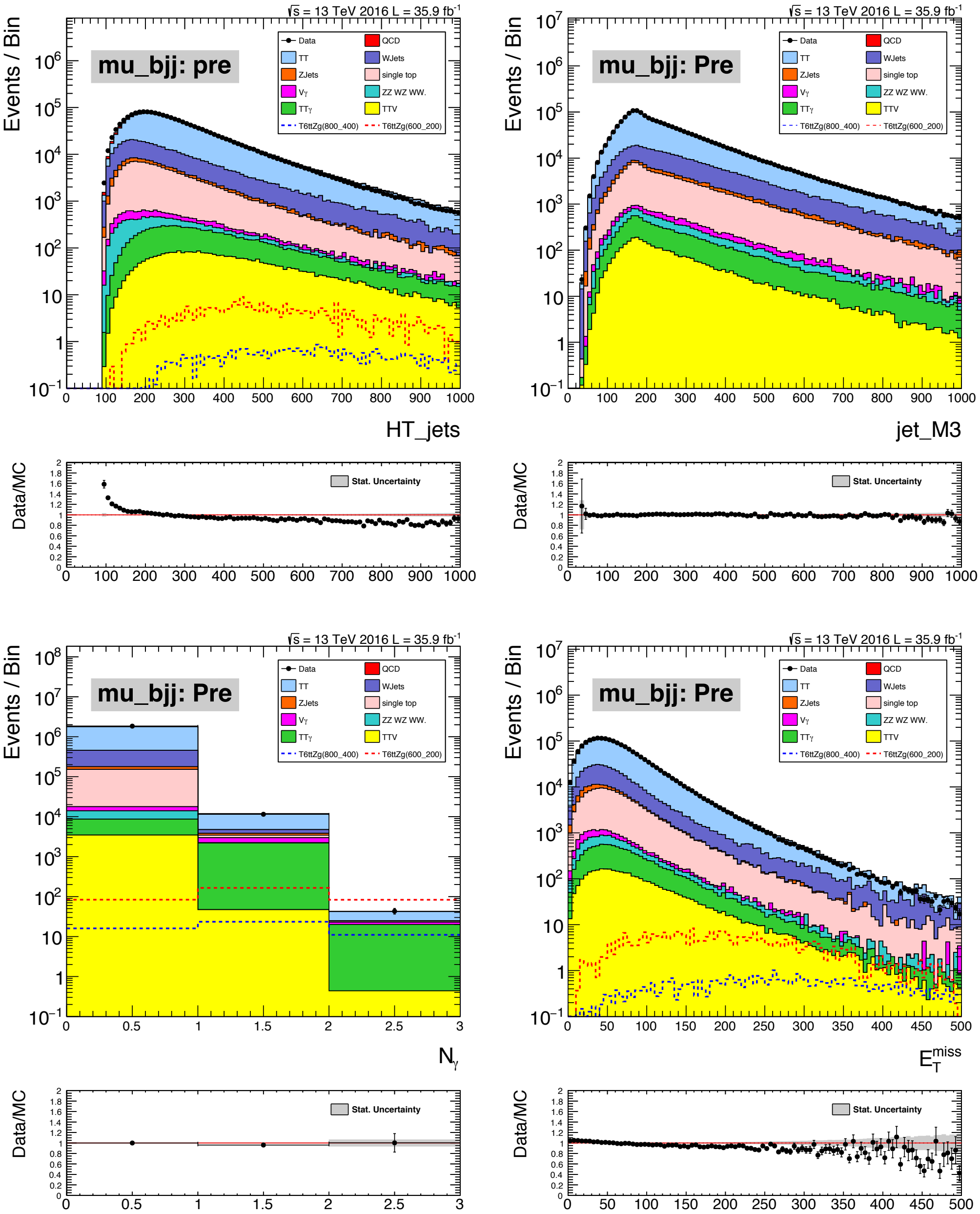

Figure 6.23: Comparison between data and MC in the μ pre-selection, the dark error bands in ratio plots represent statistical uncertainty only.

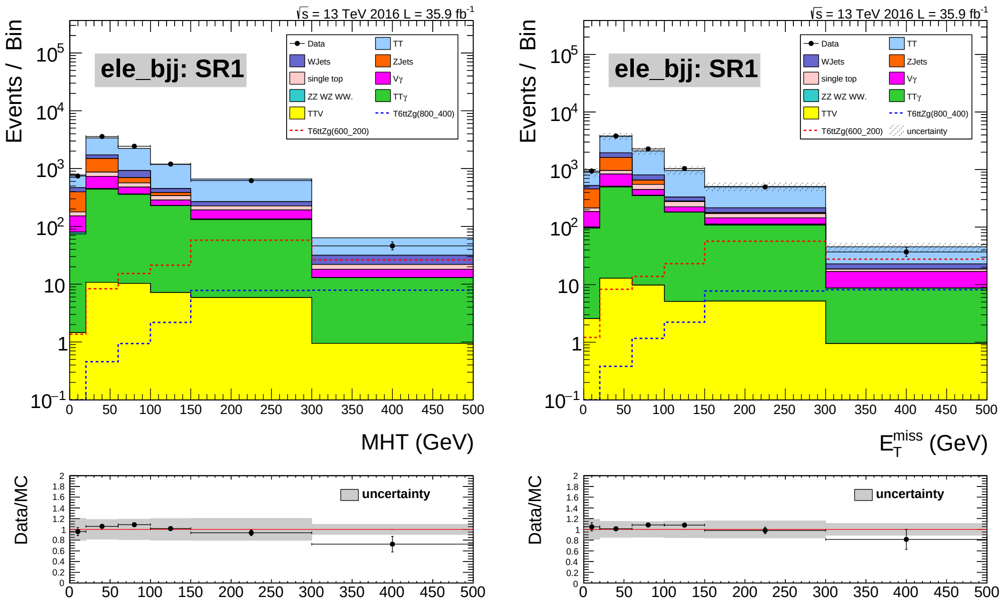

Figure 6.24: Comparison between data and MC in the electron channel in SR1, the dark error bands in ratio plots represents combined statistical and systematic uncertainties.

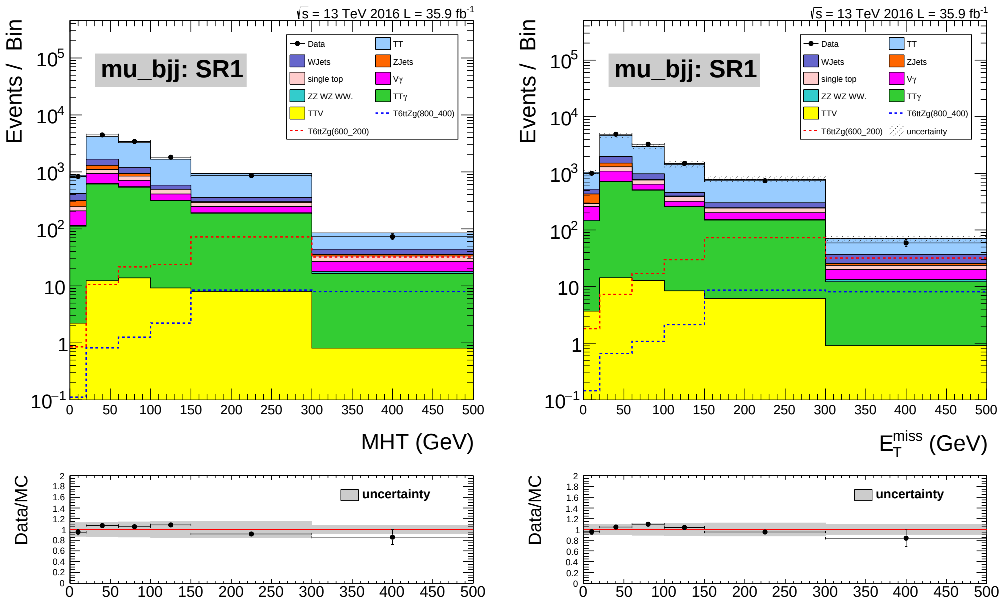

Figure 6.25: Comparison between data and MC in the muon channel in SR1, the dark error bands in ratio plots represent combined statistical and systematic uncertainties.

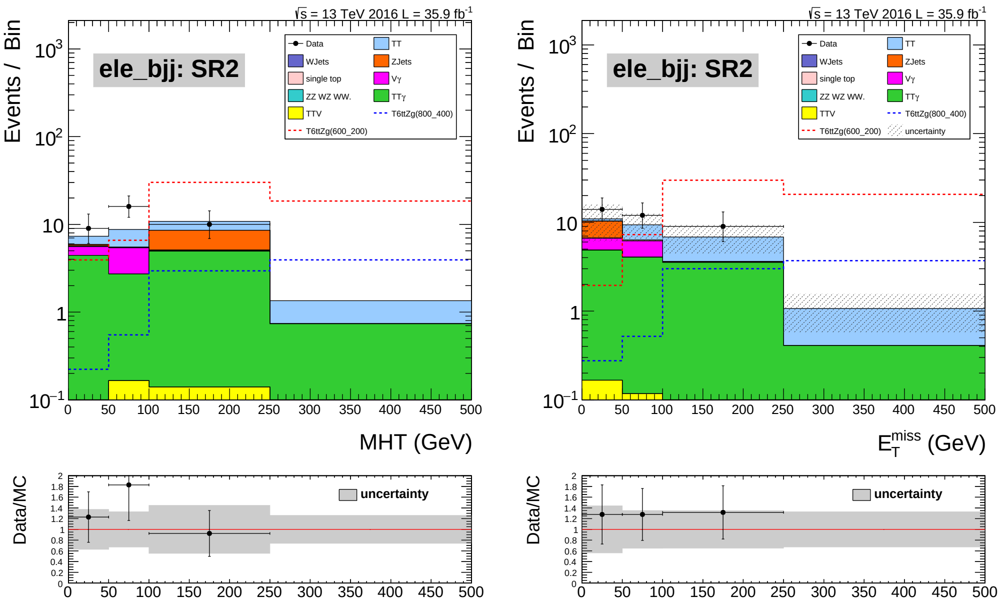

Figure 6.26: Comparison between data and MC in the electron channel in SR2, the dark error bands in ratio plots represent combined statistical and systematic uncertainties.

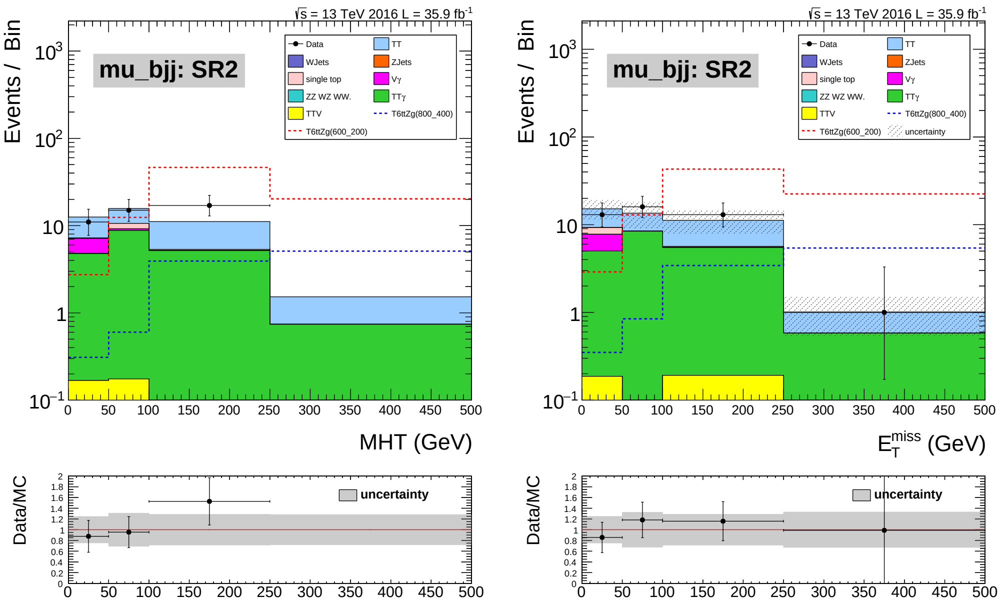

Figure 6.27: Comparison between data and MC in the muon channel in SR2, the dark error bands in ratio plots represent combined statistical and systematic uncertainties.

Chapter 7

Interpretation of Results

In the absence of a statistically significant shape-based excess of observed data over the expected background, we interpret the results of this analysis as upper limits on the cross section of the GMSB reweighted T6ttZg SUSY production using the Asymptotic CL_S method [57] [58] implemented by the combined limit setting tools developed for CMS analysis [59].

There are two channels: Electron channel and Muon channel, each with two signal regions: SR1 and SR2 contributing to the combined limit calculation, including distinct background processes: $t\bar{t}jets$, $W+$ jets, $Z+$ jets, single top, diboson, $t\bar{t}$ $+V$, $V\gamma$, and $t\bar{t}$ $+\gamma$. The shape of the E_T^{miss} distribution is divided into bins with lower edges 0, 20, 60, 100, 150, and 300 GeV with the final bin extending to 500 GeV for the SR1, and 0, 50, 100, 250 with the final bin extending to 500 GeV for the SR2. Figure 7.1 re-lists these four E_T^{miss} plots and table 7.1 lists the expected background yields in each bin for each region and channel.

For each mass point on the grid of the stop-bino masses, the observed upper limit is calculated at 95% C.L. by using the observed data, expected backgrounds, and signal yields. The expected upper limits are calculated using the expected backgrounds and signal yields. A large set of background only “pseudo-data” is generated and the cross-section at 95% C.L. is calculated for each of them and the probability distribution is built accordingly. The value at which the cumulative probability distribution covers the quantile of 50% is the median expected cross section. The $\pm 1\sigma$ (68%) is defined by the crossings of the 16% and 84% quantiles. Crossings at 2.5% and 97.5% define the $\pm 2\sigma$ (95%).

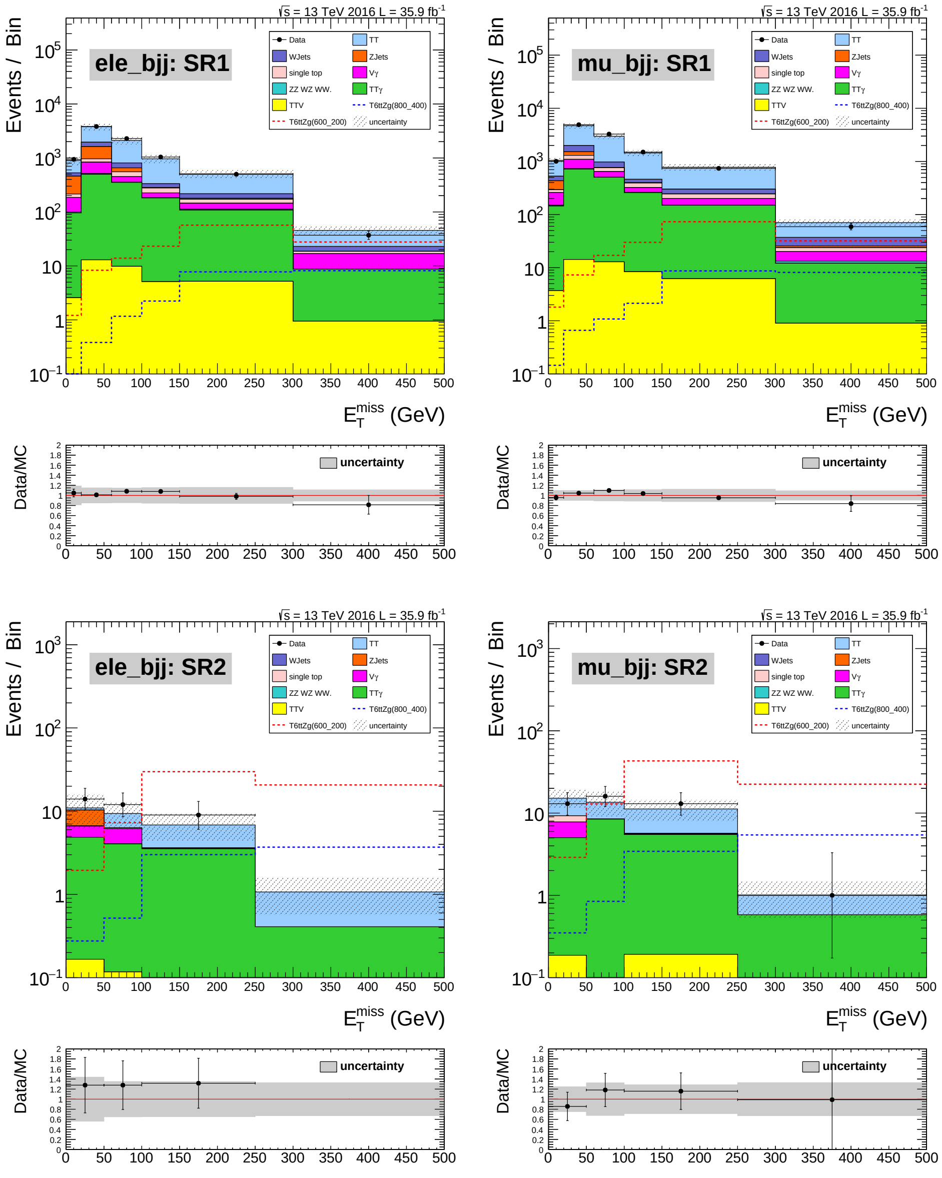

Figure 7.1: Comparison of the of observed data and predicted backgrounds in SR1 (top) and SR2 (bottom) for electron (left) and muon (right) channels.

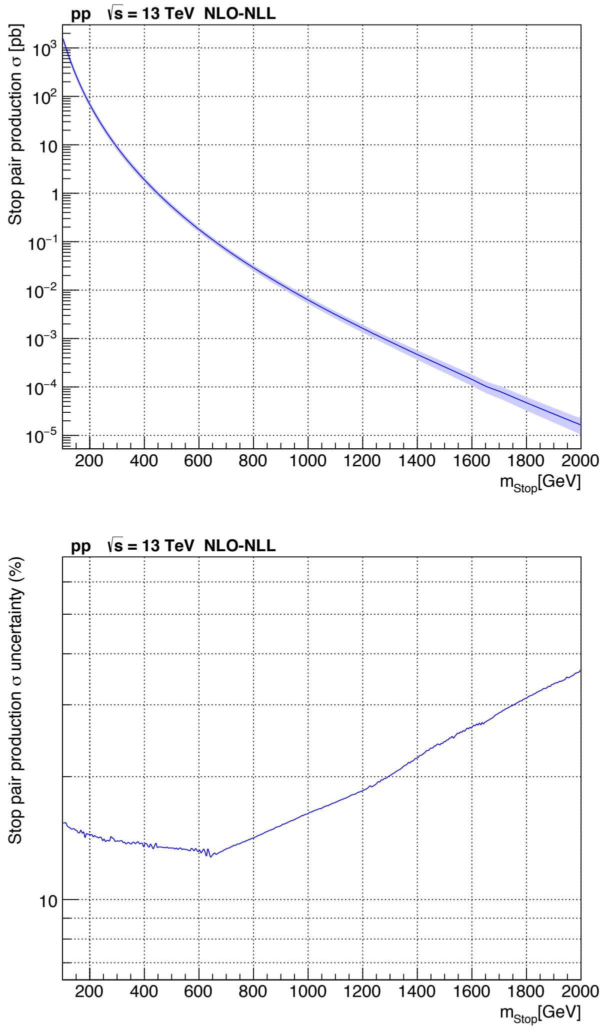

Figure 7.2: NLO + NLL cross sections (top) and relative uncertainties (bottom) for stop-pair production, plotted using the data from reference [15]. The theoretical uncertainties are estimated due to the uncertainties of scale variation and the parton distribution functions.

E_T^{miss} (GeV)	Electron channel		Muon Channel	
	Backgrounds	Data	Backgrounds	Data
SR1				
< 20	898 $\pm 59 \pm 168$	941	1049 $\pm 41 \pm 103$	1004
20 - 60	3779 $\pm 96 \pm 569$	3820	4694 $\pm 76 \pm 464$	4907
60 - 100	2109 $\pm 51 \pm 308$	2282	2977 $\pm 49 \pm 324$	3269
100 - 150	964 $\pm 26 \pm 149$	1040	1444 $\pm 31 \pm 164$	1499
150 - 300	508 $\pm 21 \pm 81$	498	777 $\pm 25 \pm 95$	740
> 300	46 $\pm 7 \pm 7$	37	70 $\pm 9 \pm 9$	59
SR2				
< 50	11.0 $\pm 3.7 \pm 4.8$	14	15.2 $\pm 2.7 \pm 3.8$	13
50 - 100	9.4 $\pm 2.3 \pm 3.3$	12	13.5 $\pm 1.7 \pm 4.4$	16
100 - 250	6.8 $\pm 1.2 \pm 2.4$	9	11.2 $\pm 1.7 \pm 3.2$	13
> 250	1.1 $\pm 0.5 \pm 0.5$	0	1.0 $\pm 0.5 \pm 0.5$	1

Table 7.1: Expected total background yields and observed data in each bin of SR1 and SR2 for both electron and muon channels. The errors represented above are statistical followed by systematic.

The observed and expected cross sections of each mass points are compared with the theoretical value. The theoretical cross sections is assumed only depend on the stop quark masses as shown in the Figure 7.3. Only on-shell productions are considered giving the cut off of the region $m_{\tilde{t}} - m_{\tilde{B}^0} < m_t$. The mass points where the observed cross section is less than the theoretical prediction are excluded in the observed upper limit. It is the same procedure used to derive the expected upper limits. These limits give the 95% Confidence Level mass exclusion contour as shown in Figures 7.4 and 7.5 of two plotting styles. Stop masses of 850-1000 GeV/c^2 are excluded depending on bino masses. The region on the left side of the exclusion contours are excluded. The observed limit contours are slightly higher than the expected, indicating a small deviation of the observed data from the background predictions. Considering the observed and expected limits are consistent within the $\pm 1\sigma$ uncertainty, the results are robust.

Besides the combined limits, the limit setting procedures are performed for electron channel and muon channel separately. Figures 7.6 and 7.7 show the exclusion contours for two channels. Muon channel indicates better consistency than electron channel.

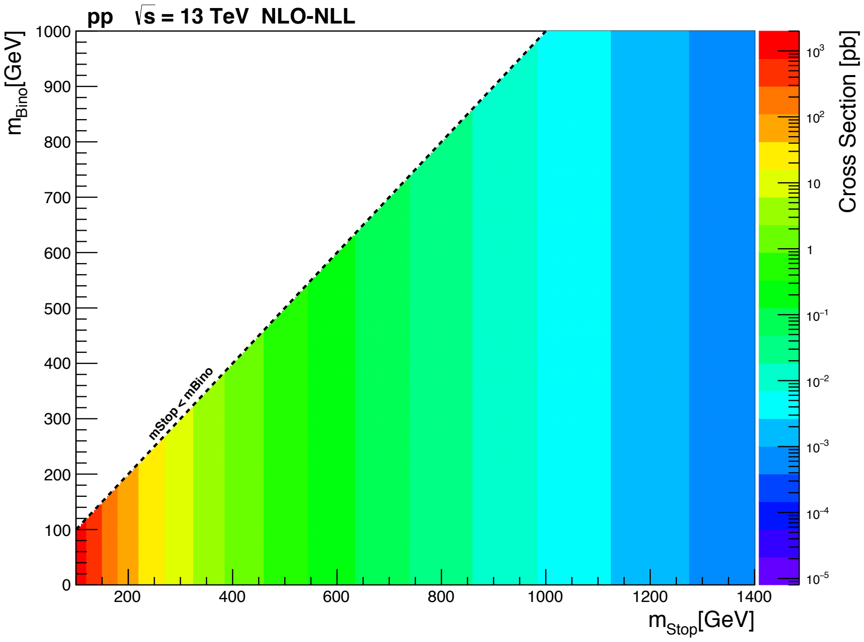

Figure 7.3: theoretical NLO + NLL cross sections of stop-bino.

SMS Interpretation

As discussed in section 3.4, the result of this analysis is also interpreted privately in the context of simplified supersymmetry models (SMS). The exclusion contour for model SMS-T6ttHG is shown in Figure 7.8 of the stop-NLSP mass plane where the NLSP decays to $50\%\gamma/50\%Z+$ LSP. Similarly, the exclusion contour for estimated SMS-T6ttHG model is shown in Figure 7.9 of the stop-NLSP mass plane where the NLSP decays to $50\%\gamma/50\%H^0$+LSP. Since no centrally produced T6ttHG samples are available, the T6ttHG events are reweighted from the T6ttZG sample by applying the ratio of $H^0 \to b\bar{b}/Z \to b\bar{b} \sim 3.8$.

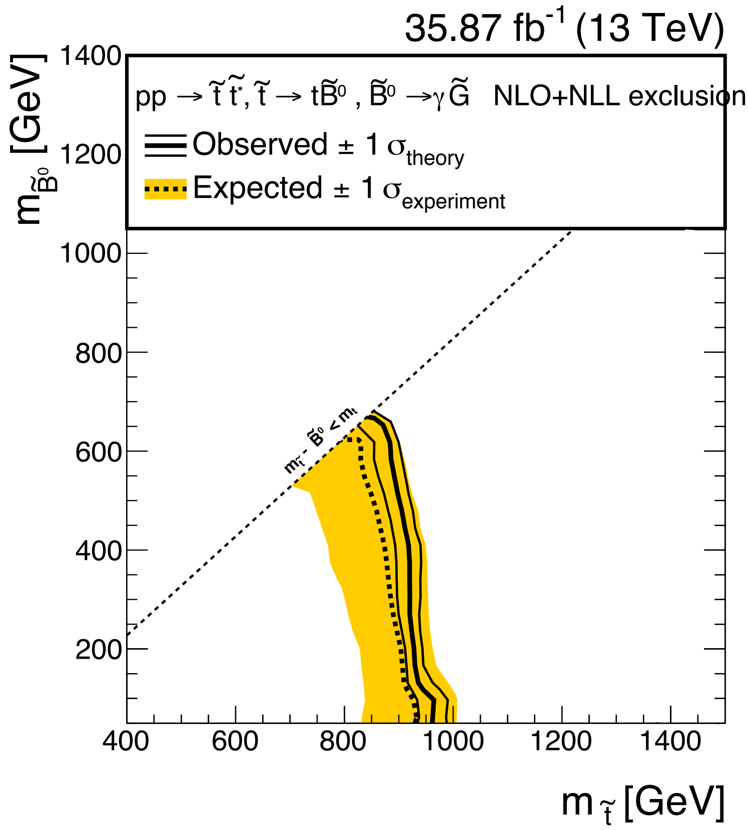

Figure 7.4: 95% C.L. exclusion contours in band style displays the $\pm 1\sigma$ bands as from expected and observed predictions for GMSB reweighted T6ttZg model. The mass points on the left side of the exclusion contours are excluded.

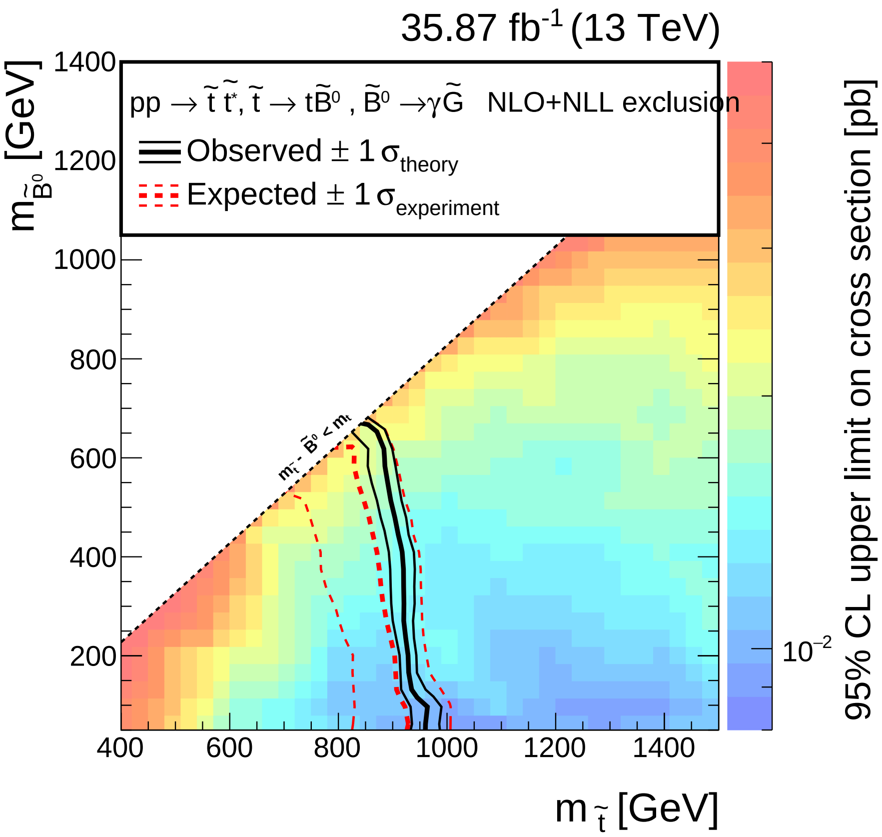

Figure 7.5: 95% C.L. exclusion contours in palette style displays the $\pm 1\sigma$ bands as from expected and observed predictions for GMSB reweighted T6ttZg model, the background palette shows the expected cross sections. The mass points on the left side of the exclusion contours are excluded.

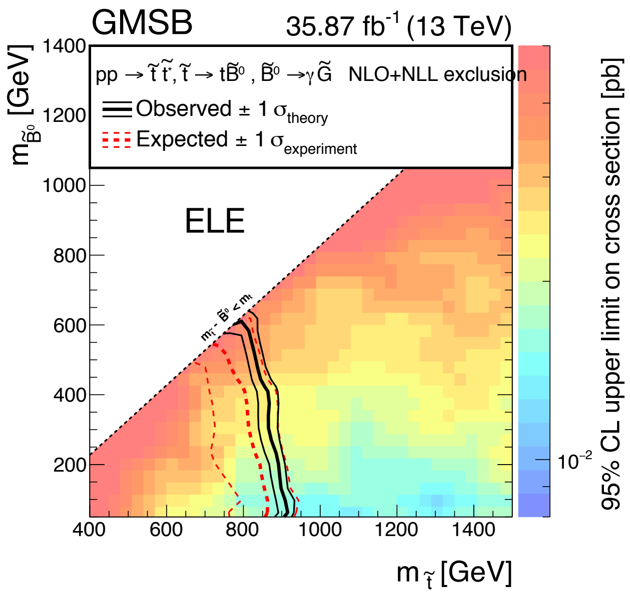

Figure 7.6: 95% C.L. exclusion contours in palette style displays the $\pm 1\sigma$ bands as from expected and observed predictions for GMSB reweighted T6ttZg model in electron channel, the background palette shows the expected cross sections. The mass points on the left side of the exclusion contours are excluded.

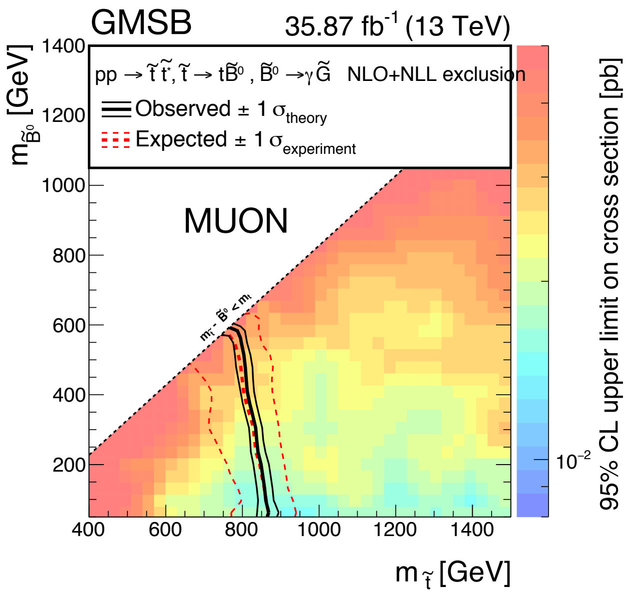

Figure 7.7: 95% C.L. exclusion contours in palette style displays the $\pm 1\sigma$ bands as from expected and observed predictions for GMSB reweighted T6ttZg model in muon channel, the background palette shows the expected cross sections. The mass points on the left side of the exclusion contours are excluded.

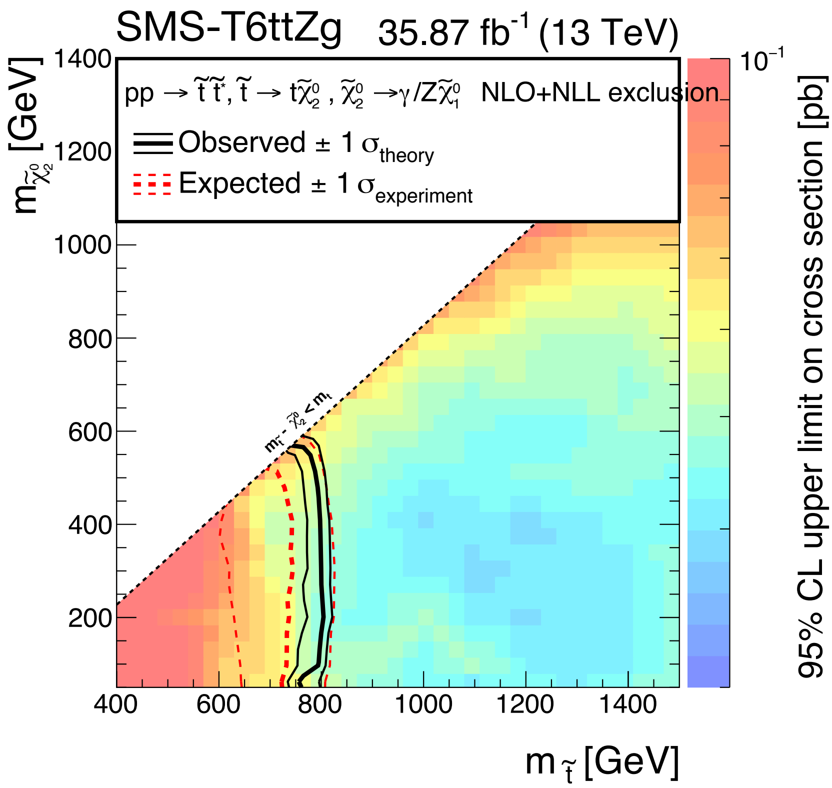

Figure 7.8: 95% C.L. exclusion contours in palette style displays the $\pm 1\sigma$ bands as from expected and observed predictions for SMS-T6ttZG model, the background palette shows the expected cross sections. The mass points on the left side of the exclusion contours are excluded.

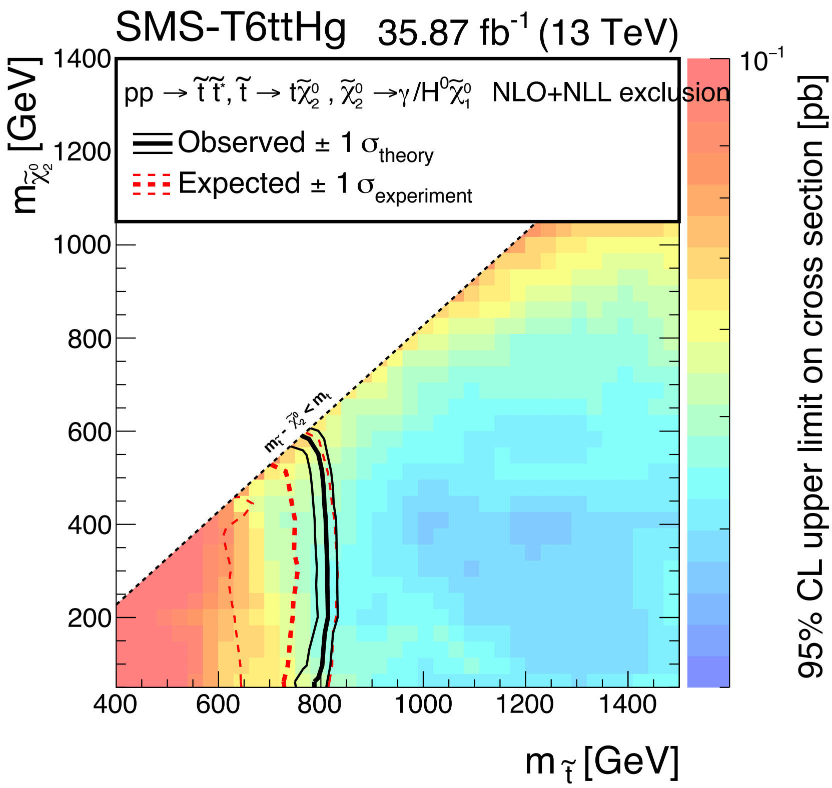

Figure 7.9: 95% C.L. exclusion contours in palette style displays the $\pm 1\sigma$ bands as from expected and observed predictions for SMS-T6ttHG(T6ttZG reweighted) model, the background palette shows the expected cross sections. The mass points on the left side of the exclusion contours are excluded.

Chapter 8

Conclusions

In this dissertation, I presented a search for Gauge Mediated Supersymmetry Breaking in top squark pair production by selecting events with at least one photon and using the lepton+jets decay channel of the $t\bar{t}$ system. The full RunII 2016 data corresponding to 35.87 fb^{-1} of proton-proton collisions is analyzed. The comparison of data to SM backgrounds indicates no significant deviation in the distribution of E_T^{miss} between the standard model expectation and the observed data.

The data results and all related uncertainties are used to calculate upper limits as the prediction for a range of top squark and bino-like neutralino masses in the GMSB SUSY model, and have defined exclusion regions reaching top squark masses upto 1000 GeV/c^2. Comparing to the similar study [60] made at $\sqrt{s}$ = 8 TeV, corresponding to an integrated luminosity of 19.7 fb^{-1}, we enhance the exclusion regions by about 250 GeV/c^2 of top squark mass as illustrated in Figure 8.1.

For the future upgrade of this analysis, some thoughts might help with signal discrimination, like improving signal strength with the multi-btagging cut and top quark reconstruction for larger datasets. The interpretation of final state can include the new signal production of higgsino-like neutralino.

From the analysis using the 2016 datasets of RunII, we find no evidence for the presence of SUSY existence. The analyses using 2017 and 2018 datasets are on going, the total luminosity of RunII is reaching about 150 fb^{-1}, resulting in 3 times more data. RunIII is planned after recommissioning in 2021 following a long shutdown that started at the end of 2018. The upgraded HL-LHC and CMS detector are going to start operation in 2026. These improvements will offer far

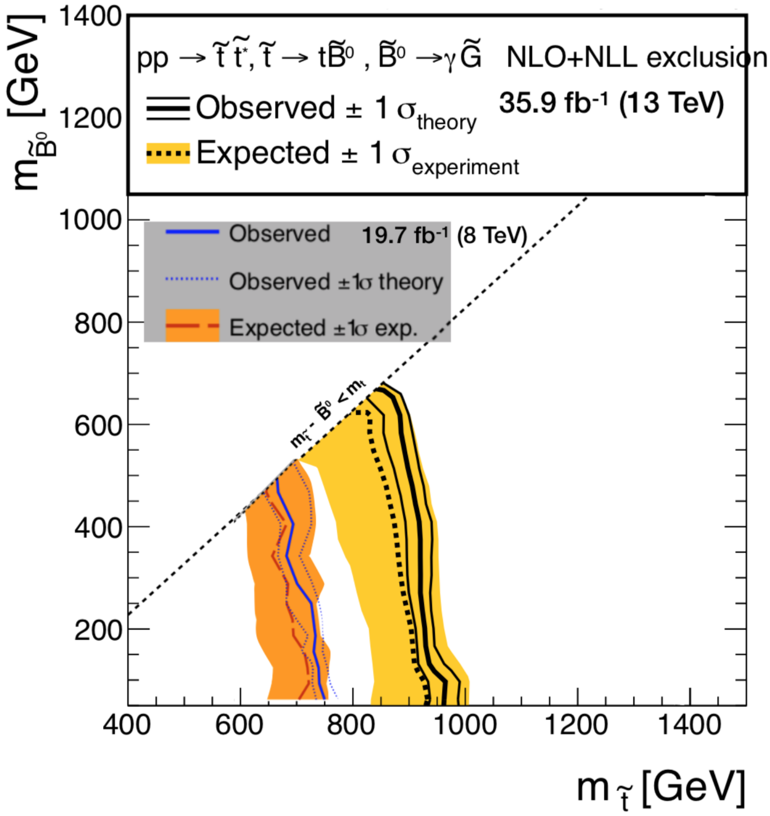

Figure 8.1: The exclusion contours of this analysis compare with the result of the similar study made at 8 TeV. The top squark mass is excluded about 250 GeV/c^2 higher.

greater chances for new physics discovery. The SUSY searches is still exciting, and we are very looking forward for the future physics results.

Appendix

A Top P_T reweighiting comparison

In section 6.2.5, it is mentioned that the observed top pair production exhibit the softer P_T spectrum than the simulated Monte Carlo samples. The jet multiplicity and H_T (Scalar Sum of the transverse energy of all jets in an event) are expected to be softer. After the top P_T reweighting for the simulated samples, the spectra are softer as shown in the Figure 8.2.

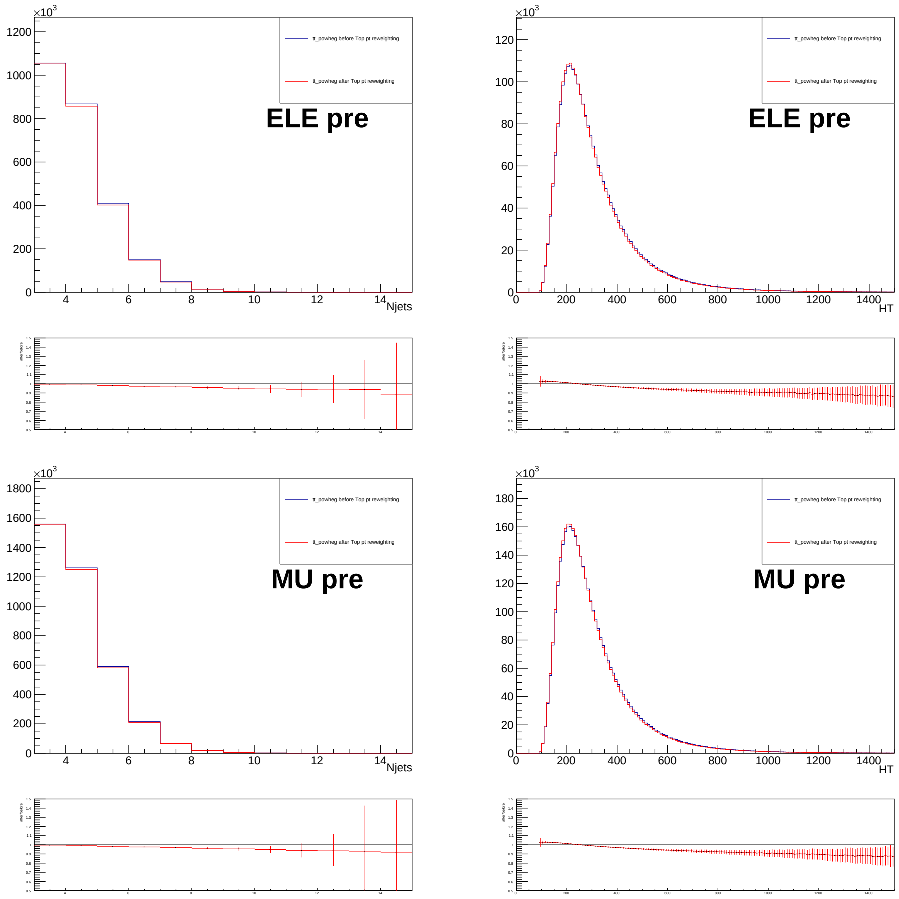

Figure 8.2: Comparison of Njets(left) and HT(right) before(blue hist) and after(red hist) the top Pt reweighting for TT_powheg sample. Ratio plots is after/before, these show Njets and HT are softer after the reweighting. Both the pre-selected regions of electron (top) and muon (bottom) channels are shown. For the region definitions, refer to section 6.4.4.

B Binning χ^2 test

The χ^2 goodness test is made for the control regions in both channels, to check the compatibility between the data and expected backgrounds, and to check the binning schemes. The test results are listed in Figure 8.3 . According to the p-values, the hypothesis of the identical of the data and backgrounds histograms can be accepted for 0.05 significant level. The binning strategy is acceptable considering the statistical uncertainty, and is used for signal regions. The detailed test method can refer to the reference [61].

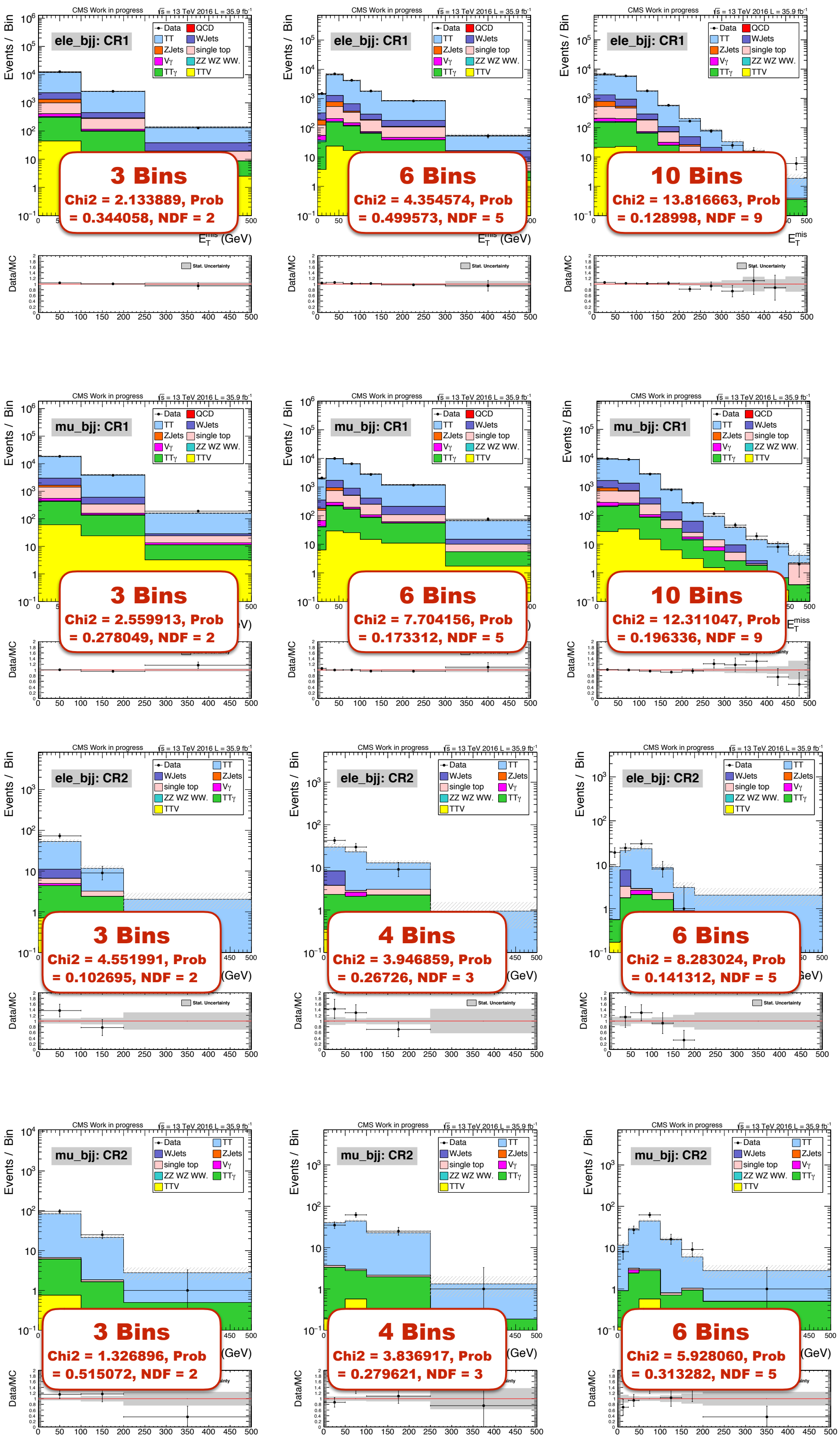

Figure 8.3: Chi2 goodness test for the control regions.

Bibliography

[1] S. Chatrchyan, V. Khachatryan, and A. Sirunyan, “Observation of a new boson at a mass of 125 GeV with the CMS experiment at the LHC”, *Physics Letters B* **716** (2012), no. 1, 30 – 61, doi:https://doi.org/10.1016/j.physletb.2012.08.021.

[2] G. Aad, T. Abajyan, and B. Abbott, “Observation of a new particle in the search for the Standard Model Higgs boson with the ATLAS detector at the LHC”, *Physics Letters B* **716** (2012), no. 1, 1 – 29, doi:https://doi.org/10.1016/j.physletb.2012.08.020.

[3] M. Swinbank, “Distant galaxies lack dark matter”, *Nature* **543** (03, 2017) 318 EP –.

[4] S. P. Martin, “A Supersymmetry primer”, doi:10.1142/9789812839657_0001,10.1142/9789814307505_0001, arXiv:hep-ph/9709356. [Adv. Ser. Direct. High Energy Phys.18,1(1998)].

[5] CMS Collaboration, “CMS SUSY Public Results”. https://twiki.cern.ch/twiki/bin/view/CMSPublic/PhysicsResultsSUS.

[6] “Public CMS Luminosity Information”. https://twiki.cern.ch/twiki/bin/view/CMSPublic/LumiPublicResults.

[7] J.-L. Caron, “LHC Layout”. https://cds.cern.ch/record/841568.

[8] https://cms.cern/detector.

[9] V. Halyo, P. LeGresley, and P. Lujan, “Massively Parallel Computing and the Search for Jets and Black Holes at the LHC”, *Nucl. Instrum. Meth.* **A744** (2014) 54–60, doi:10.1016/j.nima.2014.01.038, arXiv:1309.6275.

[10] D. Barney and P. de Barbaro, “CMS Calorimetry Introduction for Newcomers”.

[11] CMS Collaboration, “CMS reconstruction improvement for the muon tracking by the RPC chambers”, *JINST* **8** (2013) T03001, doi:10.1088/1748-0221/8/03/T03001.

[12] P. Charitos, “Deep learning and the quest for new physics at the LHC”. https://ep-news.web.cern.ch/content/deep-learning-and-quest-new-physics-lhc.

[13] CMS Collaboration, “ElectronTagAndProbe”. https://twiki.cern.ch/twiki/bin/view/CMSPublic/ElectronTagAndProbe.

[14] CMS Collaboration, “MuonSFRun2_2016”. https://twiki.cern.ch/twiki/bin/view/CMS/MuonWorkInProgressAndPagResults#Results_on_the_full_2016_data.

[15] CMS Collaboration, “SUSY SMS CrossSection of Stop-antistop at 13TeV”. https://twiki.cern.ch/twiki/bin/view/LHCPhysics/SUSYCrossSections13TeVstopsbottom.

[16] S. L. Glashow, “Partial-symmetries of weak interactions”, *Nuclear Physics* **22** (1961), no. 4, 579 – 588, doi:https://doi.org/10.1016/0029-5582(61)90469-2.

[17] S. Weinberg, “A Model of Leptons”, *Phys. Rev. Lett.* **19** (Nov, 1967) 1264–1266, doi:10.1103/PhysRevLett.19.1264.

[18] A. Salam, “Weak and Electromagnetic Interactions”, *Conf. Proc.* **C680519** (1968) 367–377.

[19] H. D. Politzer, “Reliable Perturbative Results for Strong Interactions?”, *Phys. Rev. Lett.* **30** (Jun, 1973) 1346–1349, doi:10.1103/PhysRevLett.30.1346.

[20] D. J. Gross and F. Wilczek, “Ultraviolet Behavior of Non-Abelian Gauge Theories”, *Phys. Rev. Lett.* **30** (Jun, 1973) 1343–1346, doi:10.1103/PhysRevLett.30.1343.

[21] G. S. GURALNIK, "THE HISTORY OF THE GURALNIK, HAGEN AND KIBBLE DEVELOPMENT OF THE THEORY OF SPONTANEOUS SYMMETRY BREAKING AND GAUGE PARTICLES", *International Journal of Modern Physics A* **24** (2009), no. 14, 2601–2627, `doi:10.1142/S0217751X09045431`, `arXiv:https://doi.org/10.1142/S0217751X09045431`.

[22] V. Trimble, "Existence and nature of dark matter in the universe", *araa* **25** (1987) 425–472, `doi:10.1146/annurev.aa.25.090187.002233`.

[23] G. Bertone, D. Hooper, and J. Silk, "Particle dark matter: evidence, candidates and constraints", *Physics Reports* **405** (2005), no. 5, 279 – 390, `doi:https://doi.org/10.1016/j.physrep.2004.08.031`.

[24] I. Aitchison, "Supersymmetry in Particle Physics: An Elementary Introduction". Cambridge University Press, 2007.

[25] M. Dine, A. E. Nelson, and Y. Shirman, "Low energy dynamical supersymmetry breaking simplified", *Phys. Rev. D* **51** (Feb, 1995) 1362–1370, `doi:10.1103/PhysRevD.51.1362`.

[26] P. Meade, N. Seiberg, and D. Shih, "General Gauge Mediation", *Progress of Theoretical Physics Supplement* **177** (2009) 143–158, `doi:10.1143/PTPS.177.143`.

[27] P. Meade, M. Reece, and D. Shih, "Prompt decays of general neutralino NLSPs at the Tevatron", *Journal of High Energy Physics* **2010** (May, 2010) 105, `doi:10.1007/JHEP05(2010)105`.

[28] J. Alwall, P. C. Schuster, and N. Toro, "Simplified models for a first characterization of new physics at the LHC", *Phys. Rev. D* **79** (Apr, 2009) 075020, `doi:10.1103/PhysRevD.79.075020`.

[29] LHC New Physics Working Group Collaboration, "Simplified Models for LHC New Physics Searches", *J. Phys.* **G39** (2012) 105005, `doi:10.1088/0954-3899/39/10/105005`, `arXiv:1105.2838`.

[30] ATLAS Collaboration, "ATLAS SUSY Public Results". https://atlas.web.cern.ch/Atlas/GROUPS/PHYSICS/CombinedSummaryPlots/SUSY/.

[31] W. Herr and B. Muratori, "Concept of luminosity". https://cds.cern.ch/record/941318/files/p361.pdf.

[32] CMS Collaboration, "The CMS experiment at the CERN LHC", *JINST* **3** (2008) S08004, doi:10.1088/1748-0221/3/08/S08004.

[33] CMS Collaboration, "The CMS tracker system project : Technical Design Report", Technical Report CERN-LHCC-98-006, CERN, 1998.

[34] V. Veszpremi, "Operation and performance of the CMS tracker", *JINST* **9** (2014) C03005, doi:10.1088/1748-0221/9/03/C03005.

[35] CMS Collaboration, "Description and performance of track and primary-vertex reconstruction with the CMS tracker", *JINST* **9** (2014) P10009, doi:10.1088/1748-0221/9/10/P10009.

[36] CMS Collaboration, "The CMS electromagnetic calorimeter project : Technical Design Report", Technical Report CERN-LHCC-97-033, CERN, 1997.

[37] CMS Collaboration, "Changes to CMS ECAL electronics : addendum to the Technical Design Report", Technical Report CERN-LHCC-2002-027, CERN, 2002.

[38] CMS Collaboration, "The CMS hadron calorimeter project : Technical Design Report", Technical Report CERN-LHCC-97-031, CERN, 1997.

[39] CMS Collaboration, "The CMS muon project : Technical Design Report", Technical Report CERN-LHCC-97-032, CERN, 1997.

[40] CMS Collaboration, "CMS The TriDAS Project : Technical Design Report, Volume 2: Data Acquisition and High-Level Trigger", Technical Report CERN-LHCC-2002-026, CERN, 2002.

[41] CMS Collaboration, "Particle-Flow Event Reconstruction in CMS and Performance for Jets, Taus, and MET", Technical Report CMS-PAS-PFT-09-001, CERN, 2009.

[42] CMS Collaboration, "Commissioning of the Particle-flow Event Reconstruction with the first LHC collisions recorded in the CMS detector", Technical Report CMS-PAS-PFT-10-001, CERN, 2010.

[43] CMS Collaboration, "Reconstruction of Electron Tracks With the Gaussian-Sum Filter in the CMS tracker at LHC", Technical Report CMS Note RN 2003-001, CERN, 2003.

[44] G. S. Matteo Cacciari1, Gavin P. Salam1, "The anti-k_t jet clustering algorithm", *Journal of High Energy Physics* **04** (2008) 063, doi:10.1088/1126-6708/2008/04/063, arXiv:0802.1189.

[45] CMS Collaboration, "CMSSW Application Framework". https://twiki.cern.ch/twiki/bin/view/CMSPublic/WorkBookCMSSWFramework.

[46] CERN, "ROOT: Data Analysis Framework". https://root.cern.ch/.

[47] CMS Collaboration, "SummaryTable1G25ns". https://twiki.cern.ch/twiki/bin/viewauth/CMS/SummaryTable1G25ns.

[48] CMS Collaboration, "TopPtReweighting2017". https://twiki.cern.ch/twiki/bin/view/CMS/TopPtReweighting2017.

[49] CMS Collaboration, "ElectronSFRun2_2016". https://twiki.cern.ch/twiki/bin/view/CMS/EgammaIDRecipesRun2#Electron_efficiencies_and_scale.

[50] CMS Collaboration, "PhotonSFRun2_2016". https://twiki.cern.ch/twiki/bin/view/CMS/EgammaIDRecipesRun2#Photon_efficiencies_and_scale_fa.

[51] CMS Collaboration, "BTagSFMethods_1a". https://twiki.cern.ch/twiki/bin/view/CMS/BTagSFMethods#1a_Event_reweighting_using_scale.

[52] CMS Collaboration, “MissingETOptionalFiltersRun2”. https://twiki.cern.ch/twiki/bin/view/CMS/MissingETOptionalFiltersRun2#Moriond_2017.

[53] R. Barlow and C. Beeston, “Fitting using finite Monte Carlo samples”, *Computer Physics Communications* **77** (1993), no. 2, 219 – 228, doi:https://doi.org/10.1016/0010-4655(93)90005-W.

[54] ROOT, “TFractionFitter Class Reference”. https://root.cern.ch/doc/v606/classTFractionFitter.html.

[55] CMS Collaboration, “CutBasedPhotonIdentificationRun2”. https://twiki.cern.ch/twiki/bin/view/CMS/CutBasedPhotonIdentificationRun2.

[56] CMS Collaboration, “BtagRecommendation80XReReco”. https://twiki.cern.ch/twiki/bin/viewauth/CMS/BtagRecommendation80XReReco.

[57] G. Cowan, K. Cranmer, E. Gross, and O. Vitells, “Asymptotic formulae for likelihood-based tests of new physics”, *The European Physical Journal C* **71** (Feb, 2011) 1554, doi:10.1140/epjc/s10052-011-1554-0.

[58] The ATLAS Collaboration, The CMS Collaboration, The LHC Higgs Combination Group Collaboration, “Procedure for the LHC Higgs boson search combination in Summer 2011”, Technical Report CMS-NOTE-2011-005. ATL-PHYS-PUB-2011-11, CERN, Geneva, Aug, 2011.

[59] CMS Collaboration, “RooStats-based statistics tools for Higgs PAG”. https://twiki.cern.ch/twiki/bin/viewauth/CMS/SWGuideHiggsAnalysisCombinedLimit#Computing_limits_with_the_asympt.

[60] The CMS collaboration, “Search for natural supersymmetry in events with top quark pairs and photons in pp collisions at sqrt(s)=8 TeV”, *Journal of High Energy Physics* **2018** (Mar, 2018) 167, doi:10.1007/JHEP03(2018)167.

[61] CERN, “ROOT:Chi2Test()”. https://root.cern.ch/doc/master/classTH1.html.